Magneto-transport and High Pressure transport studies on the Topological Insulator system Bi_2Se_3

By

T. R. Devidas

(Enrollment No: PHYS02 2010 04006)

Indira Gandhi Centre for Atomic Research, Kalpakkam

A Thesis Submitted to the
Board of Studies in Physical Sciences
In partial fulfillment of requirements
For the Degree of

DOCTOR OF PHILOSOPHY

of

HOMI BHABHA NATIONAL INSTITUTE

February, 2016

Homi Bhabha National Institute

Recommendations of the Viva Voce Committee

As members of the Viva Voce Committee, we certify that we have read the dissertation prepared by **Mr. T. R. Devidas** entitled ''**Magneto-transport and High Pressure transport studies on the Topological Insulator system Bi_2Se_3**'' and recommend that it may be accepted as fulfilling the thesis requirement for the award of Degree of Doctor of Philosophy.

Chairman – **Dr. C. S. Sundar** **Date:** 10/6/2016

Guide / Convener – **Dr. Awadhesh Mani** **Date:** 10/6/2016

Awadhesh Mani

Co-Guide – **Dr. A. Bharathi** **Date:** 10/6/2016

N.V. Chand

Member 1 – **Dr. P. Ch. Sahu** **Date:** 10/6/2016

P. Ch. Sahu

Final approval and acceptance of this thesis is contingent upon the candidate's submission of the final copies of thesis to HBNI.

I/We hereby certify that I/we have read this thesis prepared under my/our direction and recommend that it may be accepted as fulfilling the thesis requirement.

Date : 10/06/2016

N.V. Chand 10/6/2016

Awadhesh Mani

Place: IGCAR,
Kalpakkam

Dr. A. Bharathi
Co-Guide

Dr. Awadhesh Mani
Guide

STATEMENT BY AUTHOR

This dissertation has been submitted in partial fulfillment of requirements for an advanced degree at Homi Bhabha National Institute (HBNI) and is deposited in the library to be made available to borrowers under rules of the HBNI.

Brief quotations from this dissertation are allowable without special permission, provided that accurate acknowledgement of source is made. Requests for permission for extended quotation from or reproduction of this manuscript in whole or in part may be granted by the Competent Authority of HBNI when in his or her judgment the proposed use of the material is in the interest of scholarship. In all other instances, however, permission must be obtained from the author.

T.R. Devidas

[T. R. Devidas]

DECLARATION

I, hereby declare that the investigation presented in the thesis has been carried out by me. The work is original and has not been submitted earlier as a whole or in part for a degree/diploma at this or any other Institution/University.

T.R. Devidas

[T. R. Devidas]

List of Publications

Journal

a) **Published**

1. Role of Se vacancies on Shubnikov-de Haas oscillations in Bi_2Se_3: A combined magneto-resistance and positron annihilation study

   T. R. Devidas, E. P. Amaladass, Shilpam Sharma, R. Rajaraman, D. Sornadurai, N. Subramanian, Awadhesh Mani, C. S. Sundar and A. Bharathi, *EPL* **108** (2014) 67008

2. Magneto-transport behaviour of $Bi_2Se_{3-x}Te_x$: Role of disorder

   E. P. Amaladass, **T. R. Devidas**, Shilpam Sharma, C. S. Sundar, Awadhesh Mani and A. Bharathi, *J. Phys.: Condens. Matter* **28** (2016) 075003

b) **Manuscript under revision**

1. Magneto-transport in the Topological Insulator system $Bi_{2-x}Sb_xSe_3$

   T. R. Devidas, E. P. Amaladass, Shilpam Sharma, Awadhesh Mani, R. Rajaraman, C. S. Sundar and A. Bharathi

c) **Other Publications (not included as a part of the thesis):**

1. Pressure-induced structural changes and insulator-metal transition in layered bismuth triiodide, BiI_3: a combined experimental and theoretical study

   T. R. Devidas, N. V. C. Shekar, C. S. Sundar, P. Chithaiah, Y. A. Sorb, V. S. Bhadram, *J. Phys.: Condens. Matter* **26** (2014) 275502

2. Observation of superconductivity in $SrMnBi_2$ and Bi interface

   K. Vinod, A. Bharathi, A. T. Satya, Shilpam Sharma, **T. R. Devidas**, Awadhesh Mani, A. K. Sinha, S. K. Deb, V. Sridharan, C. S. Sundar, *Solid State Commun.* **192** (2014) 60

3. Unification of the pressure and composition dependence of superconductivity in Ru substituted $BaFe_2As_2$

T. R. Devidas, Awadhesh Mani, Shilpam Sharma, K. Vinod, A. Bharathi, C. S. Sundar, *Solid State Commun.* **185** (2014) 62

Papers/Posters presented in national/international conferences:

1. High pressure studies on topological insulator Bi_2Se_3

   T. R. Devidas, Awadhesh Mani, and A. Bharathi, *DAE-Solid State Physics Symposium (DAE-SSPS, December 3-7, 2012)* Mumbai, India

   Published in *AIP Conf. Proc.* **1512** (2013) 964

2. Polarized Micro-Raman spectra of Sb_2Te_3: A Topological Insulator

   T. R. Devidas, S. Dhara, Awadhesh Mani, A. Bharathi, *International Conference On Raman Spectroscopy (ICORS, August 12-17, 2012)* Bangalore, India

T. R. Devidas

[T. R. Devidas]

Dedicated To
Mother Nature
Of which
I am just a tiny speck of dust

ACKNOWLEDGEMENTS

Firstly, I would like to express my sincere gratitude to my research supervisors Dr. Awadhesh Mani and Dr. A. Bharathi for their valuable guidance during my research tenure. Their innovative ideas, immense knowledge and motivation kept me brimming with positive energy throughout the course of the work.

Besides my supervisors, I would also like to thank the rest of my thesis committee: Dr. C. S. Sundar and Dr. P. Ch. Sahu, for their insightful comments and encouragement, but also for the hard questions which incented me to widen my research from various perspectives.

I sincerely thank the Department of Atomic Energy, India for providing me necessary financial support throughout my research tenure. I am grateful to Dr. Baldev Raj, former Director, IGCAR, for allowing me to carry out my research work in Material Science Group and also the subsequent directors Shri. S. C. Chetal, Dr. P. Vasudeva Rao including the current director Dr. S. A. V. Satyamurthy for allowing me to continue my research work in this esteemed institute.

I am grateful to my seniors in the lab Dr. T. Sathyanarayana Annam, Dr. Shilpam Sharma, Dr. rer. nat. A. Edward Prabhu and Dr. K. Vinod for their willingness to share knowledge and helping me in carrying out experiments. I also thank my lab-mate and fellow research scholar Mr. Radhikesh Raveendran Nair for the wonderful time spent in lab discussing anything from science to sports.

I express my sincere thanks Dr. G. Amarendra for allowing me to use the 15 T Cryogen-free Magneto-Resistance facilities at UGC-DAE-CSR, Kalpakkam node; without which this thesis is not possible. I thank Dr. R. Rajaraman, Dr. Varghese Anto Chirayath and Dr. S. Abhaya for the helping me with the positron lifetime measurements and analysis. I also thank Dr. N. Subramanian, MSG and Prof. A. Thamizhavel, TIFR for helping me in carrying out Laue diffraction of samples at the latter's lab. I thank Dr. V. Sridharan and Dr. S. Kalavathi for their help in XRD experiments.

I thank Dr. M. Sai Baba for providing accommodation at the JRF enclave during my research tenure. Special thanks to Dr. Pradeep Kumar Samantaroy for being an accommodative and wonderful roommate and senior during my initial years in enclave.

Words are insufficient to thank my dear friends at the enclave – K. Benadict Rakesh, V. Mahendran, D. Karthickeyan, Irshad K. Abbas, K. Srinivasan, M. Vairavel, C. Lakshmanan, M. Thangam, K. G. Raghavendra, without whom hostel life would have been boring. I also extend my warm thanks to my batch-mates K. Kamali, M. Kalyan Phani, Avinash Patsha, Bonu Venkataramana, G. Prasanna, A. V. Meera, K. R. Rasmi, Soja K. Vijay, Anbumozhi Angayarkanni, Leona J. Felicia and M. Sabeena.

I take this opportunity to thank my grandparents late N. S. Raghuthaman and late K. Rajamma for their blessings, and Shri R. S. Moorthy for his kind caring.

I am especially indebted to my caring parents and my lovely sister for bestowing me with their unconditional love and encouragement, and for having been there at every step of the journey without which this thesis would not be possible.

T.R. Devidas

(T. R. Devidas)

CONTENTS

Chapter 2 Experimental Techniques 43

Chapter 3 Quantum oscillations from Topological Surface States in Bi_2Se_3 62

Chapter 4 Magneto-transport studies on Sb substituted Bi_2Se_3 single crystals 92

Chapter 5 Magneto-transport studies on Te substituted disordered Bi_2Se_3 single crystals 115

SYNOPSIS

Topological insulators (TI) are an exotic class of compounds that have a band-gap in the bulk co-existing with gapless conducting edge/surface states on the edge/surface and have been extensively investigated in condensed matter physics in the past few years [1]. The characteristic features of these conducting states are that they are dissipation-less and spin polarized, properties that arise from their Dirac fermion like linear ε-k dispersion and strong spin-orbit coupling. These conducting states are topologically protected which makes them robust against weak perturbation or disorder and are hence very promising from the technological point of view such as in the field of spintronics and quantum computation [1]. The major focus has been on identification, growth and characterization of 3D TIs which possess conducting "topological surface states (TSS)" analogous to conducting "topological edge states" observed first in HgTe/CdTe [2] quantum well structure. The binary alloy $Bi_{1-x}Sb_x$ was the first 3D TI to be predicted and experimentally confirmed. However the narrow Sb doping range ($0.07 < x < 0.22$), small band-gap (0.03 eV at $x = 0.18$) and the presence of multiple surface states subsequently reduced the interest in the system [3]. The prediction and confirmation of Bi_2X_3 (X = Se, Te) class of binary compounds being 3D TIs however sparked off extensive research, as they are relatively easy to synthesis, have a wider band gap (0.35 eV for Bi_2Se_3) and present a single Dirac cone [4]. Surface sensitive techniques such as Angle Resolved Photo-Emission Spectroscopy (ARPES) [4] and Scanning Tunneling Microscopy (STM) [5] have been widely used to probe the TSS.

Bi_2Se_3 – considered as the "hydrogen atom of 3D TI", crystallizes in the $R\bar{3}m$ space-group. It's tetradymite structure consists of Se(1)-Bi-Se(2)-Bi-Se(1) quintuples (QLs) separated by Van der Waals force; where Se(1) and Se(2) are two non-equivalent positions of Se in QL. With a measured band-gap of 0.35 eV, single crystals of Bi_2Se_3 are expected to exhibit the properties of a semiconductor in resistivity measurements. However, they exhibit metallic resistivity behaviour and the Hall Effect measurement suggests that the crystals are highly n-doped [6]. First principle calculations associate the n-type doping predominantly to Se vacancies [7, 8]; however direct experimental evidence for quantifying vacancies seems lacking. ARPES measurements performed on Bi_2Se_3 have shown that the presence of charge defects shifts the bulk Fermi level from the bulk band gap into the conduction band [9]. This causes complications in transport measurements as the parallel conductance from the bulk makes it difficult to distinguish between signatures from the TSS and that of bulk. Further, the presence of a semiconductor/metal interface in a TI results in phenomena such as band-bending [9], in order to establish equilibrium between the bulk and surface Fermi levels. These play a significant role in observing the signature of TSS states in transport measurements viz. 2D Shubnikov de Haas (SdH) oscillations and Weak Anti-localisation (WAL) behaviour [10]. The major research pertaining to Bi_2Se_3 has been focused on the shifting the Fermi level into the bulk band-gap without disturbing the topological surface states so as to realize their signatures in transport measurements. To achieve this, various methods have been adopted such as (a) doping, (b) growing thin films and nanostructures, (c) electric gating; with varying degree of success [6]. Recent band structure calculations point out to a major role played by defects/disorder in modifying the direction of band-bending [11, 12, 13] and hence shifting the Dirac point such that the Fermi level lies in the surface states, thereby affecting the relative contribution of surface states and bulk state to the transport property.

The current thesis aims at investigating the role of defects/disorder in observing the signature of TSS in transport measurements in the Bi_2Se_3 crystal system by the following routes:

- Introducing weak and strong disorder by varying the growth conditions of Bi_2Se_3 single crystals. The presence of defects has been investigated using the technique of Positron Annihilation Spectroscopy.
- Controlling the disorder in the Bi_2Se_3 system by substitution of Sb and Te at the cationic and anionic site respectively.
- Applying external pressure to modify the electronic structure and understand whether – a) pressure can suppress the bulk conductivity and unmask the surface contribution in transport; b) induce superconductivity while preserving the topological surface state which could give rise to novel superconductor/TI interface.

The thesis is organized into 7 chapters and the contents of each chapter are summarized below.

Chapter 1 – Transport behaviour in Topological Insulators (TI): An overview

Chapter 1 presents a brief introduction to the field of Topological Insulators (TI), beginning from Quantum Hall Effect to the 2nd generation 3D TIs. Also a detailed review of the current literature on the role of defects/disorder on the transport properties of 3D TIs and the idea behind the current thesis is presented.

Chapter 2 – Experimental techniques

Chapter 2 describes in detail the synthesis and various experimental techniques used in the current thesis. The modified Bridgman method, adopted for growing single crystals is described. Powder X-ray diffraction and Laue diffraction techniques used for structural characterization are briefed. The principle and working of the 15 T Cryogen free Magneto-resistance setup used for measuring the magneto-transport properties, and the fast-fast coincidence spectrometer used for measuring the Positron Lifetime are explained. The home built opposed anvil Bridgman cell used for studying the high pressure-low temperature transport properties of the samples is also described.

Chapter 3 – Quantum oscillations from Topological Surface States in Bi_2Se_3

Chapter 3 focuses on understanding the role of defects in realizing the signatures of Topological Surface States (TSS) viz., the Shubnikov-de Haas (SdH) oscillations in magneto-transport measurements in single crystalline Bi_2Se_3. Positron lifetime measurements supported by ab-initio calculations of Positron density on stoichiometric Bi_2Se_3 single crystals establish, for the first time, that Se vacancies play the dominant role in n-type doping of the Bi_2Se_3 crystal. Single crystals are synthesized under different growth conditions – a) varying the Se/Bi stoichiometry and b) cooling from melt at different rates (1°C/hr., 2°C/hr. and 137°C/hr.), to control the defect concentration. The crystals are characterized using powder XRD and Laue diffraction for structure. Magneto-transport measurements have been performed in the temperature range 4.2 K – 10 K and under 0 T – 15 T magnetic fields. It is observed that samples exhibiting SdH oscillations show a pronounced strain in Laue patterns associated with the presence of low-angle tilt grain boundaries and stacking fault disorder in the crystals. The appearance of TSS signatures viz. Shubnikov-de Haas (SdH) oscillations in magneto-transport measurements on Bi_2Se_3 is directly correlated to the presence of low-angle grain boundaries and extended defects such as stacking faults that shift the Dirac point to lower energies leading to upward band-bending behaviour, which in turn favour the transport being dominated by the TSS.

Chapter 4 – Magneto-transport studies on Sb substituted Bi_2Se_3 single crystals

Chapter 4 presents a detailed magneto-transport study on the effect of Sb substitution on the signatures of TSS in magneto-transport measurements on the Bi_2Se_3. Since the Spin-Orbit Interaction (SOI) plays an important role in defining the band-gap in TIs, Sb with a reduced SOI parameter has been increasingly substituted for Bi starting with the optimized parent Bi_2Se_3, so as to study the effect of reduced SOI on the TSS signatures. Magneto-transport measurements have been carried out on $Bi_{2-x}Sb_xSe_3$ (x = 0, 0.05, 0.1, 0.3 & 0.5) single crystals in the 4.2 K – 300 K temperature and 0 T – 15 T magnetic field range. It is observed that Shubnikov-de Haas (SdH) oscillations have a 2D character; however their origin, as deduced from the Landau Level-Fan diagram analysis, changes from, the TSS in x = 0, 0.05 & 0.1 to a mixture of TSS and the conventional 2D electron gas that forms at the metal/semiconductor interface in x = 0.3. The data is further analysed and the results are discussed.

Chapter 5 – Magneto-transport studies on Te substituted Bi_2Se_3 single crystals

Chapter 5 discusses the results of magneto-transport experiments carried out on fast cooled single crystals of $Bi_2Se_{3-x}Te_x$ (x = 0 to 2) system in the 4.2 K – 300 K temperature range and 0 T – 15 T magnetic field range. The variation of resistivity with temperature that points to a metallic behaviour in Bi_2Se_3, shows an up-turn at low temperatures in the Te doped samples. Magneto-resistance measurements in Bi_2Se_3 show clear signatures of Shubnikov – de Hass (SdH) oscillations that gets suppressed in the Te doped samples. In the Bi_2SeTe_2 sample, the magneto-resistance shows a cusp like positive magneto-resistance at low magnetic fields and low temperatures, a feature associated with weak anti-localisation (WAL), that crosses over to negative magneto-resistance at higher fields. The qualitatively different magneto-transport behaviour seen in Bi_2SeTe_2 as compared to Bi_2Se_3 is rationalised in terms of the disorder, through an estimate of the carrier density, carrier mobility and an analysis in terms of the Ioffe-Regel criterion with support from Hall Effect measurements.

Thus the substitution of larger Te for Se in Bi_2Se_3 introduces strong electronic disorder. A low field cusp in magneto-resistance, attributed to the Weak Anti-localization associated with TSS is observed at high Te concentration accompanied by the change in character of the Hall slope from linear to non-linear. This indicates the increased contribution of TSS in transport.

Chapter 6 – High pressure transport studies on single crystal TI system $Bi_2Se_{3-x}Te_x$

Chapter 6 presents the data on transport properties of $Bi_2Se_{3-x}Te_x$ system under high pressure and low temperatures. Bi_2Se_3 changes from a metallic to insulating behaviour with a distinct hump-like behaviour occurring at temperature $T_{shoulder}$, which shifts to higher temperature with increasing pressure. Bi_2Se_2Te changes character from a system indicating metal-insulator transition at ambient pressure to completely insulating and then to metallic system with increasing pressure. The system exhibits superconductivity with a transition temperature (T_C) = 5.90 K at a pressure of 2.5 GPa. The T_C shifts to lower temperatures with increase in pressure beyond 2.5 GPa. Bi_2SeTe_2 system changes behaviour from insulating to metallic with increasing pressure. The system exhibits superconductivity with a T_C = 6.20 K at a pressure of 1.2 GPa and the T_C shifts to slightly lower values with increase in pressure. The Bi_2Te_3 exhibits completely metallic behaviour till the highest pressure in the current experiments and also undergoes a superconducting transition at 1.7 GPa with a T_C = 5.87 K. The T_C doesn't exhibit much variation with increasing pressure. The observed behaviour across the $Bi_2Se_{3-x}Te_x$ series is analyzed and the results are discussed. It is thus observed that although the pristine Bi_2Se_3 does not show superconducting transition even upto 8 GPa, addition of Te makes the system favour a superconducting phase under pressure.

Chapter 7 – Summary of the thesis and Future work

This chapter summarizes the various results obtained in the current thesis and also the directions for future work.

References:

[1] M. Z. Hasan & C. L. Kane, *Rev. Mod. Phys*. **82** (2010) 3045

[2] Markus König, Steffen Wiedmann, Christoph Brüne, Andreas Roth, Hartmut Buhmann, Laurens W. Molenkamp, Xiao-Liang Qi and Shou-Cheng Zhang, *Science* **318** (2007) 766

[3] Jeroen B. Oostinga and Alberto F. Morpurgo, in *Contemporary Concepts of Condensed Matter Science – Topological Insulators* (Elsevier) 2013, pp. 199-233

[4] Y. Xia, D. Qian, D. Hsieh, L.Wray, A. Pal, H. Lin, A. Bansil, D. Grauer, Y. S. Hor, R. J. Cava and M. Z. Hasan, *Nat. Phys.* **5** (2009) 398

[5] Peng Cheng, Canli Song, Tong Zhang, Yanyi Zhang, Yilin Wang, Jin-Feng Jia, et al. *Phys. Rev. Lett.* **105** (2010) 076801

[6] Dimitrie Culcer, *Physica E* **44** (2012) 860

[7] D. West, Y. Y. Sun, Han Wang, Junhyeok Bang, and S. B. Zhang, *Phys. Rev. B* **86**, (2012) 121201 (R)

[8] L. Xue, P. Zhou, C. X. Zhang, C. Y. He, G. L. Hao, L. Z. Sun and J. X. Zhong, *AIP ADVANCES* **3**, (2013) 052105

[9] J. G. Analytis, J. H. Chu, Y. Chen, F. Corredor, R. D. McDonald, Z. X. Shen et al. *Phys. Rev. B* **81** (2010) 205407

[10] Dohun Kim, Paul Syers, Nicholas P. Butch, Johnpierre Paglione and Michael S. Fuhrer, *Nat. Commun.* **4** (2013) 2040

[11] Dimitrios Galanakis and Tudor D. Stanescu, *Phys. Rev. B* **86** (2012) 195311

[12] L. Seixas, L.B. Abdalla, T.M. Schmidt, A. Fazzio, R.H. Miwa, *J. Appl. Phys.* **113** (2013) 023705

[13] Y. Liu, Y. Y. Li, S. Rajput, D. Gilks, L. Lari, P. L. Galindo, et al. *Nat. Phys.* **10** (2014) 294

LIST OF FIGURES

LIST OF TABLES

CHAPTER 1

Transport behaviour in Topological Insulators (TI): An overview

Much of condensed matter physics aims at understanding the different phases of matter and transitions between them by change of pressure, temperature and chemical potential. The language used to understand why these transitions occur comes under the purview of symmetry breaking principles and was detailed by Landau in his theory of phase transitions. To give a few examples, in structural transitions the translational symmetry is changed, while in ferromagnets rotational symmetry is broken and in superconductors the gauge symmetry is broken. With the discovery of Integer Quantum Hall Effect (IQHE) by Klaus von Klitzing et al. [1] in 1980, the basic understanding of phase transitions had to be revisited as the normal state to IQHE state transition could not be explained on the basis of symmetry breaking alone. A new classification of phases, based on the topological property of the ground states was propounded by Thouless et al. [2] wherein a system is said to undergo a phase transition if there is a change in the topological property of its ground state. To understand what constitutes a topological transition let us first look at the definition of topology.

1.1 Topology

Topology is the mathematical study of the properties that are preserved through deformations, twisting and stretching of objects. For example, two geometrical constructions that can be transformed into one another by simple deformations are said to be topologically equivalent. In three dimensional Euclidean space, the topological class is based on the genus (g) i.e. the number of handles present; the geometries with the same number of handles are considered topologically equivalent. Thus, a coffee cup and a doughnut are topologically equivalent (g = 1) as are a solid sphere and a solid cube (g = 0). However the solid sphere and the doughnut are topologically non-equivalent as the solid sphere cannot be transformed into the doughnut without piercing a hole through. This pinching of a hole is what constitutes a topological phase transition. Figure 1.1 shows the topological equivalence between a coffee mug and a doughnut, sphere and a cube and the non-equivalence between the doughnut and a sphere.

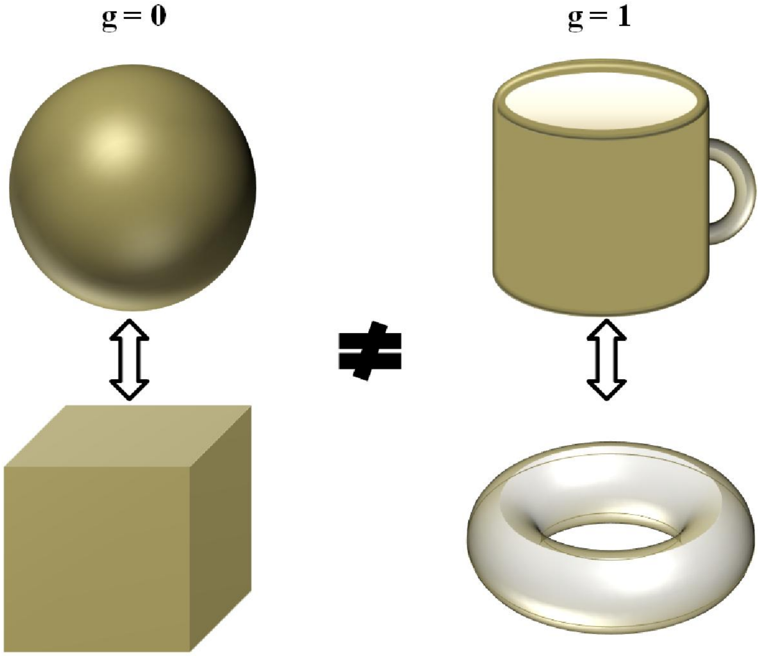

Figure 1.1 – The sphere and cube on the left hand side are topologically equivalent with g = 0 as are the coffee cup and the torus on the right with g =1. The sphere and the coffee cup are topologically non-equivalent as they cannot be transformed into one another through smooth deformations.

In a band insulator, the concept of topology is applied to the parity characteristic of the valence band manifold. If the parity changes at an odd number of special points in the Brillouin zone, the insulator is termed a non-trivial or topological insulator whereas if the parity characteristic does not change or changes at an even number of points in the Brillouin zone, the insulator is termed a trivial insulator. The principle of adiabatic continuity can be used to explain topological equivalence in insulators i.e. two insulators are said to be topologically equivalent if they can be changed into one another by adiabatically tuning the Hamiltonian such that the finite energy gap in the band-structure doesn't vanish. An equivalent statement that can be made is that while connecting two topologically different insulators, the topological phase transition that happens is defined by the vanishing of the energy gap. The first instance of such a topological phase transition taking place was found with the discovery of the Integer Quantum Hall Effect by Klaus von Klitzing et al. in 1980 [1].

1.2 Integer Quantum Hall Effect (IQHE)

In this quantum analogue of the Classical Hall Effect, when a current carrying 2-Dimensional Electron Gas (2DEG) system is subjected to a strong perpendicular magnetic field, the Hall resistivity (ρ_{xy}) is observed to have quantized plateaus at values of $h/\nu e^2$, as depicted in Figure 1.2, which shows the IQHE data measured on InGaAs based heterostructure at a temperature of 0.3 K [3]. Here h is the Planck's constant; e is the electron charge and ν is an integer described as the filling factor.

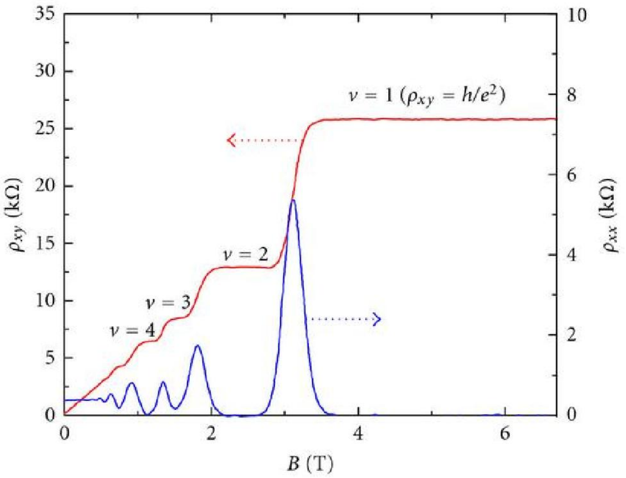

Figure 1.2 – Experimental measurements of the integer quantum Hall effect for an InGaAs based heterostructure at a temperature of 0.3 K (adopted from [3])

At the values of magnetic fields where quantized plateaus are observed in ρ_{xy}, clearly the value of longitudinal resistivity (ρ_{xx}) also reduces to zero value as is evident from Figure 1.2. The phenomena can be explained as follows. Under strong magnetic fields and low temperatures, the free electrons in the system get quantized in cyclotron orbits (ref. Figure

1.4(b)) and as a consequence, the energy levels in the system are quantized into Landau Levels (LLs) with energy $E_n = \left(n + \frac{1}{2}\right)\hbar\omega_c$ (ref. Figure 1.3). Here $\hbar$ is the reduced Planck's constant and ω_c is the cyclotron frequency. The maximum of ρ_{xx} corresponding to the simultaneous increase in ρ_{xy} (ref. Figure 1.2) with increasing magnetic field occurs when the Fermi Level lies in between two Landau Levels; and the vanishing of ρ_{xx} occurring simultaneously to the quantization of ρ_{xy} into plateaus occurs when the Fermi level lies at the centre of a Landau Level (cf. Figure 1.3).

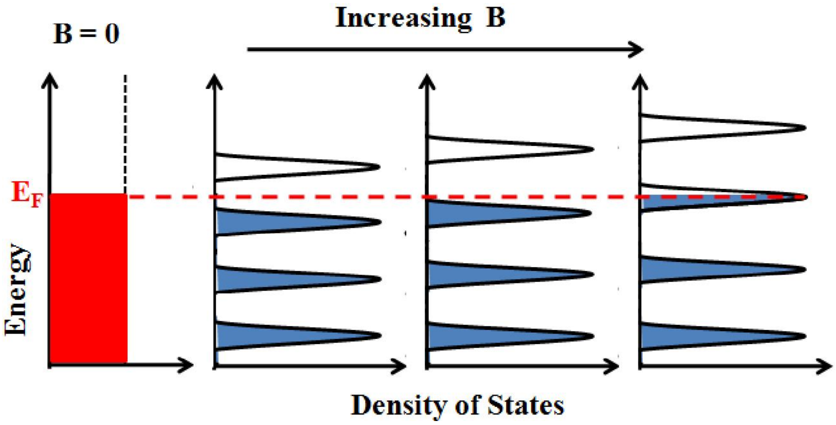

Figure 1.3 – Energy level vs. number of states that the electrons can occupy for increasing magnetic field strength. The Fermi level marked by E_F is dotted in red. Only those Landau Levels that lie below the E_F are occupied

As is evident from Figure 1.3, when the Fermi level lies between two Landau Levels, the LLs lying below the Fermi level are filled and those lying above are empty i.e. an energy gap exists between the occupied and vacant states akin to a normal insulator. The Landau Levels can thus be identified as a band-structure of the IQHE state. In addition to the IQHE being a quantum macroscopic phenomenon, Thouless et al. [2] showed that it is a topological phenomenon i.e. the IQHE is topologically distinct from other types of insulating states namely band insulator in condensed matter solids. They showed that the quantized plateaus bear the signatures of this topological state termed, the Chern number ν which occurs in the expression for ρ_{xy} shown earlier [2].

A characteristic feature of the IQHE state is the presence of chiral edge states that arise at the interface of a 2DEG sample and the vacuum. This is on account of a direct consequence of the topological character of gapped band structures, a semi-classical description of which follows. As mentioned earlier, the electrons in the IQHE state get quantized in cyclotron orbits (ref. Figure 1.4(b)). However, for the electrons that are at the edges of the 2DEG sample, the cyclotron orbits are incomplete and hence they form skipping orbits. The conduction along these edge states is unidirectional, defined by the direction of applied external magnetic field to the system (as shown in Figure 1.4(b)). These edge states are spin degenerate states i.e. irrespective of the spin of the electron, the electrons at one edge travel along one direction and the electrons on the other edge travel in the opposite direction (as shown in Figure 1.4(b)) and hence chiral.

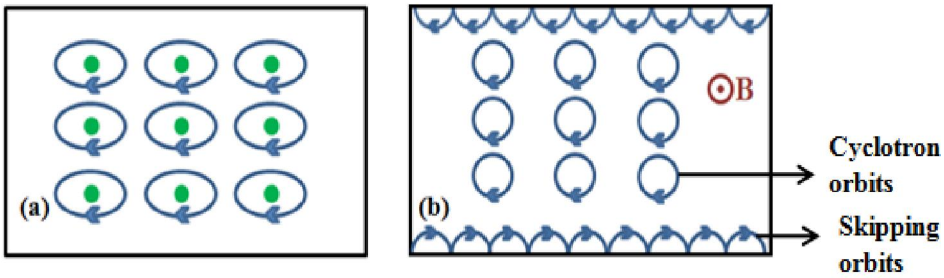

Figure 1.4 – **(a)** The atomic insulator; **(b)** The Integer Quantum Hall state with skipping orbits forming the edge states

1.3 Integer Quantum Hall Effect in Graphene

Using the tight binding model on the honeycomb lattice of graphene (ref. Figure 1.5(a)), Haldane [4] proposed that the IQHE state could be realized in graphene. The band-structure of graphene has a unique feature, wherein the conduction and valence bands touch each other at two distinct points in the Brillouin zone (K and K') (as shown in Figure 1.5(b))

[5]. The electronic dispersion near these points is linear and can be described by the relativistic Dirac equation by setting the rest mass of the fermion to be zero [6][7][8].

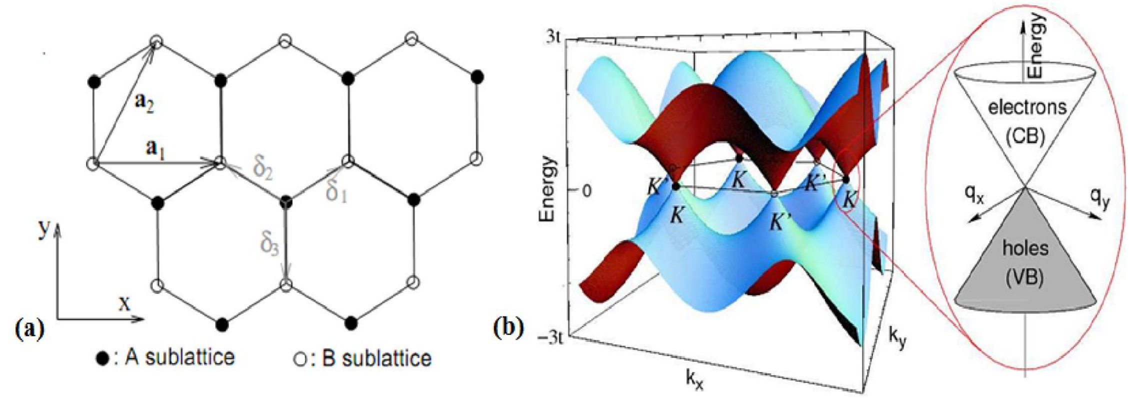

Figure 1.5 – **(a)** Honeycomb lattice of graphene. $\mathbf{a_1}$ and $\mathbf{a_2}$ are the basis vectors of the triangular Bravais lattice; **(b)** the band structure of graphene. At two inequivalent BZ corners the valence band and conduction band touch each other and the band dispersion near these points is conical as shown in the zoomed portion (adopted from [5]).

The dispersion at one of the K points is zoomed in Figure 1.5(b). This shows a double cone, meeting at the Dirac point. The states in the valence band (VB) are shown shaded while the top non-shaded cone is the conduction band (CB). These are called the Dirac cone in the band-structure of graphene. The presence of the chiral edge states was also proven by Haldane's model under the conditions of a semi-infinite geometry. A schematic diagram where the direction of electron flow is marked is illustrated in Figure 1.6(a)).

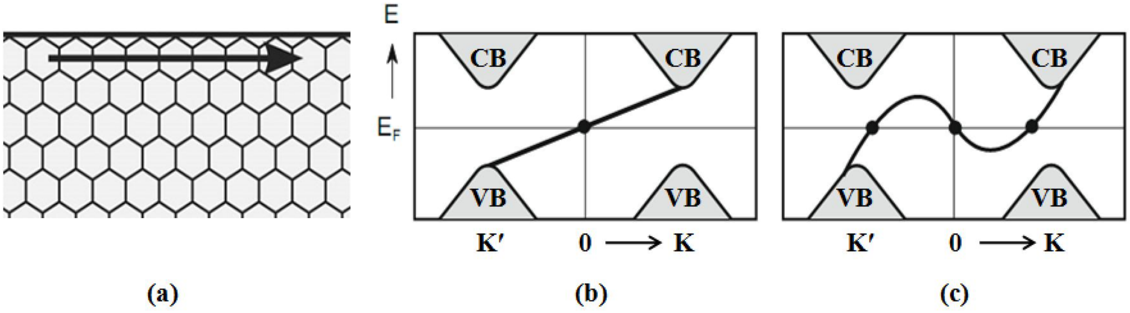

(a) (b) (c)

Figure 1.6 – **(a)** Edge states in Haldane's model on a semi-infinite plane; **(b)** The chiral edge states that connect the valence band and the conduction band near K and K'; **(c)** tuning the Hamiltonian near edge changes the number of times the edge states intersect with the Fermi level, but Δn is always equal to 1 (adopted from [6])

To mimic the IQHE state, a gap needs to be formed in the band structure. This is achieved by the application of magnetic field which breaks the time reversal symmetry in graphene [9]. Figure 1.6(b)-(c) shows a schematic of the energy levels as a function of the momentum k_x along semi-infinite edge of graphene. The bulk valence band and conduction band are labelled VB and CB respectively. The energy gaps at K and K' are also seen in the schematic. The chiral edge states are represented by the single band that connects the valence band at K' to the conduction band at K. The dispersion of the edge states and the number of times it crosses the Fermi level can be changed by tuning the Hamiltonian near the surface (as shown in Figure 1.6(b)-(c)), however the difference between the number of right moving (N_R) and left moving modes (N_L), "Δn" cannot be changed. It is always an integer value and is a topological invariant that characterizes the interface [6]. This is called the TKNN (Thouless-Kohmoto-Nightingale-den Nijs) invariant [2] and is defined as the difference in the Chern number across the 2DEG/vacuum interface. Thus in the IQHE state, the topologically non-trivial states characterized by the chiral edge states occur only when an external magnetic field is applied viz., when the time reversal symmetry in the system is broken.

1.4 The Quantum Spin Hall Effect

Kane and Mele [10][11] predicted a new state in which strong spin-orbit coupling played the role of an external magnetic field, thus preserving time reversal symmetry. This state has a bulk electronic band gap that supports the transport of charge and spin in gapless edge states. They named it as Quantum Spin Hall (QSH) state and associated the phase with a topological invariant Z_2 [10]. The spin-orbit coupling lifts the spin degeneracy of the edge states present resulting in the chiral states at each edge of the sample that correspond to the two spins of the electron. They also predicted that the QSH state could be realised in Graphene [11]. (ref. Figure 1.7(a))

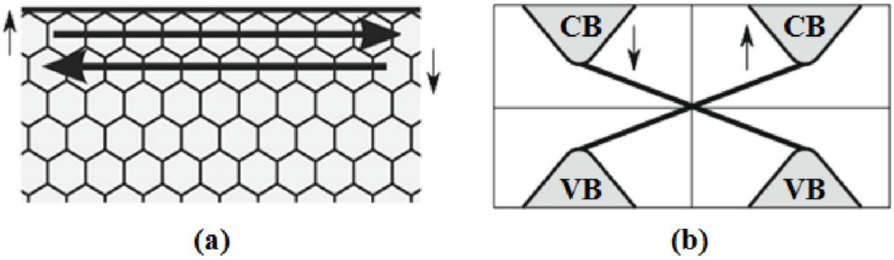

(a) (b)

Figure 1.7 – **(a)** spin-polarized edge states in graphene, obtained on introducing a spin-orbit interaction term in the Hamiltonian; **(b)** the corresponding schematic band diagram that shows the spin-polarized surface states crossing each other at Fermi level (adopted from [6])

The presence of a strong spin-orbit coupling makes these chiral edge states immune to back-scattering from impurities. The immunity of these states to back-scattering is a direct consequence of the states being spin polarized i.e. electron with up spin has a momentum +**k** and electrons with down spin has a momentum -**k**. If an electron has to be back-scattered from +**k** to -**k**, then its spin should also be flipped from up spin to downspin for which an external magnetic field is necessary; and since a field is not present, the electrons in the chiral edge states cannot be back-scattered.

To understand the physical meaning of the Z_2 index, it is necessary to understand effect of presence of time reversal symmetry in the electronic structure of a solid. The time reversal symmetry is represented by an anti-unitary operator. For a spin-half particle, this leads to a condition where the wavefunction of the particle changes its sign after a 2π rotation. As a consequence, all the eigenstates of a time-reversal invariant system with half integer total spin are two-fold degenerate. This is called the Kramer's theorem [12]. The points in momentum space where **k** and -**k** differ only by a lattice vector G, are called the Time Reversal Invariant Momenta (TRIMs). At these points, the energy of the two Kramer partners viz., the spin up and spin down electron is the same. Figure 1.8 shows the 4 TRIMs (marked as "Λ_i"; i = 1, 2, 3, 4) for a 2D Brillouin zone.

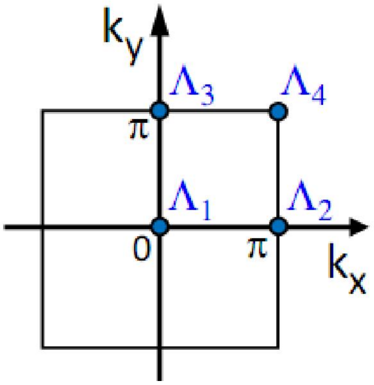

Figure 1.8 – The 4 Time Reversal Invariant Momenta for the 2D Brillouin zone (adopted from [13]).

In the absence of spin-orbit coupling, this Kramer's degeneracy refers to the degeneracy between the up-spin and down-spin states. However, in the presence of spin-orbit interactions, it introduces a new invariant (ν), in addition to the TKNN invariant [6]. The new invariant can have only two possible values ν = 0 or 1. The presence of only two classes denoted by 0 and 1 is understood from the principle of bulk-boundary correspondence. Figure 1.9 shows the electronic band-structure associated with the edge of a time reversal invariant insulator as a function of crystal momentum along the edge.

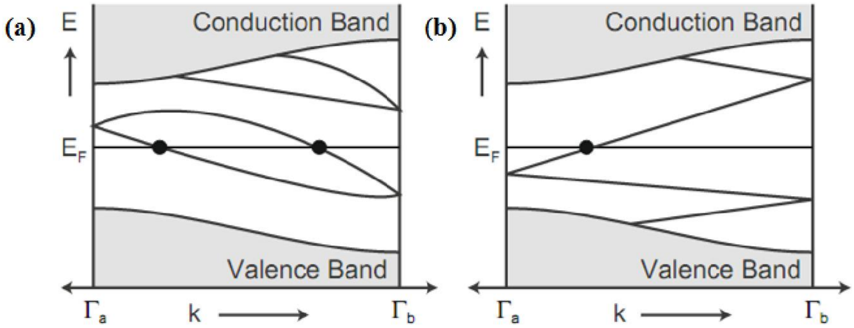

Figure 1.9 – Electronic dispersion between two boundary Kramers degenerate points. The number of surface states crossing the Fermi energy E_F in **(a)** it is even, in **(b)** it is odd (adopted from [6]). An odd number of crossings at the E_F leads to topologically protected surface states

As a consequence of the Kramer's theorem [12], the chiral edge states are two-fold degenerate at the time reversal invariant momenta (TRIM) occurring at $k_x = 0, \frac{\pi}{a}$. At other positions, the spin-orbit interaction lifts the degeneracy. The two states are then connected in two different ways as shown in Figure 1.9(a)-(b) respectively. If the connection is pair-wise i.e. if the bands intersect the Fermi energy E_F an even number of times as shown in Figure 1.9(a), the edge states can be removed by pushing the bound states out of the gap. However if the edge states connect as shown in Figure 1.9(b) where they cross E_F an odd number of times, the states can never be eliminated. The occurrence of the above two types of cross-over depends on the topological class of the valence band-structure of the system under investigation. Termed the bulk-boundary correspondence, it relates the number of Kramer's pairs of the edge modes intersecting the E_F and the change in the Z_2 invariant across the interface. The presence of an odd number of crossings at the Fermi level leads to topologically protected edge states.

1.5 Quantum Spin Hall State in 3D

Fu, Kane and Mele in their seminal paper [14] extended the QSH state to 3D systems wherein the edges states are replaced by surface states and Moore and Balents [15] showed that the topology of such system is defined by four Z_2 variants (ν_0; ν_1, ν_2, ν_3). Consider the cube in Figure 1.10 to represent the Brillouin zone of a 3D material. The Kramer's theorem [12] then defines 8 time reversal invariant momentum points in the Brillouin zone, marked as "Λ" in the figure.

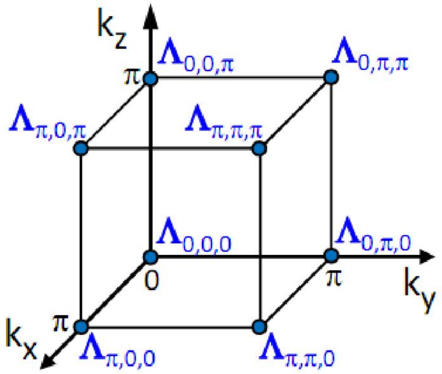

Figure 1.10 – The 8 Time reversal Invariant Momenta in a 3D Brillouin zone (adopted from [13]).

Six planes in the 3D BZ, x = 0, x = ± π, y = 0, y = ± π, z = 0, and z = ± π possess the symmetries of the 2D BZ (shown in Figure 1.8), and therefore they each have a Z_2 invariant denoted as x_0, x_1, y_0, y_1, z_0, and z_1. However, these six invariants are not independent. Thus only four invariants that are defined by the two constraining relations $x_0x_1 = y_0y_1 = z_0z_1$ can be determined independently in the 3D system. These 4 invariants (ν_0; ν_1, ν_2, ν_3) provide a complete classification of the 3D time reversal invariant insulators based on whether their values are either 0 or 1. If $\nu_0 = 1$, the system is called a strong TI and if $\nu_0 = 0$ & $\nu_i = 1$ for i = 1, 2, 3…, it is called a weak TI [13].

1.6 The Berry phase

A unique characteristic feature of the quantum spin hall insulator state is the presence of a π Berry phase in the system which is a consequence of the presence of spin-orbit coupling that spin-polarizes the fermions present in the system. By definition the Berry phase is the phase acquired by a wave function after traversing closed loop in a parameter space. The presence of a π Berry's phase in TIs can be illustrated with the help of the schematic shown in Figure 1.11.

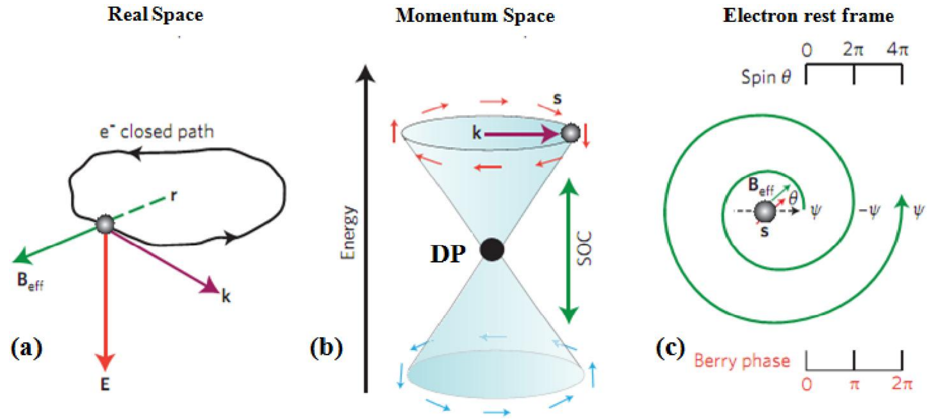

Figure 1.11 – **(a)** the electron's orbit in real space; **(b)** the Dirac cone formed as a consequence of spin-orbit coupling, DP corresponds to the Dirac point; **(c)** the physics from the electron's rest frame (adopted from [16]).

Consider an electron with position **r** and momentum **k** performing a closed orbit in real space (as shown in Figure 1.9(a)). Let ψ be the wavefunction that describes the electron behaviour. In the presence of an electric field **E**, the electron experiences an effective magnetic field $\mathbf{B}_{\mathbf{eff}}$, which couples to its spin. This spin-orbit coupling then lifts the degeneracy of the spin-degenerate states, this lifting of degeneracy results in the formation of a Dirac cone in the momentum space, with the spin (**s**) rotating with, one chirality above the Dirac point (DP), and the opposite chirality below DP (Figure 1.11(b)) [16]. However in its rest frame the electron experiences a rotating magnetic field which changes both the spin direction θ and the Berry phase of the wavefunction ψ. For every closed orbit completed in real space, θ changes by 2π, but the Berry phase only changes by π, which means that sign of the wavefunction ψ changes from ψ to $-\psi$. The electron must therefore complete two complete orbits in real space for ψ to return to its original value. This is analogous to what happens when an electron as it moves on the surface of a Möbius strip (shown in Figure 1.12).

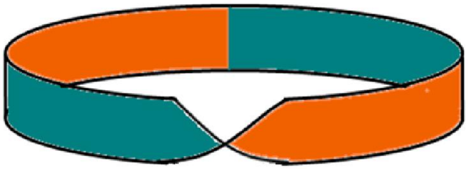

Figure 1.12 – The Möbius strip

The Möbius strip has only one edge and one side. If an electron starts from a point, it has to move around the circumference of the strip twice i.e. it has to undertake 2 x 2π rotations to arrive at the initial position because after the first 2π rotation, the electron is at the opposite surface to the initial position.

1.7 3D Topological Insulator materials

As discussed in the earlier section 1.4, a material is identified as a topological insulator by calculating the Z_2 invariant of the system. Fu and Kane [17] devised a method wherein the Z_2 invariant could be estimated from the parity eigenvalues of the Bloch wavefunctions at the Time Reversal Invariant Momenta (TRIM) in the condensed matter systems. Bernevig, Hughes and Zhang (BHZ) [18] further simplified the process into just finding out whether a band inversion occurs at odd number of TRIMs in the system. Following the theoretical model proposed by BHZ, many candidate materials that had inherently strong spin-orbit interaction were examined to see if they host topological surface states.

The following is a brief account of the materials that were predicted and then confirmed by Angle Resolved Photo-Emission Spectroscopy (ARPES) technique to be 3D Topological Insulators.

1.7.1 $Bi_{1-x}Sb_x$

$Bi_{1-x}Sb_x$ (x = 0.07-0.22) was the first 3D TI to be predicted based on band structure calculations [17]. The Z_2 invariant of the $Bi_{1-x}Sb_x$ system, determined from ab-initio calculations is found to be (1;111) and thus the system is predicted to be a strong TI. Dirac cone states were experimentally observed in $Bi_{0.9}Sb_{0.1}$ using ARPES by D. Hsieh et al. [19]. Figure 1.13 shows the ARPES data for k-space cuts along the various directions. The Dirac cone dispersed states can be easily seen from the data. However some inherent shortcomings in the $Bi_{1-x}Sb_x$ system such as the narrow Sb doping range ($0.07 < x < 0.22$) in which the material could be tuned as an insulator, small band-gap (0.03 eV at $x = 0.18$) and the presence of multiple surface states have subsequently made the system least interesting from research point of view.

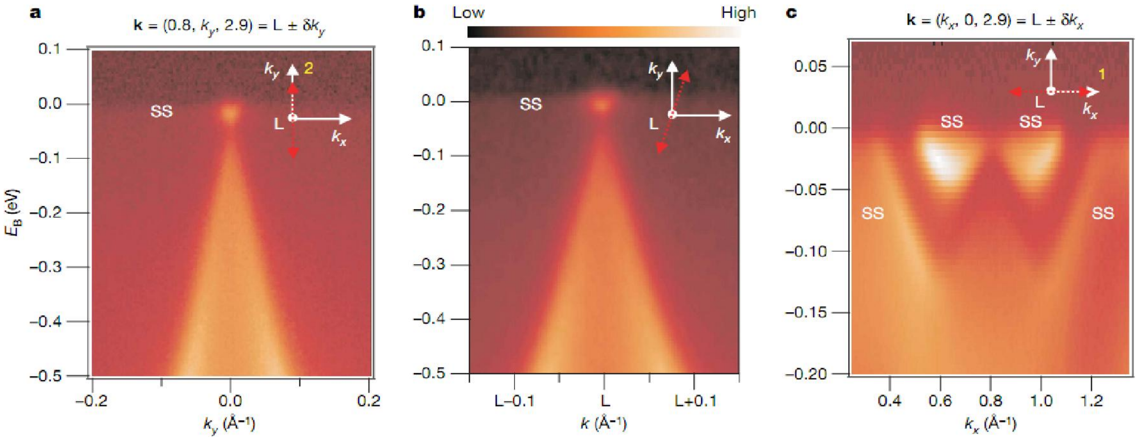

Figure 1.13 – Selected ARPES intensity maps of $Bi_{0.9}Sb_{0.1}$ along three k-space cuts **(a)** k_y direction; **(b)** a direction rotated by approximately 10° from the k_y direction; **(c)** the k_x direction through the L-point of the bulk 3D Brillouin zone (adopted from [19]).

1.7.2 A_2B_3 chalcogenide systems

Following the results on $Bi_{1-x}Sb_x$ system, Zhang et al. [20] predicted that certain compounds of the A_2B_3 chalcogenides family of crystals viz. Bi_2Se_3, Bi_2Te_3, Sb_2Te_3 are prospective candidates to realize the 3D Topological Insulators, based on ab-initio calculations performed using density functional theory. The Spin-Orbit coupling strength was found to be strong enough to cause a band inversion at the Γ point in the Brillouin zone. Figure 1.14 shows the schematic of the atomic energy levels in Bi_2Se_3 and the effect of crystal field splitting and SOC on the energy eigenvalues at the Γ point as calculated by Zhang et al. [20].

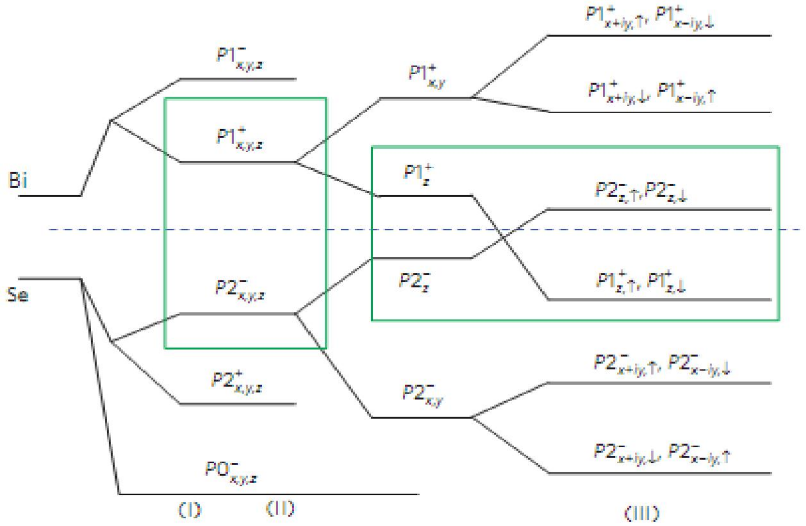

Figure 1.14 – Schematic diagram of the evolution from the atomic $p_{x,y,z}$ orbitals of Bi and Se into the conduction and valence bands of Bi_2Se_3 at the Γ point. The three different stages (I), (II) and (III) represent the effect of turning on chemical bonding, crystal-field splitting and SOC respectively. The blue dashed line represents the Fermi energy (adopted from [20]).

The calculations predicted a 3D Z_2 invariant of (1;000) for these systems and were termed Strong Topological Insulators. The theoretical prediction was followed by observation of a Dirac cone state in Bi_2Se_3 by Y. Xia et al. [21], in Bi_2Te_3 by Chen et al. [22] and, in Bi_2Te_3 and Sb_2Te_3 by Hsieh et al. [23] using Angle Resolved Photo Emission Spectroscopy (ARPES) which are reproduced in Figure 1.15(a)-(c). The Dirac Point (DP) was predicted to lie in the bulk band-gap for Bi_2Se_3 and at the top of the valence band for Bi_2Te_3 and Sb_2Te_3.

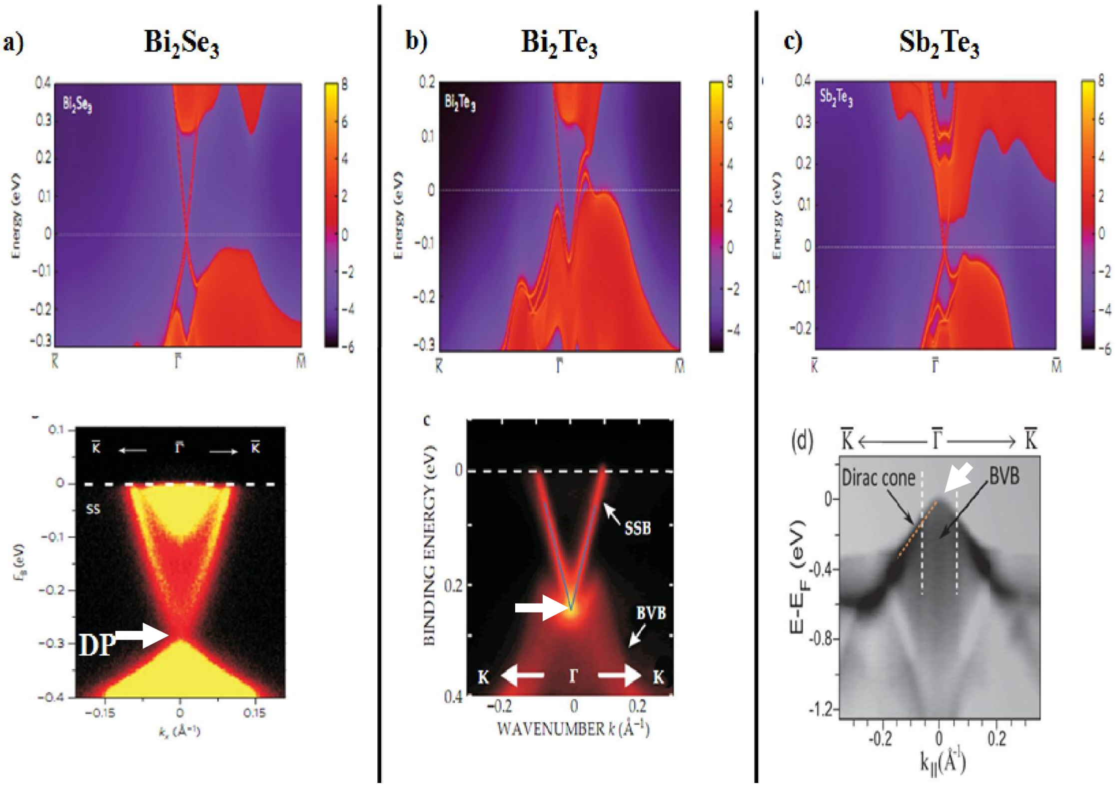

Figure 1.15 – Ab-initio calculation of the band structure at the Γ point and ARPES data on **(a)** Bi_2Se_3 [21]; **(b)** Bi_2Te_3 [22][23] and **(c)** Sb_2Te_3 showing the Dirac cones [23]. The Dirac Point (DP) is marked by the white arrows in the ARPES data.

1.7.3 Other chalcogenide systems

Similar to the binary chalcogenides, systems consisting of combinations of several A_2B_3 such as Bi_2Se_3 – Bi_2Te_3 [24][25], Bi_2Te_3 – Sb_2Te_3 [26] and Bi_2Se_3 – Bi_2Te_3 – Sb_2Te_3 [27] were also predicted to be 3D TIs. The Surface states were observed in these systems using ARPES measurements. Figure 1.16(a)-(e) shows the ARPES data on a few selected ternary and quaternary alloys. The Dirac points and the surface states are clearly visible lending credence to these ternary chalcogenides systems to be TI.

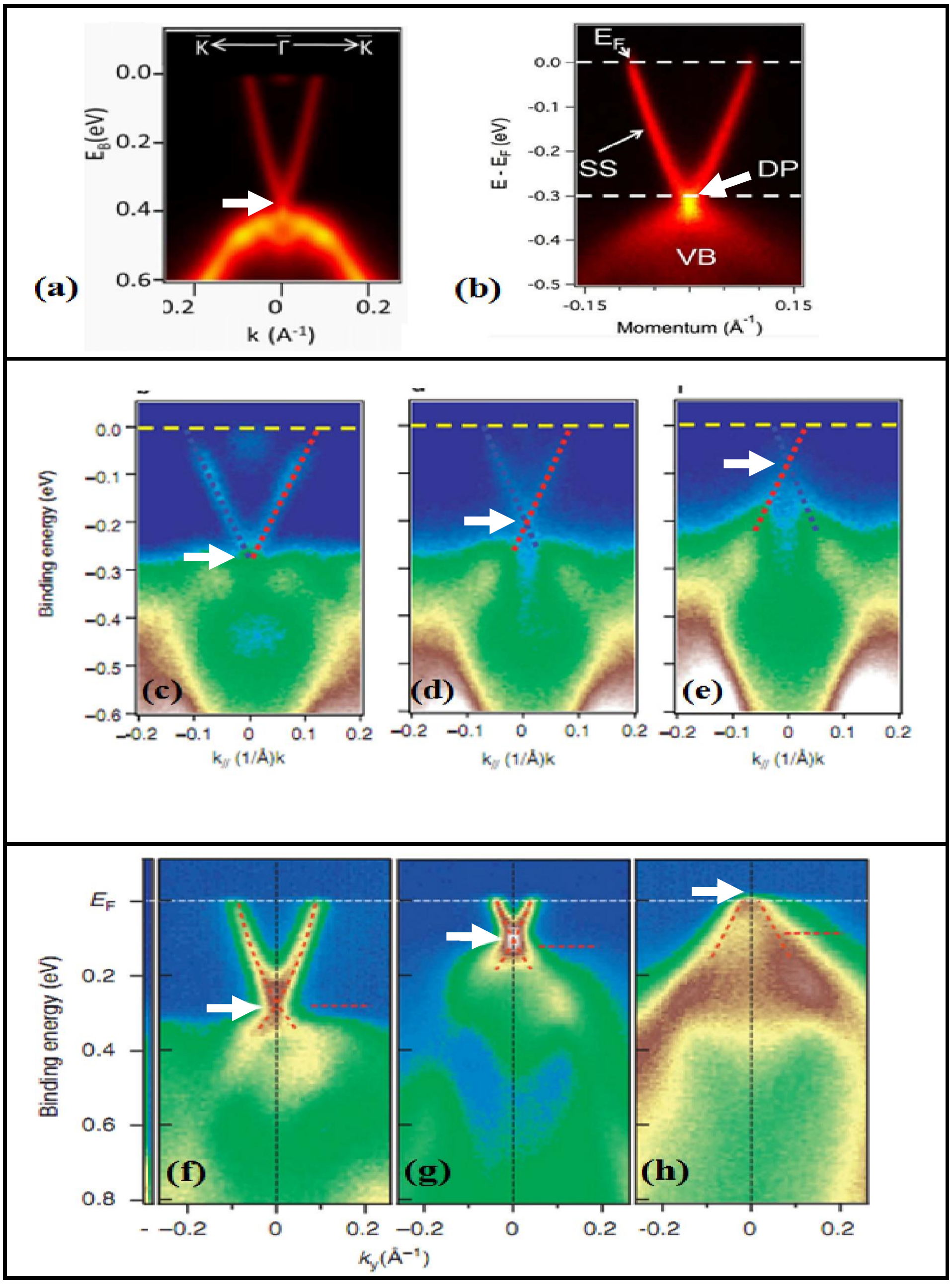

Figure 1.16 – ARPES data indicating the surface states and the Dirac Point (DP, marked by white arrows) in the ternary alloys **(a)** Bi_2Te_2Se [24]; **(b)** Bi_2Se_2Te [25]; **(c)** $Bi_{1.5}Sb_{0.5}Te_3$; **(d)** $Bi_{0.5}Sb_{1.5}Te_3$; **(e)** $Bi_{0.12}Sb_{1.88}Te_3$; **(f)** $Bi_{1.75}Sb_{0.25}Te_{1.85}Se_{1.15}$ [26]; **(g)** $Bi_{1.5}Sb_{0.5}Te_{1.7}Se_{1.3}$; **(h)** $BiSbTeSe_2$ [27]

1.8 Signatures of TI in transport measurements

In the earlier sections, the examples drawn from literature that demonstrate the Dirac cone like dispersion of the surface states in some 3D TI using ARPES were shown. Since these surface states form a metallic sheet encompassing the 3D insulating bulk, it will be interesting to inquire if the quantum hall like plateaus can be seen in the transport measurements. Although there have been several investigations of magneto-transport in the strong 3DTI, the observation of these QHE like plateaus have eluded experiments; primarily due to the fact that the bulk is not truly gapped as a consequence of the presence of intrinsic defects and disorder in the system, leading to the observation of much lower mobility of ~ 1000 cm^2/Vs in the 3D TI crystals until very recently, where with special care the Hall plateaus and zero longitudinal resistance has been observed [28]. Similar to the QHE state, where for very low magnetic fields Shubnikov de Haas (SdH) oscillations were observed (ref. Figure 1.2), in most 3D TIs the SdH oscillations have been observed, as also in the present thesis. In addition, akin to the situation in QSH insulator, Weak Anti Localization (WAL) is also observed in some TI samples, when the phase coherence length l_φ is greater than the mean free path l of the electron. These two phenomena have been observed in several investigations, and formed a part of the studies presented in this thesis; and therefore a brief review of the phenomenon is given below [29].

The book titled “Semiconductor Nanostructures: Quantum States and Electronic Transport” [30] by Thomas Ihn has been referred for the theory and derivation of SdH oscillations and WAL phenomena, presented below.

1.8.1 Shubnikov de Haas (SdH) oscillations

The Shubnikov de Haas oscillations are the oscillations in the longitudinal resistivity/conductivity of a material observed at low temperatures in the presence of very high magnetic fields. The phenomenon can be explained as follows: In a 2D electron gas confined to the *xy*-plane and subjected to a strong external magnetic field in the *z*-direction (as shown in Figure 1.17), the electrons execute cyclotron motion and their orbits get quantized.

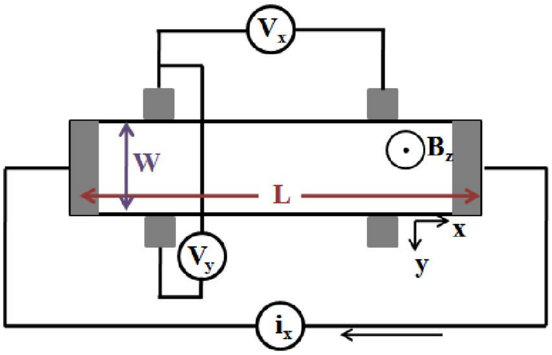

Figure 1.17 – Magneto-resistance measurement geometry of a 2DEG system with sample dimensions of length *L* and width *W*

The Hamiltonian of an electron in the presence of an Electromagnetic field is

$$H = \frac{1}{2m^*}\left(\bar{p} + |e|\bar{A}\right)^2 + V(z) \qquad (1.1)$$

Where *V(z)* is the potential and the vector potential is chosen to be $\bar{A} = (-By, 0, 0)$.

The Hamiltonian can then be split into xy and z components as

$$H_{xy} = \frac{1}{2m^*}\left[(p_x - eB_z y)^2 + p_y^2\right] \qquad (1.2)$$

$$H_z = -\frac{\hbar^2}{2m^*}\frac{\partial^2}{\partial z^2} + V(z) \qquad (1.3)$$

The H_z is independent of the magnetic field and depends only on the *z*-coordinate. The solution of H_{xy} can be obtained by using the trial solution $\psi(x,y) = e^{ik_x x}\eta(y)$ which leads to the equation

$$\left[\frac{p_y^2}{2m^*} + \frac{1}{2}m^*\omega_c^2\left(y - \frac{\hbar k_x}{|e|B_z}\right)^2\right]\eta k_x(y) = E\eta k_x(y) \qquad (1.4)$$

Here, $\omega_C = \frac{|e|B}{m^*}$ is the cyclotron frequency. This equation is that of a 1D quantum mechanical oscillator centred at $y_0 = \frac{\hbar k_x}{|e|B}$. The solution of the equation is given by

$$E_n = \hbar\omega_c\left(n + \frac{1}{2}\right) \tag{1.5}$$

The quantum states with different quantum numbers k_x but with same quantum numbers n are energetically degenerate. These states are called Landau Levels (LLs). The energy of each and every given Landau Level increases linearly with magnetic field which leads to the Landau Fan (shown in Figure 1.18).

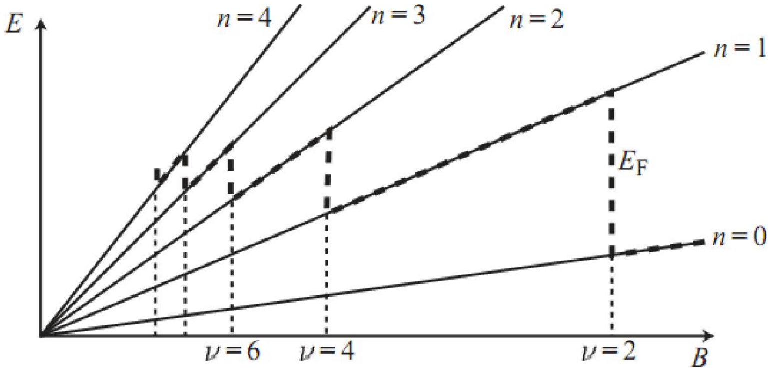

Figure 1.18 – Energy levels for electrons in a magnetic field. The energy of the Landau levels increases linearly with the magnetic field resulting in a fan-like diagram. The slope of each Landau level line depends on the quantum number *n*. At a fixed electron density in the electron gas, the Fermi energy oscillates as a function of the filling factor (adopted from [30]).

The degeneracy of a Landau level is determined by the dimensions of the structure. If *L* is the sample length and *W* is the sample width (as shown in Figure 1.17), then the centre coordinate $y_0 = \frac{\hbar k_x}{eB}$ should lie within the width W of the structure, i.e., $0 \le \frac{\hbar k_x}{eB} \le W$. The density of k_x states for the above 2D system is L/2π. Hence good k_x-values fulfil the condition $0 \le \frac{k_x L}{2\pi} \le \frac{eB}{hA}$, where $A = WL$ is the area of the sample. Thus the number of allowed k_x states per unit area is given as $n_L = \frac{|e|B}{h}$. If an electron gas has the electron density n_s, the number $\nu = \frac{n_s}{n_L}$ tells us the number of Landau levels that are occupied at a given external magnetic field at zero temperature. Therefore, $\nu = \frac{hn_s}{|e|B}$ is called the filling factor corresponding to the magnetic field B. At fixed electron density n_s, the Fermi level of the electron gas oscillates as a function of B, i.e., with filling factor ν in a 1/B periodic fashion as shown in Figure 1.18. This energy spectrum consists of discrete LLs which are determined by the external magnetic field. The Density of States (DOS) is described as delta function located at E_n and is given by

$$D_{2D}(E,B) = \frac{|e|B}{h} \sum_{n,\sigma=\pm} \delta\left(E - E_n^{(\sigma)}\right) \tag{1.6}$$

At temperatures above 0 K, scattering events such as intra and inter-Landau Level scattering can limit the lifetime of an electron in a particular quantum state and consequently broaden the ideal delta function shaped DOS. Consequently, the DOS of an individual LL with a quantum number n is given as

$$D_{2D}(E,B) = 2n_L \sum_{n\to\infty} L_n\left(E - \hbar\omega_c\left(n + \frac{1}{2}\right)\right) = \frac{m^*}{\pi\hbar^2}\left[1 - 2e^{-\pi/\omega_c\tau_q}\cos\left(2\pi\frac{E}{\hbar\omega_c}\right)\right] \tag{1.7}$$

From classical Drude's model, the Ohm's law is given as $\bar{j} = \sigma\bar{E}$. This can be expressed in tensor notation as

$$\begin{bmatrix} j_x \\ j_y \end{bmatrix} = \begin{bmatrix} \sigma_{xx} & \sigma_{xy} \\ -\sigma_{xy} & \sigma_{xx} \end{bmatrix} \begin{bmatrix} E_x \\ E_y \end{bmatrix} \tag{1.8}$$

Where

$$\begin{bmatrix} \sigma_{xx} & \sigma_{xy} \\ -\sigma_{xy} & \sigma_{xx} \end{bmatrix} = \begin{bmatrix} \rho_{xx} & \rho_{xy} \\ -\rho_{xy} & \rho_{xx} \end{bmatrix}^{-1} \tag{1.9}$$

Applying the Fermi Dirac distribution, the density of states for a 2D system and the Drude's model, the resistivity tensor component ρ_{xx} is obtained as

$$\rho_{xx} - \rho_0 = \left(\frac{\hbar\omega_c}{2\varepsilon_F}\right)^{1/2} \frac{\left(\frac{2\pi^2 k_B T}{\hbar\omega_c}\right)}{\sin\left(\frac{2\pi^2 k_B T}{\hbar\omega_c}\right)} e^{-\left(\frac{2\pi^2 k_B T_D}{\hbar\omega_c}\right)} \cos\left(\frac{1}{2}\pi g \frac{m_0}{m^*}\right) \cos\left[2\pi\left(\frac{F}{B} + \frac{1}{2} - \beta\right)\right] \tag{1.10}$$

The above equation 1.10 is called the Lifshitz-Kosevich (L-K) [31] equation and can be rewritten as

$$\Delta\rho_{xx} = A_0 R_T R_D R_S \cos\left[2\pi\left(\frac{F}{B} + \frac{1}{2} - \beta\right)\right] \tag{1.11}$$

The various terms present in the L-K equation are defined below.

i. ρ_{xx} = longitudinal resistivity

ii. ρ_0 = classical Drude resistivity around which the MR oscillates with a period 1/B

iii. E_F = Fermi energy

iv. T_D = Dingle temperature

v. $\left(\frac{\hbar\omega_c}{2E_F}\right)$ = constant = A_0;

vi. $\frac{\left(\frac{2\pi^2 k_B T}{\hbar\omega_c}\right)}{\sinh\left(\frac{2\pi^2 k_B T}{\hbar\omega_c}\right)}$ = Temperature damping factor = R_T, reduces the amplitude of oscillations as a result of energy averaging over $k_B T$ around Fermi energy

vii. $e^{-\left(\frac{2\pi^2 k_B T_D}{\hbar\omega_c}\right)}$ = Dingle damping factor = R_D accounts for the finite lifetime broadening of the LL

viii. $cos\left(\frac{1}{2}\pi g\frac{m_0}{m^*}\right)$ = Spin damping factor = R_s

ix. m_0 = rest mass of electron

x. m^* = effective mass

xi. F = Frequency of oscillations

xii. β = phase factor that accounts for the phase shift

These oscillations described by equation 1.10 in resistance versus magnetic field are called the Shubnikov de Haas (SdH) oscillations and are fitted to the observed magneto-resistance in the 3D TI.

It should be noted that there lies a major difference between the Landau quantization of normal fermions which obey a parabolic E vs. k dispersion and the Dirac fermions which have linear E vs. k dispersion. While the Landau quantization of the energy states for the former is of the form given by Eqn. 1.5, for Dirac fermions it occurs as [13]

$$E_{\pm n} = \pm\sqrt{\left(2e\hbar v_F^2 Bn\right)/c} \tag{1.12}$$

Where n = 0, 1, 2...

Thus while the spacing between two LLs in normal metals is a constant ($\hbar\omega_c$), as shown in Figure 1.3; the spacing in Dirac systems is not constant and changes as $\sqrt{n}$. The equation 1.12 is an indication of the presence of a zeroth LL occurring at the Dirac Point (DP). Figure 1.19(a) shows the partially filled Dirac cone and Figure 1.19(b) shows the Landau quantization of the Dirac cone in the presence of a magnetic field. The zeroth LL is marked by n = 0.

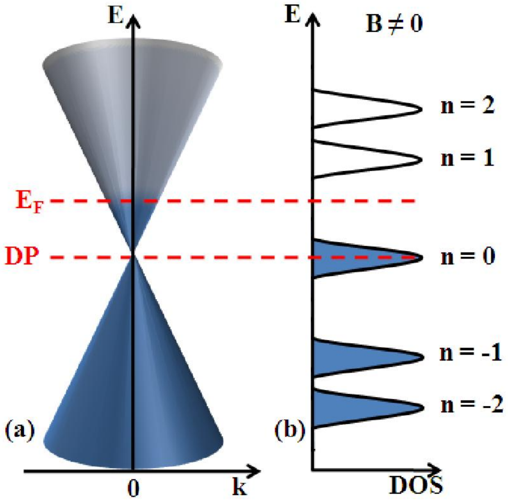

Figure 1.19 – **(a)** partially filled Dirac cone; **(b)** Landau quantization of the Dirac cone, n = 0 marks the zeroth LL at the Dirac point (DP). E_F is the Fermi level (adopted from [13])

Analysis of the SdH oscillations plays an important role in the studies of 3D TIs for two reasons.

(a) It provides a means to selectively and quantitatively characterize the 2D surface states that coexist with 3D bulk states by looking at the angular dependence of the SdH oscillation. The measurement geometry during MR is illustrated in Figure 1.20 below. C_1, C_2, C_3 are the three axis of the crystal and H is the applied magnetic field strength.

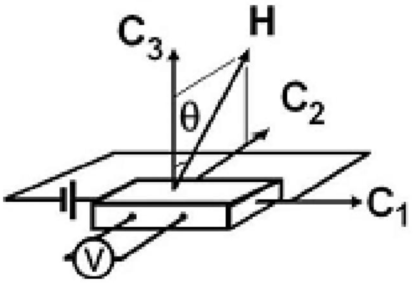

Figure 1.20 – Magneto-resistance measurement geometry. C_1, C_2, C_3 are the three axis of the crystal and H is the applied magnetic field strength

According to theory of angular dependent magneto-resistance measurements, the positions of maxima and minima in SdH oscillations in $1/B$ depend only on the perpendicular component of field $(B_\perp)$ as $(B_\perp)^{-1} \equiv (B\cos\theta)^{-1}$, where θ is the angle between the field direction and the normal to the crystal surface, which varies as 0° < θ < 90° [13]. For a 3D Fermi surface, the minima and maxima positions in oscillations would vary as $(B\cos\theta)^{-1}$ and oscillations would be observed in the measurement at all angles from 0° to 90°. For a 2D Fermi surface, which would be the case for the TSS, the minima and maxima positions in SdH oscillations will not change with $(B_\perp)^{-1}$ and oscillations would cease to exist at θ = 90°. Thus if the oscillations are observed only in the $H \| C_3$ direction, it can be surmised that the origin of oscillations are associated with that of a 2D Fermi surface, whereas, if the oscillations are observed in both $H \| C_3$ and $H \| C_1$-C_2 directions, then the SdH oscillations arise from a 3D Fermi surface.

(b) The phase factor of the oscillations directly reflects the Berry phase of the system, from which we can elucidate whether the electrons showing the SdH oscillations are Dirac fermions or not. The TSS has a 2D Fermi surface with linear *E* vs. *k* dispersion while the normal fermions have a parabolic *E* vs. *k* relation. From equation 1.10 we know that in the SdH oscillations, resistivity and hence conductivity oscillates periodically as a function of 1/B and the oscillatory part of the longitudinal conductivity σ_{xx} follows the relation

$$\Delta\sigma_{xx} \sim \cos\left[2\pi\left(\frac{F}{B}+\frac{1}{2}-\beta\right)\right] \tag{1.13}$$

The phase factor β is the same one which appears in the Onsager's semi-classical quantization condition [31]

$$A_N = \frac{2\pi e}{\hbar c} B\left[n + \frac{1}{2} - \beta\right] \tag{1.14}$$

Where, A_N is the area enclosed by electrons in the k-space with their cyclotron orbits on the Fermi surface and β is the Berry phase γ divided by 2π. The value of β for fermions with a parabolic dispersion is 0 and for Dirac fermions with a linear dispersion is 0.5 [13].

When the E_F lies at the centre of a LL, the DOS takes a maximum and when the E_F lies in between two neighbouring LLs, the DOS takes a minimum. In the latter situation, a certain number of LLs are completely filled and the next LL is empty. Therefore, a minimum in σ_{xx}, which occurs when DOS takes a minimum, implies that some n LLs are filled, and hence we can assign an integer index n to that minimum. In ordinary metals, this LL index n corresponds to the filling factor ν. This is akin to the situation in the ordinary quantum Hall effect (ref. Figure 1.2), in which σ_{xy} is quantized to $\nu e^2/h$ and σ_{xx} becomes zero when the chemical potential lies between ν and $(\nu+1)^{th}$ LLs. In the case of Dirac fermions, the filling factor is not n but is n+1/2, because of the half-integer quantization that arises from the existence of the zeroth LL (Figure 1.19) [13]. The phase factor in the SdH oscillations can be experimentally determined from an analysis of the LL fan diagram, wherein the sequence of the values of $1/B_n$ corresponding to the n^{th} minimum in $\sigma_{xx,}$ are plotted versus n. From equation 1.12 it is clear that the n^{th} minimum occurs when following condition occurs

$$\frac{2\pi e}{\hbar c} B\left[n + \frac{1}{2} - \beta\right] = (2n-1)\pi \tag{1.15}$$

Thus the slope of a plot of $1/B_n$ vs. n corresponds to the oscillation frequency and the extrapolation of the linear fit to the LL fan diagram to $1/B_n \rightarrow 0$ gives an intercept on the n axis, as the phase factor β.

1.8.2 Weak Localization (WL) and Weak Antilocalization (WAL)

The electron conduction in solids involves various characteristic lengths

(a) Mean free path (l) – defined as the average distance travelled by the electron between successive collisions with impurities or phonons (Drude model). This is a classical quantity and is given by $l = v\tau$, where v is the velocity of the electron and τ is the relaxation time

(b) De-Broglie wavelength (λ) – this arises as a consequence of electron being a quantum mechanical object and is defined as

$$\lambda = \frac{2\pi}{k} \tag{1.16}$$

Where k = wave-vector. For fermions $k = k_F$ Fermi wave-vector and the De-Broglie wavelength is called Fermi wavelength λ_F.

(c) Phase coherence length (l_φ) – the state of the electron is quantum mechanics is defined by a wave function that includes a phase. The phase coherence length is the characteristic length over which the scattered electron retains its original phase and is given by

$$l_\varphi = \sqrt{D\tau_\varphi} \tag{1.17}$$

Where D – diffusion constant and τ_φ – time over which the electron undergoes elastic collisions. The diffusion constant is given by $D = \frac{vl}{d}$ where d is the dimensionality of the electron gas. The phase decoherence for the electron can occur only by scattering processes that break time reversal symmetry e.g. spin-flip by application of an external magnetic field.

Based on the relation between the mean free path "l" and the sample dimensions, the transport in solids can be classified as –

(i) Ballistic: $l << L, W$; L = length of the sample, W = width of the sample

(ii) Quasi-ballistic: $W < l < L$

(iii) Diffusive: $l > L, W$, which can be further divided into

(a) Semi-classical diffusive regime: $l_\varphi \leq l$; this gives Drude's conductivity

(b) Quantum diffusive regime: $l_\varphi >> l$; quantum interference between time reversed paths gives rise to quantum correction to the conductivity. This gives rise to phenomena such as Weak Localization (WL) and Weak Antilocalization (WAL).

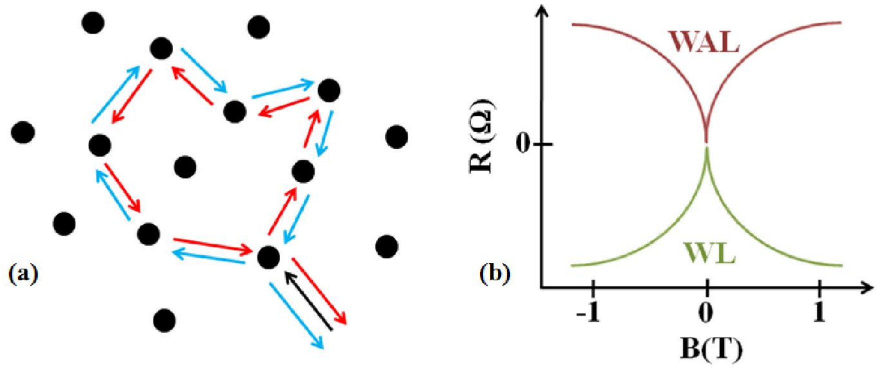

Figure 1.21 – **(a)** the two time reversed paths for a scattered electron wavefunction; **(b)** WL and WAL signatures in magneto-resistance

Weak localization (WL) is a phenomenon that is observed in systems that preserve Time Reversal Symmetry (TRS). It occurs when an electron is scattered sequentially in a loop by impurities distributed randomly in the conductor, whereby the electrons are weakly localized in the loop as a result of constructive interference of the wave functions. Figure 1.21(a) shows an example of the two time-reversed paths of an electron during scattering from disorders. The two partial waves traverse the same paths, in opposite directions during scattering. If A^+ and A^- are the quantum mechanical amplitudes of the two paths, the probability of the paths to return to the starting point and backscatter is given as

$$P = [P_{classical}] + \{P_{quantum}\} \tag{1.18}$$

$$\Rightarrow P = \left|A^{+} + A^{-}\right|^{2} = \left[\left|A^{+}\right|^{2} + \left|A^{-}\right|^{2}\right] + \left\{A^{+} \cdot A^{-*} + A^{+*} \cdot A^{-}\right\} \qquad (1.19)$$

Where the first two terms inside the square brackets are classical contribution to resistance from Drude-Boltzmann theory $P_{classical}$ and the last two terms inside the flower brackets are the quantum mechanical interference terms $P_{quantum}$. In the absence of an external magnetic field, Time Reversal Symmetry is preserved and thus

$$A^{+} = A^{-} \equiv A \qquad (1.20)$$

$$\Rightarrow P_{classical} = 2\left|A\right|^{2} \qquad (1.21)$$

$$\Rightarrow P_{quantum} = 4\left|A\right|^{2} \qquad (1.22)$$

Thus there is an enhanced back-scattering and an increase in resistance in the system is observed. The semi classical expression for the weak localization correction to the conductivity is then given by

$$\frac{\delta\sigma_{m}}{\sigma} \approx -\frac{1}{k_{F} l} ln \frac{l_{\varphi}}{l} \qquad (1.23)$$

Where, k_F is the Fermi wave-vector. As seen from (1.23), the correction is logarithmic in behaviour with a negative contribution to the conductivity.

In the presence of a strong spin-orbit interaction (SOI), the quantum correction arising out of the phase coherent back-scattering changes a little. The presence of a strong SOI leads to spin rotation during scattering events. An intuitive way to visualize the spin rotation is to assume that the spin diffusing on a Bloch sphere (as shown in Figure 1.22)

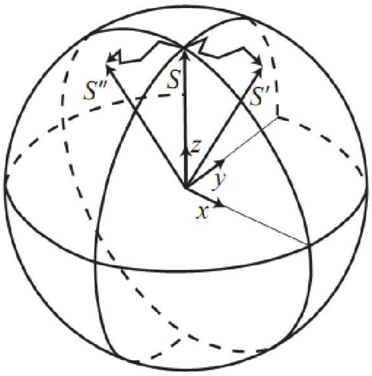

Figure 1.22 – Spin diffusion on the Bloch sphere (adopted from [30])

Let the partial wave start with a particular spin state $|s\rangle$. After it traverses along the loop and reaches the origin, its new state is given by

$$|s'\rangle = R|s\rangle \tag{1.24}$$

Where *R* is the rotation operator and defined as the product of the number of rotations that had occurred during the completion of the loop $R = R_n......R_3R_2R_1$. For the time reversed path, the final state is given by

$$|s''\rangle = \overline{R}|s\rangle \tag{1.25}$$

Where $\overline{R} = \overline{R_n}......\overline{R_3}\,\overline{R_2}\,\overline{R_1}$ and $R_m\overline{R_m} = 1$

The total probability for backscattering is then given by

$$\left(|s'\rangle + |s''\rangle\right)\cdot\left(\langle s'| + \langle s''|\right) = 2 + \langle s'|s''\rangle + \langle s''|s'\rangle \tag{1.26}$$

Where, the interference contribution is given as - $\langle s''|s'\rangle = \langle \overline{R}s|Rs\rangle = \langle s|R^2|s\rangle$.

Now, let l_{SO} and τ_{SO} be the characteristic length and the characteristic time scale respectively, over which the spin orientation doesn't change during scattering. In the case of weak SOI i.e. $l_{SO} < l_\varphi$, the spin stays polarized in the same direction throughout the scattering process which implies $R = 1$ and hence the back-scattering is enhanced. This situation is akin to the Weak localization phenomenon discussed before. In the case of strong SOI i.e. $l_\varphi < l_{SO}$, the spin gets completely randomized. However the spin randomization directions for the two time-reversed paths are in complete opposite directions throughout the scattering process in the loop. Here, evaluation of R^2 becomes necessary. Solving for it we get $\langle s|R^2|s\rangle = -\frac{1}{2}$.

Thus the total back-scattering probability is given as

$$\left(|s'\rangle + |s''\rangle\right)\cdot\left(\langle s'| + \langle s''|\right) = 2 + \langle s'|s''\rangle + \langle s''|s'\rangle = 2 + 2\langle s'|R^2|s''\rangle = 2 + 2(-\tfrac{1}{2}) = 1 \qquad (1.27)$$

Thus the presence of a strong spin-orbit interaction reduces the back-scattering probability by half of the classical contribution and hence the conductivity increases. Hikami, Larkin and Nagaoka (HLN) had derived an analytical expression to describe the WL-WAL phenomena in 2D systems. The HLN equation is given as

$$\delta\sigma(B) = \alpha\frac{e^2}{h}\left[\ln\left(\frac{B_\varphi}{B}\right) - \psi\left(\frac{1}{2} + \frac{B_\varphi}{B}\right)\right] \qquad (1.28)$$

Where ψ = Digamma function; $B_\varphi = \frac{\hbar}{4el_\varphi}$; $l_\varphi = \sqrt{D\tau_\varphi}$ is the phase coherence length and α is a constant. For WL $\alpha = 1$ and for WAL $\alpha = -0.5$.

In Topological Insulators, since the spin of the electron is locked to its momentum, the spin direction in the two time-reversed paths is always in opposite directions to each other. As already described in Section 1.6, for a closed orbit around the Fermi surface of a TI a π Berry phase is accumulated. Thus the two time reversed paths acquire phases of $+\frac{\pi}{2}$ and $-\frac{\pi}{2}$ and the π Berry phase thus leads to destructive interference. The constant term α from the HLN equation is then used as a counter to detect the number of 2D transport channels. For example, if $\alpha = -0.5$ then only one conducting SS is present etc.

Thus, both SdH oscillations and WAL phenomena act as indicators of the presence of TSS in the system via the Berry phase obtained from the Landau Level Fan diagram analysis of SdH oscillations and the value of α from HLN analysis of the WAL data respectively. A Berry phase of 0.5 or the value of α being close of -0.5 indicates that the transport is dominated by contribution from the TSS.

1.9 Transport studies on single crystals of 3D TI system Bi_2Se_3

It has been indicated that to harness the transport from TSS of 3D TI, there should be no interference from the bulk conduction. In realistic crystals this is seldom possible, because Bi_2Se_3 and its related systems are host to a lot of defects and disorder. As the interest of this thesis lies on studying the transport in single crystals of Bi_2Se_3, the following literature review restricts itself to the same.

The strong 3D TI Bi_2Se_3 is a small band-gap semiconductor (0.3 eV) that crystallizes in the $R\bar{3}m$ space group. It has a tetradymite structure that consists of repeating Se1-Bi-Se2-Bi-Se1 units called quintuples (QLs). The unit cell consists of 3 such QLs held together by Van der Waals interaction, stacked along the hexagonal c-axis [0001] direction. Se1 and Se2 are two non-equivalent positions with the Se2 playing the role of centre of inversion in the crystal structure. The nature of bonding between the atoms in a QL is covalent. Figure 1.23 shows the crystal structure of Bi_2Se_3.

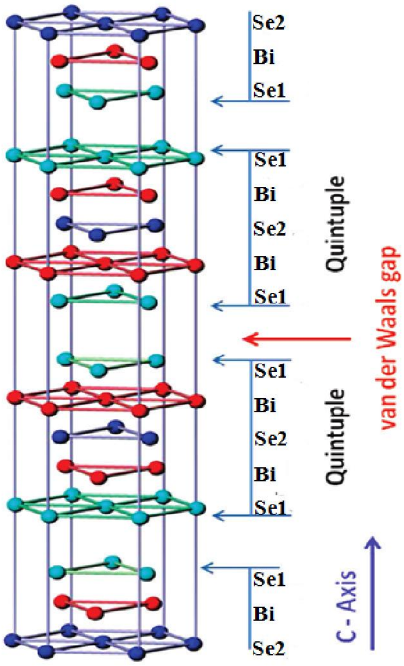

Figure 1.23 – The crystal structure of Bi_2Se_3 indicating the Quintuple layers and the location of the van der Waals gap [32]

Bi_2Se_3 has the inherent thermodynamic defects – a) anion vacancy V_A (V_{Se1}) which is a double donor, b) cation antisite C_A (Bi_{Se}) which is a single donor and anion antisite A_C (Se_{Bi}) which is again a single donor. The cation vacancy V_C (V_{Bi}) is the sole acceptor (triple acceptor) [33][34]. As grown Bi_2Se_3 crystals have always been found to be electron doped, with the bulk carrier concentration of ~ 10^{19} cm^{-3}. Ab-initio calculations by D. West et al. [33] and L. Xue et al. [34] have suggested based on the energy of formation, that the major defects in the system are Se vacancies (V_{Se1}) and Se anti-site defects (Se_{Bi}). Y. S. Hor et al. [35] reported p-type crystals by substituting low concentrations of Ca (~ 1%) at Bi site, where the E_F was shifted closer to the valence band lying below the Dirac Point. However the transport in these samples still displays metallic behaviour. J. G. Checkelsky et al. [36] observed that on doping Ca^{2+} to the Bi^{3+} site, the number of charge carriers were reduced and the temperature coefficient of resistivity changed sign from positive to negative i.e. the bulk went from being metallic to displaying semi-conducting character ($0.002 < x < 0.0025$, $\rho_{4.2K} = 80$ mΩ-cm) in the transport. However no signatures of surface states viz., 2D Shubnikov de

Haas oscillations, were observed in the single crystals as Ca doping introduced strong scattering centres and the electron mobility was reduced in Ca-doped Bi_2Se_3 system. N. P. Butch et al. [37] obtained Bi_2Se_3 crystals with carrier concentration as low as 10^{16} cm^{-3} by varying the bismuth/selenium ratios and the heating conditions. However the samples still displayed metallic behaviour in transport except for shallow local minima below 30 K, beyond which the resistivity showed an upturn. SdH oscillations associated with the TSS were not observed in the magneto-transport measurements in these low carrier density crystals too. Analytis et al. [38] achieved low carrier concentrations of the order ~ 10^{16} cm^{-3} by partially substituting for Bi by Sb, in which signatures from the TSS were observed in the single crystals of Bi_2Se_3. The crystal reached the quantum limit, that is, the point where a magnetic field can collapse the bulk carriers to their lowest Landau level. Beyond this field surface states could be seen clearly. However, no n-to-p type transition was achieved via this route. Ren et al. [39] achieved bulk semiconducting behaviour and a low temperature resistivity of 1Ω-cm in Te doped Bi_2Se_3 system with the composition Bi_2Te_2Se. This was possible because the compound Bi_2Te_2Se naturally crystallizes in a chalcogen-ordered structure with Te-Bi-Se-Bi-Te QL units. This structure brings out a two-fold advantage. Firstly, as Se occupies the centre of the QL, it cannot escape easily as in Bi_2Se_3 and hence the number of Se vacancies is reduced. Secondly, the larger electro-negativity of Se in comparison to Te makes Bi bond strongly with Se than Te reduces and hence discourages the formation of Bi/Te antisite defects as observed in Bi_2Te_3. Thus nearly bulk-insulating behaviour was achieved in the system. In addition, its ordered structure improved the mobility of carriers so that topological surface states characteristics remain unmasked in the material. Ren et al. [40] were able to tune the charge carrier type in single crystals of Bi_2Se_3 to obtain high bulk resistivity and clear quantum oscillations by combining Cd doping and a Se-rich crystal-growth condition. They obtained a p-type Bi_2Se_3 which underwent a p-to-n-type conversion upon gradually increasing the Se vacancies by post annealing. With the optimal annealing condition, they achieved resistivity value in excess of 0.5 Ω-cm at 1.8 K and were able to observe two-dimensional Shubnikov–de Haas oscillations composed of multiple frequencies in magnetic fields below 14 T. Ren et al. [41] and Taskin et al. [42] synthesized crystals with higher bulk insulating characteristic by substituting Sb at Bi site in $Bi_2Te_{3-y}Se_y$. In this system, Se occupies the middle of the QL similar to that observed in Bi_2Te_2Se. In addition, the Bi/Sb ratio in the cation layers and the Te/Se ratio in the outer layers affect the levels of acceptors and donors, respectively, making it possible to achieve a maximally compensated situation. It was noticed that a reasonably bulk-insulating behaviour was observed for a series of compositions (x, y) in the compound $Bi_{2-x}Sb_xTe_{3-y}Se_y$ with the highest being 10 Ω-cm for the composition $BiSbTeSe_2$. Xiong et al. [43] reported Te doped Bi_2Te_2Se crystals with insulating characteristics and a low temperature resistivity value of 6 Ω-cm and concluded that SdH oscillations from the Topological surface states were observed. Bao et al. [25] synthesized single crystals of the Te doped Bi_2Se_3 system Bi_2Se_2Te with highly insulating behaviour (420 Ω at 4.2 K) and observed signatures of TSS viz. SdH oscillations and Weak Antilocalization (WAL) in transport. Paul Syers et al. [44] devised a new synthesis method for achieving stoichiometric Bi_2Se_3 crystals that exhibit non-metallic behavior in electrical transport down to low temperatures, without the use of gating techniques. Hall Effect measurements indicated the presence of both electron- and hole-like carriers, and the latter were identified with topological surface state.

1.10 Approach of investigation in the current thesis

While the traditional approach to bring out TSS signatures in magneto-transport measurements has been focused on tuning the Fermi level into bulk band-gap by charge compensation; a recent article by Brahlek et al. [45] put forth a new idea where the TI system

Bi_2Se_3 was studied from the point of view of a semiconductor/metal interface wherein interface phenomena at the semiconductor/metal interface has been invoked. Since Bi_2Se_3 is a bulk semiconductor whose Fermi level is pinned to the conduction band because of thermodynamic defects and as it also hosts the metallic surface states, it has two Fermi levels viz. the bulk and surface Fermi levels. The presence of two distinct Fermi levels makes the system vulnerable to interface phenomena such as band bending.

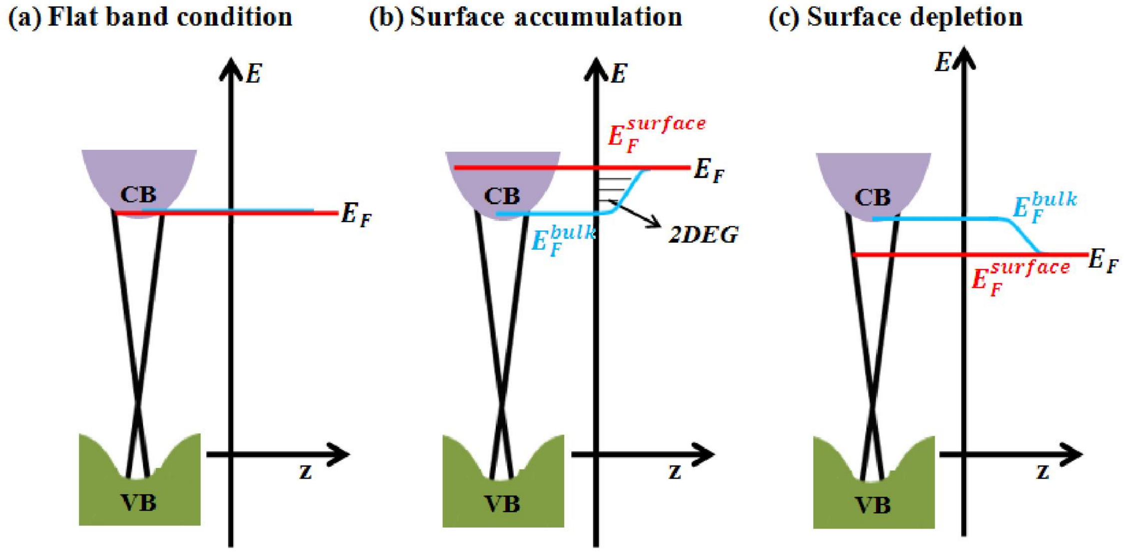

Figure 1.24 – **(a)** Flat band condition where both the Fermi levels are already in equilibrium; **(b)** Downward band-bending leading to accumulations of carriers at the interface; **(c)** Upward band-bending leading to depletion of charge carriers at the surface (adopted from [45])

Band bending happens when there is a large mismatch between the surface and bulk Fermi levels and upon equilibration, the bulk band shifts near the surfaces. This shift has can be either upward or downward. In the case of an upward shift (as shown in Figure 1.24(c)) the carriers at the interface get depleted, while in the downward case it leads to an accumulation region near the surface (as shown in Figure 1.24(b)). This downward bending gives rise to a conventional two dimensional electron gas (2DEG) at the surface (ref. Figure 1.24(b)). The presence of such a conventional 2DEG due to band-bending has been reported by Bianchi et al. [46] in detailed ARPES measurements (shown in Figure 1.25) on Bi_2Se_3.

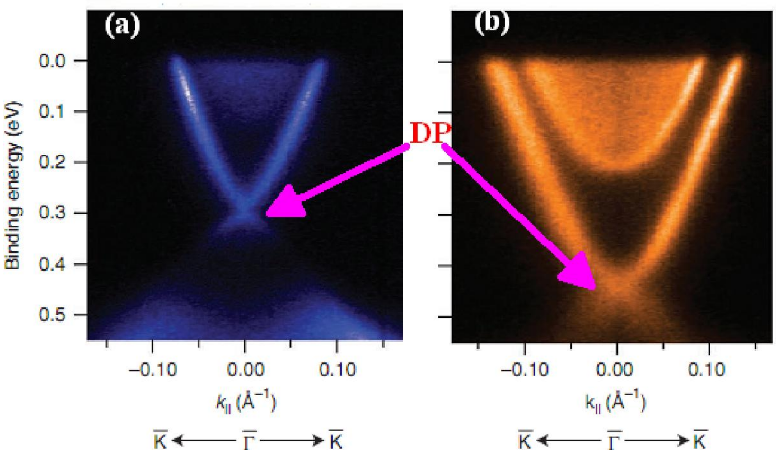

Figure 1.25 – ARPES of Bi_2Se_3 (0001) crystal. **(a)** Spectrum collected 30 min after cleaving the crystal. The sharp V-type feature corresponds to the Dirac like dispersion of the TSS. The Dirac Point, denoted as DP is marked using the arrow in pink. The valence band states are visible below the Dirac point and the diffuse intensity inside the Dirac cone is due to the filled bottom of the conduction band; **(b)** Spectrum collected after 3 hours exposure of the crystal surface. The chemical potential and hence the DP is seen shifted downwards towards the conduction band. The sharp rim around the bottom of the conduction band marks the spectral signature of a 2DEG state (adopted from [46]).

Brahlek et al. attributed the absence of SdH oscillations in Bi_2Se_3 in earlier studies [36][37] to the presence of the downward band-bending in the system as the systems with a downward band bending have very large Fermi surface which leads to very small period of oscillations. Additionally, the band-bending leads to the formation of quantum well states that are 2D in nature and hence quantum oscillations from transport in them would dominate in a measurement. Hence it is essential to realize an upward band-bending in the system, so that SdH oscillations from the TSS would show up in magneto-transport measurements. Also taking into consideration the fact that the single crystals of Bi_2Se_3 that have been synthesized always showed very low mobilities, Brahlek et al. applied the Ioffe-Regel criterion and found that Bi_2Se_3 lies in the region known as bad metal ($k_F l = 0.3-3$) where the mean free path of the carriers l is very small.

From the above discussion it is amply evident that disorder/defects interfere with the contribution from TSS in transport behaviour. Thus a systematic investigation of transport behaviour with well characterised disorder deliberately introduced is much needed and the work presented in the current thesis is based on this premise. Chapter 3 focuses on studying the role of defects in achieving Quantum oscillations in magneto-transport from surface states by introducing weak and strong disorder by varying the growth conditions of Bi_2Se_3 single crystals. The role of substitutional disorder and its effect on magneto-transport behaviour of Bi_2Se_3 are studied in Chapter 4 (Sb substitution) and Chapter 5 (Te substitution). In addition to this, the effect of high pressure on the transport properties of the Te substituted Bi_2Se_3 system is studied in Chapter 6.

References

[1] K. von Klitzing, G. Dorda, and M. Pepper, *Phys. Rev. Lett.* **45** (1980) 494

[2] D. J. Thouless, M. Kohmoto, M. P. Nightingale, and M. den Nijs, *Phys. Rev. Lett.* **49** (1982) 405

[3] Daniel R. Cooper, Benjamin D'Anjou, Nageswara Ghattamaneni, Benjamin Harack, Michael Hilke, Alexandre Horth, Norberto Majlis,Mathieu Massicotte, Leron Vandsburger, EricWhiteway, and Victor Yu, *ISRN Condensed Matter Physics* **2012** (2012) 501686

[4] F. D. M. Haldane *Phys. Rev. Lett.* **61** (1988) 2015

[5] M. O. Goerbig, arXiv:0909.1998

[6] *Contemporary Concepts of Condensed Matter Science – Topological Insulators*, edited by Franz Marcel and Molenkamp Laurens,Vol. 6 (Elsevier) 2013

[7] D. P. DiVincenzo, E. J. Mele, *Phys. Rev. B* **29** (1984) 1685

[8] G. W. Semenoff, *Phys. Rev. Lett*. **53** (1984) 2449

[9] Serhii Shafraniuk, *Graphene: Fundamentals, Devices and Application*, (Pan Stanford Publishing) 2015

[10] C. L. Kane and E. J. Mele *Phys. Rev. Lett.* **95** (2005) 146802

[11] C. L. Kane and E. J. Mele, *Phys. Rev. Lett.* **95** (2005) 226801

[12] H. A. Kramers, *Proc. Amsterdam Acad.* **33** (1930) 959

[13] Y. Ando, *J. Phys. Soc. Jpn.* **82** (2013) 102001

[14] L. Fu, C. L. Kane, and E. J. Mele, *Phys. Rev. Lett.* **98** (2007) 106803

[15] J. E. Moore and L. Balents, *Phys. Rev. B* **75** (2007) 121306(R)

[16] Hari C. Manoharan, *Nature Nanotechnology* **5** (2010) 477

[17] L. Fu and C. L. Kane, *Phys. Rev. B* **76** (2007) 045302

[18] B. A. Bernevig, T. L. Hughes, and S.-C. Zhang, *Science* **314** (2006) 1757

[19] D. Hsieh, D. Qian, L. Wray, Y. Xia, Y. S. Hor, R. J. Cava, and M. Z. Hasan, *Nature* **452** (2008) 970

[20] Haijun Zhang, Chao-Xing Liu, Xiao-Liang Qi, Xi Dai, Zhong Fang & Shou-Cheng Zhang, *Nature Physics* **5**, (2009) 438

[21] Y. Xia, D. Qian, D. Hsieh, L. Wray, A. Pal, H. Lin, A. Bansil, D. Grauer, Y. S. Hor, R. J. Cava & M. Z. Hasan, *Nature Physics* **5**, (2009) 398

[22] Y. L. Chen, J. G. Analytis, J. -H. Chu, Z.K. Liu, S. -K. Mo, X. L. Qi, H. J. Zhang, D. H. Lu, X. Dai, Z. Fang, S. C. Zhang, I. R. Fisher, Z. Hussain, and Z.-X. Shen, *Science* **325** (2009) 178.

[23] D. Hsieh, Y. Xia, D. Qian, L. Wray, F. Meier, J. H. Dil, J. Osterwalder, L. Patthey, A. V. Fedorov, H. Lin, A. Bansil, D. Grauer, Y. S. Hor, R. J. Cava, and M. Z. Hasan, *Phys. Rev. Lett.* **103** (2009) 146401.

[24] Su-Yang Xu, L. A. Wray, Y. Xia, R. Shankar, A. Petersen, A. Fedorov, H. Lin, A. Bansil, Y. S. Hor, D. Grauer, R. J. Cava, M. Z. Hasan, arXiv:1007.5111

[25] Lihong Bao, Liang He, Nicholas Meyer,Xufeng Kou, Peng Zhang, Zhi-gang Chen, Alexei V. Fedorov, Jin Zou, Trevor M. Riedemann, Thomas A. Lograsso, Kang L. Wang, Gary Tuttle & Faxian Xiu, *Scientific Reports* **2** (2012) 726

[26] Jinsong Zhang, Cui-Zu Chang, Zuocheng Zhang, Jing Wen, Xiao Feng, Kang Li, Minhao Liu, Ke He, Lili Wang, Xi Chen, Qi-Kun Xue, Xucun Ma & Yayu Wang, *Nat. Comm.* **2** (2011) 574

[27] T. Arakane, T. Sato, S. Souma, K. Kosaka, K. Nakayama, M. Komatsu, T. Takahashi, Zhi Ren, Kouji Segawa & Yoichi Ando, *Nat. Comm.* **3** (2011) 636

[28] Yang Xu, Ireneusz Miotkowski, Chang Liu, Jifa Tian, Hyoungdo Nam, Nasser Alidoust, Jiuning Hu, Chih-Kang Shih, M. Zahid Hasan and Yong P. Chen, *Nat. Phys.* **10** (2014) 956

[29] Dimitrie Culcer, *Physica E* **44** (2012) 860

[30] Thomas Ihn, *Semiconductor Nanostructures: Quantum States and Electronic Transport* (Oxford University Press) 2010

[31] D. Schoenberg, *Magnetic Oscillations in metals* (Cambridge University Press, London) 1984

[32] Desalegne Teweldebrhan, Vivek Goyal and Alexander A. Balandin, *Nano Lett.* **10 (4)** (2010) 1209

[33] D. West, Y. Y. Sun, Han Wang, Junhyeok Bang, & S. B. Zhang, *Phys. Rev. B* **86** (2012) 121201

[34] L. Xue, P. Zhou, C. X. Zhang, C. Y. He, G. L. Hao, L. Z. Sun & J. X. Zhong, *AIP* Advances **3** (2013) 052105

[35] Y. S. Hor, A. Richardella, P. Roushan, Y. Xia, J. G. Checkelsky, A. Yazdani, M. Z. Hasan, N. P. Ong, and R. J. Cava, *Phys. Rev. B* **79** (2009) 195208

[36] J. G. Checkelsky, Y. S. Hor, M.-H. Liu, D.-X. Qu, R. J. Cava, and N. P. Ong, *Phys. Rev. Lett.* **103** (2009) 246601

[37] N. P. Butch, K. Kirshenbaum, P. Syers, A. B. Sushkov, G. S. Jenkins, H. D. Drew & J. Paglione, *Phys. Rev. B* **81** (2010) 241301(R)

[38] James G. Analytis, Jiun-Haw Chu, Yulin Chen, Felipe Corredor, Ross D. McDonald, Z. X. Shen & Ian R. Fisher, *Phys. Rev. B* **81** (2010) 205407

[39] Z. Ren, A.A. Taskin, S. Sasaki, K. Segawa & Y. Ando, *Phys. Rev. B* **82** (2010) 241306

[40] Z. Ren, A. A. Taskin, S. Sasaki, K. Segawa & Y. Ando, *Phys. Rev B* **84** (2011) 075316

[41] Z. Ren, A. A. Taskin, S. Sasaki, K. Segawa & Y. Ando, *Phys. Rev. B* **84** (2011) 165311

[42] A. A. Taskin, Z. Ren, S. Sasaki, K. Segawa & Y. Ando, *Phys. Rev. Lett.* **107** (2011) 016801

[43] Jun Xiong, A. C. Petersen, Dongxia Qu, Y. S. Hor, R. J. Cava & N. P. Ong, *Physica E* **44** (2012) 917

[44] Paul Syers, Johnpierre Paglione, arXiv:1412.1422

[45] Matthew Brahlek, Nikesh Koirala, Namrata Bansal & Seongshik Oh, *Solid State Communications* **215** (2015) 54

[46] Marco Bianchi, Dandan Guan, Shining Bao, Jianli Mi, Bo Brummerstedt Iversen, Philip D.C. King & Philip Hofmann, *Nat. Commun.***1** (2010) 128

CHAPTER 2

Experimental Techniques

2.1 Single Crystal Synthesis

The “modified Bridgman” method [1] has been used to synthesize single crystals of the 3D Topological Insulator systems Bi_2Se_3, Bi_2Te_3, $Bi_{2-x}Sb_xSe_3$ and $Bi_2Se_{3-x}Te_x$. In this technique the precursor elements viz. Bi, Sb, Se, Te in their high purity form (99.999%) were taken in the required stoichiometry, mixed together and vacuum sealed in a quartz crucible with a conical tip. The sealed crucible was held vertically in a box furnace and the samples were grown by melt process. The melting points of the elements and the compounds are known to be Bi = 271.5°C, Sb = 630.63°C, Se = 221°C, Te = 449.51°C, Bi_2Se_3 = 710°C, Bi_2Te_3 = 586°C. The stoichiometric mixture was first heated to 850°C in 24 hours and the melt was then held at the same temperature for 24 hours for homogenization. This step was followed by cooling the melt from 850°C to 550°C with different cooling rates (1°C/hour, 2°C/hour, 137°C/hour), and subsequently it was held at 550°C for 24 hours followed by furnace cooling to room temperature. The obtained boule was generally greyish in colour, had a cleavage plane along the 001 crystal axis leading to flat silvery crystals having typical dimensions of 0.6 cm x 0.6 cm (ref. Figure 2.1).

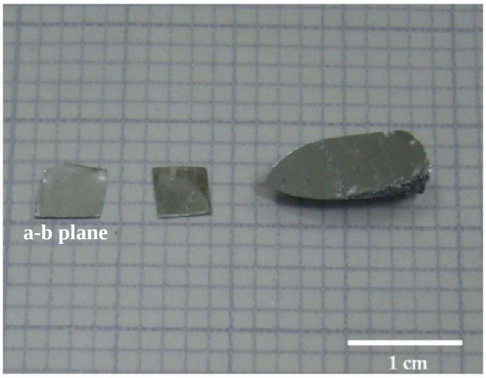

Figure 2.1 – Photograph of Bi_2Se_3 crystals of typical dimensions.

2.2 X-ray diffraction:

2.2.1 Powder Diffraction

Phase elucidation for the synthesized samples was done by room temperature powder X-ray diffraction (XRD) on powdered single crystals carried out at BL-12 beam-line of Indus II, RRCAT – Indore [2]. The experiment was carried out Debye-Scherrer geometry mode wherein X-rays of a defined energy were incident on the samples enclosed in a circular depression in kapton tape and the data was collected using a MAR 3450 image plate detector positioned behind the sample. The energy of the incident X-ray and the sample to detector distance were 12.6 keV and 120 mm respectively. The 2D image plate data was converted into a 1D 2θ vs. intensity format using FIT2D software [3]. The lattice parameters were extracted from the diffraction data using the refinement procedure in *PowderCell* [4]. Figure 2.2(a)-(b) show the typical MAR3450 image plate data and the corresponding 2θ vs. intensity plot of a Bi_2Se_3 sample respectively.

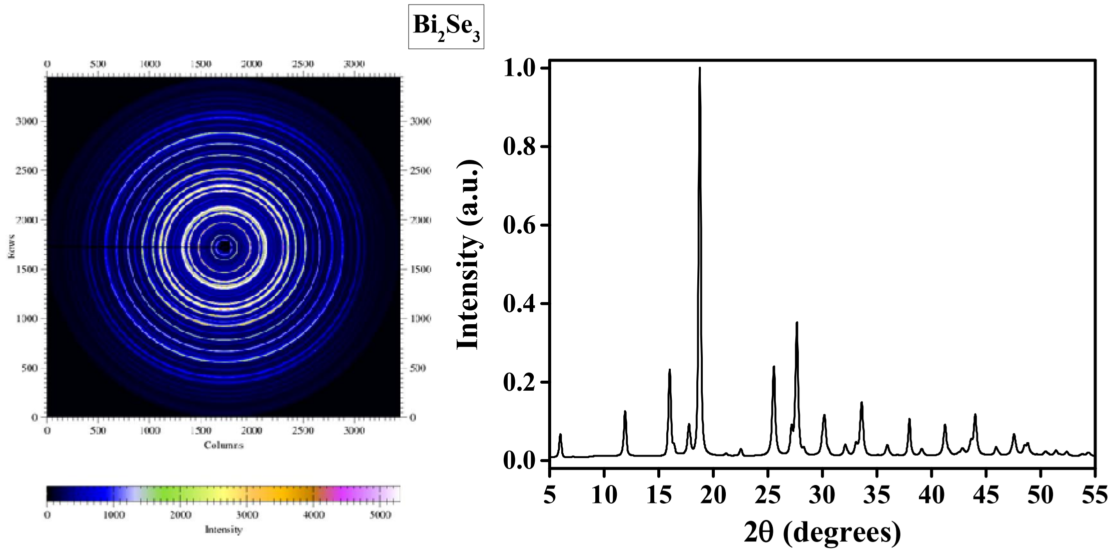

Figure 2.2 – (a) MAR3450 2D image plate data of powder diffraction from Bi_2Se_3; **(b)** 2θ vs. intensity data converted from image plate using the FIT2D program

2.2.2 Laue diffraction

The Laue diffraction measurements were carried out on cleaved single crystals using a Molybdenum X-ray source, and the patterns were recorded using a HD-CR-35 NDT image plate system, to determine their orientation. In this experiment, a beam of white X-ray radiation is allowed to fall on a fixed single crystal. Since the Bragg angle θ is fixed for every set of planes in the crystal, each set picks out and diffracts a particular wavelength which satisfies the Bragg law for the particular values of *d* and *θ* involved [5]. The Laue diffraction can be carried out in two different measurement geometries – the transmission geometry and back-reflection geometry based on the relative positions of the X-ray source, the sample and the photographic film. The schematics of both the geometries are shown in Figure 2.3(a)-(b). In both the geometries, the single crystal is placed perpendicular to the direction of X-rays.

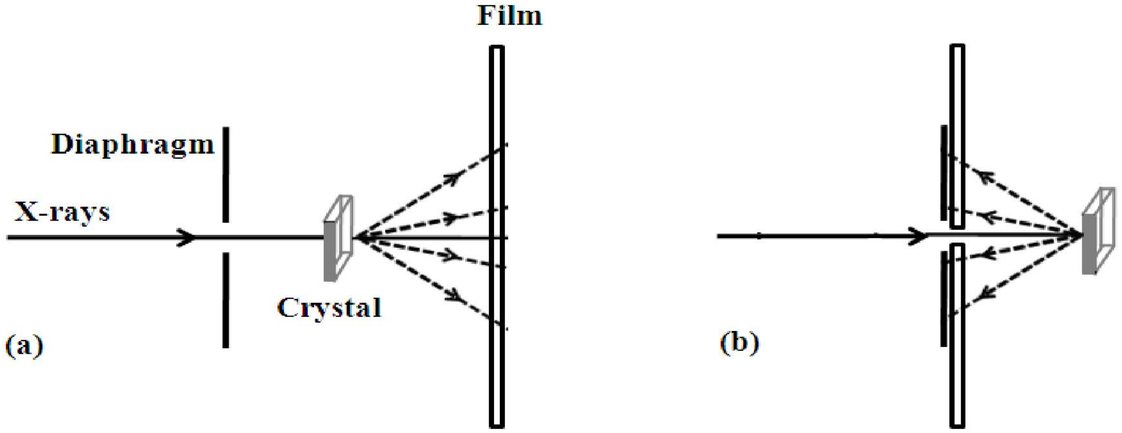

Figure 2.3 – Schematic of the Laue diffraction geometries – **(a)** Transmission geometry; **(b)** back-reflection geometry

In the transmission geometry (Figure 2.3(a)), the photographic film is placed after the sample which records the beams diffracted in the forward direction that gets partially transmitted through the crystal. In the back-reflection Laue method (Figure 2.3(b)), the film is placed between the X-ray source and the crystal and the beams diffracted in the backward direction are recorded. In both these geometries, the diffracted beams form an array of spots on the film. Figure 2.4(a)-(b) shows the Laue diffraction pattern from transmission and back-reflection geometries of a Bi_2Se_3 single crystal.

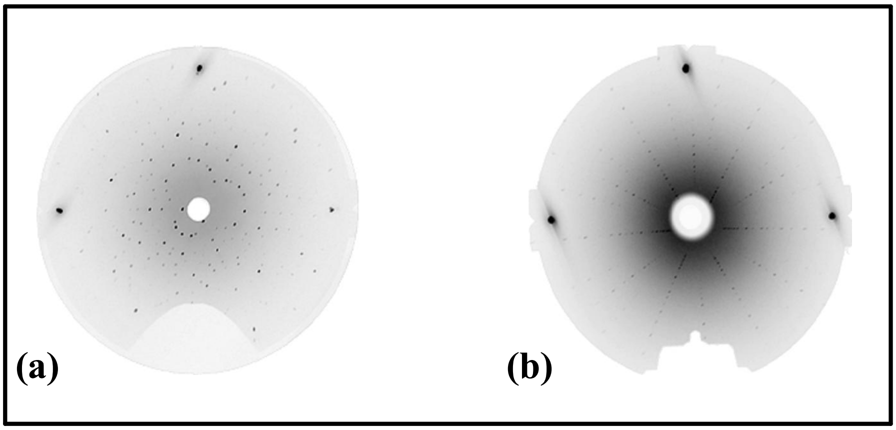

Figure 2.4 – Laue diffraction pattern on Bi_2Se_3 in **(a)** transmission geometry; **(b)** back-reflection geometry.

2.3 Electrical Resistivity

2.3.1 Ambient Pressure resistivity

The resistivity of the synthesized samples was measured by the Van der Pauw method. Figure 2.5(a)-(d) shows the schematic of the Van-der Pauw geometry used for resistivity measurements.

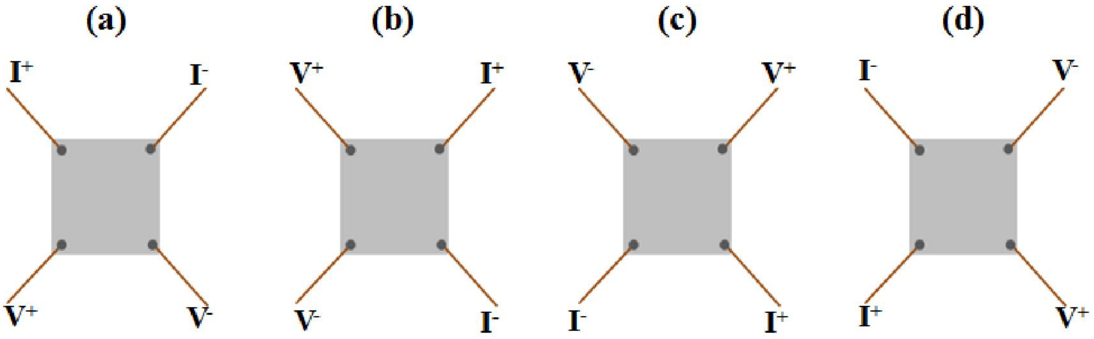

Figure 2.5 – (a)-(d) The four Van der Pauw configurations used for resistivity measurement represented schematically.

The resistivity ρ at a particular temperature is determined by iteratively solving the following equation [6]

$$e^{-\frac{\pi r_1}{\rho t}} + e^{-\frac{\pi r_2}{\rho t}} = 1 \tag{2.1}$$

Where r_1 and r_2 are resistance values from different Van der Pauw configurations (for example Figure 2.5(a)-(b)) and t is the thickness of the sample. Figure 2.6(a) shows the setup for the measurement of resistivity as a function of temperature.

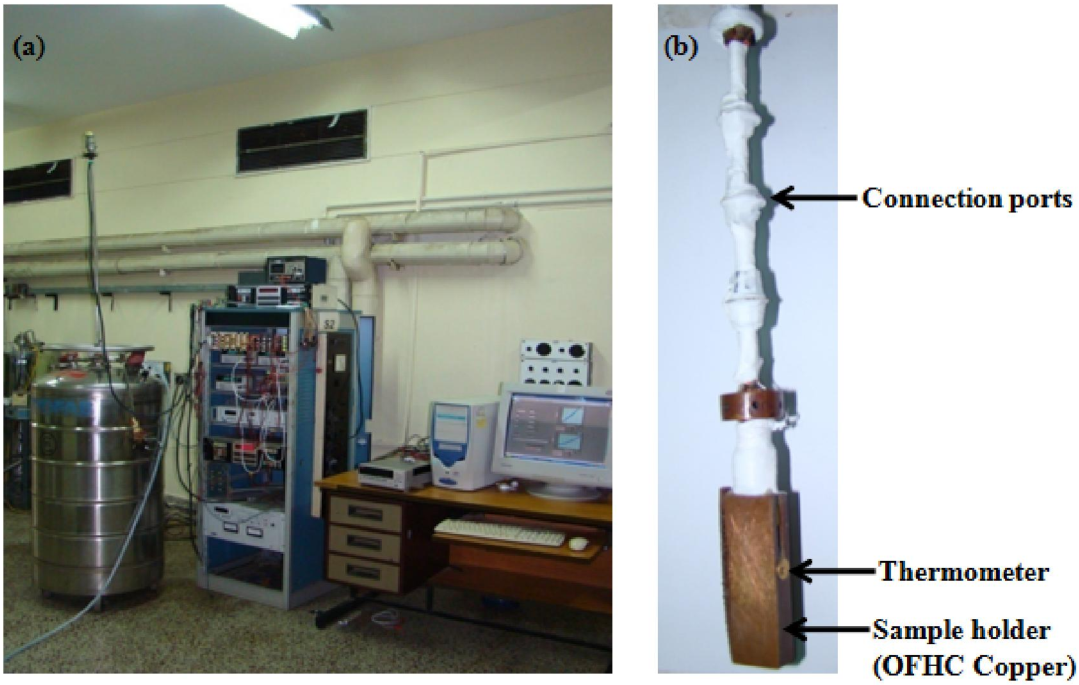

Figure 2.6 – (a) The set-up for measuring the resistance of a sample in the temperature range 300 K to 4.2 K; **(b)** The sample holder portion of the dipstick.

This setup consists of a dipstick, the helium dewar, current sources and nano-voltmeters. The sample is mounted on an OFHC (Oxygen Free High Conductivity) copper block (shown in (Figure 2.6(b))) using a double sided tape. 44 SWG copper wires, de-enamelled at the ends are used as leads and the contacts are made on the sample using silver paste that cures at room temperature. The other end of the leads are connected to the current source and nano-voltmeter through a connector mounted on the dipstick. A calibrated Si diode thermometer (shown in (Figure 2.6(b)) which is mounted on the OFHC copper block is used to record temperatures. The sample is mounted in close vicinity of the thermometer so as to avoid any thermal gradients in the holder. The temperature range of 300 K to 4.2 K is attained in a Dewar containing liquid helium where the liquid bath is at 4.2 K (boiling point of liquid Helium) and the neck of the Dewar is nearly at 300 K. The dipstick with the sample mounted is then attached to the neck of the Dewar using clamps and then slowly dipped inside. The resistance of the sample is measured by passing a steady direct current of few mA through it, measuring the voltage drop across the sample and converting it into resistance using the formula R = V/I. A direct current of 10μA is passed through the Si diode sensor and the resulting voltage drop across it is used for calculating temperature using pre-calibrated Chebyshev polynomial coefficients. The sample voltage and the Si diode voltage are measured simultaneously by triggering the respective nano-voltmeters at the same instant using a *LabView* program through GPIB interface with the computer. As the leads that connect the sample to the current-source and the nano-voltmeters experience a thermal gradient, the measured voltage across the sample includes an additional thermo-emf component. Thus for a current I^+, the measured voltage V^+ across the sample is given as

$$V^+ = V^+_{sample} + V_{thermo} \tag{2.2}$$

To negate the contribution of this thermo-emf, the direction of current through the sample is reversed i.e. I^- and the corresponding voltage drop V^- is measured. As the thermo-emf is independent of the direction of current, the voltage measured under current reversal is

$$V^- = V^-_{sample} + V_{thermo} \tag{2.3}$$

The two voltages are then subtracted and the modulus of the average is taken to get the actual voltage drop across the sample which gives its resistance as

$$R = {}^{V}\!/_{I} \tag{2.4}$$

Where $V = |V^{+} - V^{-}|$

The data is collected throughout the dipping process until the sample reaches the liquid Helium bath where the minimum temperature of 4.2 K is reached. The resistance as a function of temperature data is also collected during the warming process so as to check whether the *R* vs. *T* curve is retraced.

2.3.2 High Pressure resistivity

A home built miniature Bridgman opposed anvil high pressure cell attached to a dipstick arrangement is used for carrying out resistivity measurements at high pressures in the temperature range 300 K to 4.2 K [7]. The design is that of a clamp-type cell where the applied pressure on the sample is retained by employing a lock-nut. The maximum pressure attainable in this cell is ~ 8 GPa. Pyrophillite and steatite are used as the gasket and pressure transmitting medium respectively. The schematic of the high pressure cell is shown in Figure 2.7.

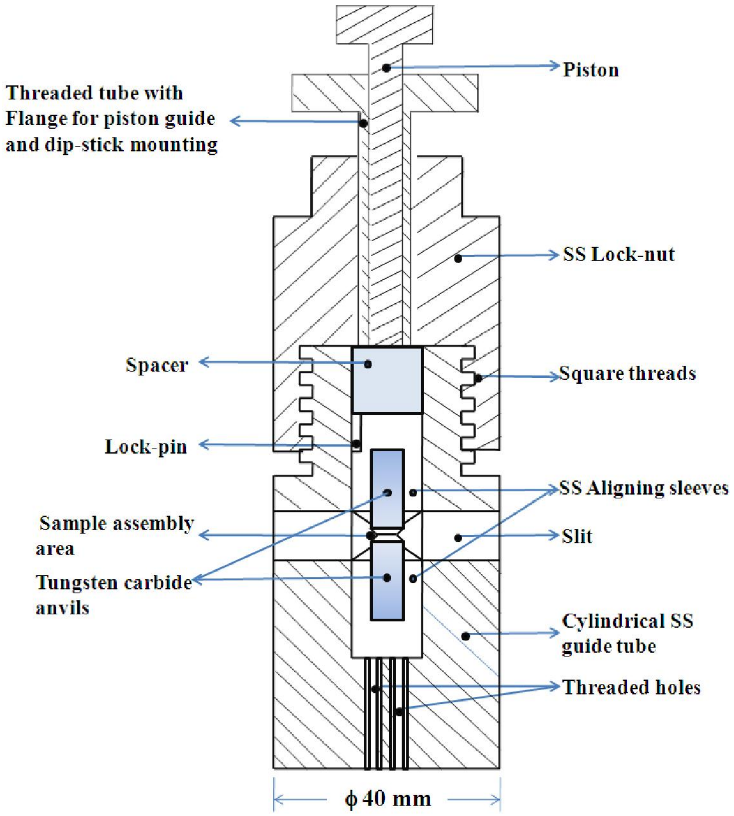

Figure 2.7 – Schematic diagram of the miniaturized high pressure cell used for resistivity investigations

The various components of the cell are

a) Guide tube – made of stainless steel (SS), 40mm diameter x 140 mm length x 9 mm wall thickness

b) Anvils – made of tungsten carbide, 12 mm diameter x 20 mm length, flat face of 4 mm diameter

c) Aligning sleeves – made of SS, 22 mm outer diameter x 36 mm length x 5 mm wall thickness. The sleeves have a tapering at angle of 30° at one end to reduce the diameter to 12 mm

d) Lock nut – made of SS, cylindrical, 2 mm diameter x 5 mm length

e) Piston – made of SS, 100 mm diameter

f) Thermometer – pre calibrated Si diode sensor

Slits of dimensions 5 mm width x 20 mm length are machined at diametrically opposite ends of the guide tube for taking the leads from the anvils to the exterior. Pyrophillite and Steatite are used as the gasket and pressure transmitting medium respectively.

The sample mounting procedure is described below –

1. On the 4 mm flat face of the tungsten carbide anvils, a pyrophillite washer of dimensions 1 mm inner diameter x 4 mm outer diameter x 0.16 mm thickness is mounted using slow setting araldite.
2. Grooves, 8 in number are made on the pyrophillite gasket using a sharp scalpel so as to hold the electrical leads in place. The grooves are made deep enough so as to allow the leads to sit safely inside but at the same time it is ensured that groove doesn't cut through the pyrophillite disc and damage its integrity.
3. The pressure transmitting medium steatite, in the form of discs of dimensions 1 mm diameter x 0.13 mm thickness is then placed inside the 1 mm hole in the pyrophillite washer.
4. Electrical leads, preferably made of 46 SWG manganin wire and of sufficient length are then placed inside the grooves, such that a part of them lies inside the sample space without touching each other. The wires are anchored in their grooves using araldite.
5. Another pyrophillite washer of similar specifications as the first is then mounted over the lower one using araldite.
6. The sample is the mounted in the 1 mm sample space provided by the two pyrophillite washers.
7. This is followed by closing the sample space by placing another steatite disc over the mounted sample and sealing it using araldite.

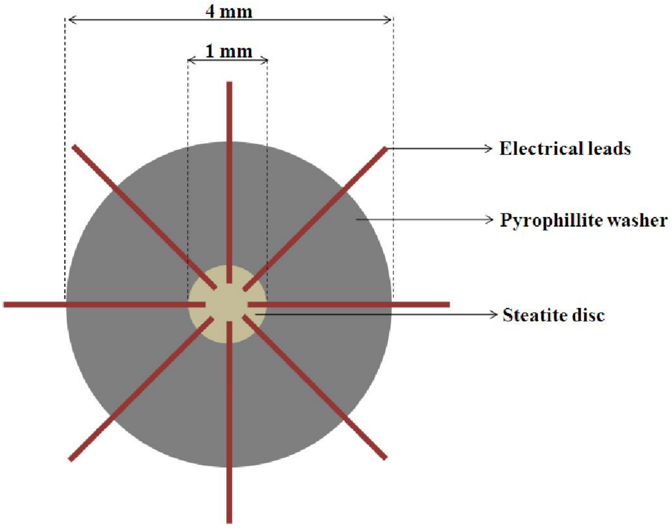

Figure 2.8 – Schematic of the face of the anvil with Pyrophillite washer, steatite disc and wires mounted on it.

During the mounting process, care is taken so that the araldite used for bonding at various places does not flow into the sample space. Following the mounting of the sample on the anvil, the same anvil is slowly inserted into the guide tube and the free ends of the leads are taken out of the guide tube through the slits. The other anvil is then slowly placed over the top of the bottom anvil such that their faces are in perfect alignment. The lock-nut notch provided on the top anvil and on the inner wall of the guide tube prevents the top anvil from rotating while locking the applied pressure. The pressure is applied at ambient temperature using a hydraulic press and is locked. The cell is then attached to a specifically designed dipstick arrangement. The leads from both the sample and the thermometer are connected to DC power supply and nano-voltmeters for passing current and measuring the voltage developed. The pressure cell is then wrapped around with several layers of aluminized Mylar for improving the temperature uniformity. The dipstick is then slowly inserted into the Helium Dewar and the resistance of the samples under study is measured as a function of temperature from 300 K to 4.2 K by exploiting the natural gradient present inside the Dewar. The procedure for data collection remains the same as mentioned in the preceding section.

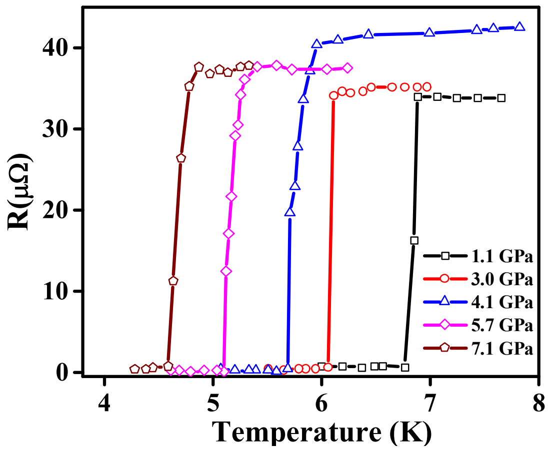

Figure 2.9 – The variation of superconducting transition temperature of Pb with application of pressure

The relation between the loads applied by the hydraulic press to the value of pressure locked in the cell is determined by measuring the shift in the superconducting transition in lead (Pb). This calibration is done prior to mounting the experimental sample. Figure 2.9 shows data collected on Pb under different pressures. Care is taken to perform the subsequent high pressure resistivity measurement on the sample under the same experimental conditions as that of the Pb calibration. The maximum error in the value of pressure reported is of the order of ~ 0.2 GPa.

2.4 Magneto-transport:

Magneto-transport measurements were carried out in a commercial cryogen free 15 T MR system from Cryogenics Ltd., UK. Figure 2.10 shows the complete set-up.

Figure 2.10 – Commercial 15T Cryogen free Magneto-resistance set-up from Cryogenic Ltd., UK for carrying out magneto-resistance and Hall measurements

The various components of the system are

i. Cryogen-free magnet system which includes –

a) Cryostat

b) Superconducting magnet – the magnet is a vertically oriented hybrid solenoid wound from copper stabilized filamentary superconducting wire of NbTi with Nb_3Sn.The magnet is energized via high temperature superconducting current leads. The temperature of the magnet is monitored with the help of temperature sensors mounted at various positions

c) Cryo-cooler – a two stage cryo-cooler, a Pulse tube refrigerator is used for cooling the whole system from the 300 K to base temperature. The first stage cools the radiation shield which surrounds the low temperature parts in the system and the second stage is used to cool the magnet and the variable temperature insert (VTI).

d) Variable temperature insert (VTI) – this helps in regulating the temperature of the sample from the 1.6 K to 325 K.

e) Electronic units – the main components are the Lakeshore temperature controller, Keithley 2700 multimeter, Magnet controls (Cryogenics Ltd.)

ii. Measurement probe – The probe platform (shown in Figure 2.11(a)) has two sample sockets for mounting the sample perpendicular and parallel to the magnetic field direction, a calibrated CERNOX sensor and a separate 100 Ω heater. A 19 pin connector is used to connect the platform to the probe.

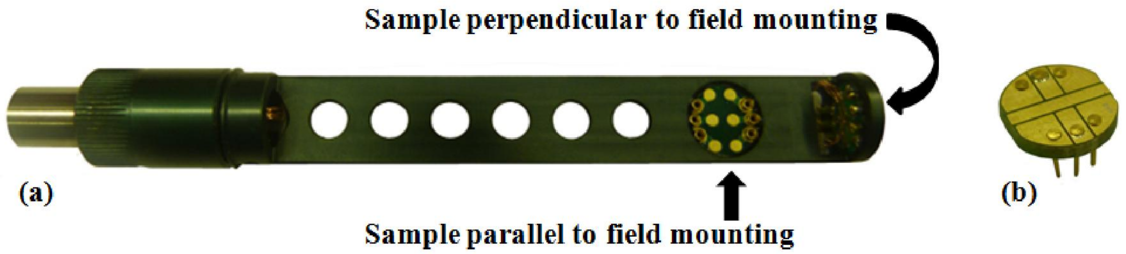

Figure 2.11 – **(a)** Measurement probe; **(b)** the sample puck

Samples are mounted on a sample puck (shown in Figure 2.11(b)). Samples of typical dimension 10 mm x 5 mm can be mounted on the puck. The sample wiring is made by soldering wires on to the gold pin contacts present. The Linear geometry (shown in Figure 2.12) was used for the magneto-transport measurements.

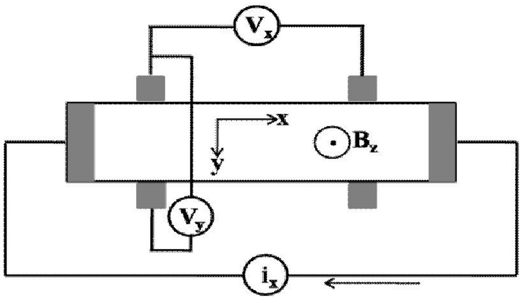

Figure 2.12 – Schematic representation of the linear geometry used for measuring magneto-resistance and Hall Effect on the synthesized samples.

Where i_x = current passed through the sample, V_x = longitudinal voltage, V_y = Hall voltage and B_z = External magnetic field.

From the boule grown, single crystals of uniform thickness have been cleaved and shaped into a rectangle. The length to width ratio is preferably maintained as 3:1. The sample was placed on the sample puck (shown in Figure 2.11(b)) provided by Cryogenics Ltd. using double sided tape. The contacts were made on the sample using a 25 micron thick gold wire and a conducting silver paste that cures at room temperature. Figure 2.13 shows a schematic diagram for the longitudinal and Hall resistance measurement in MR experiments.

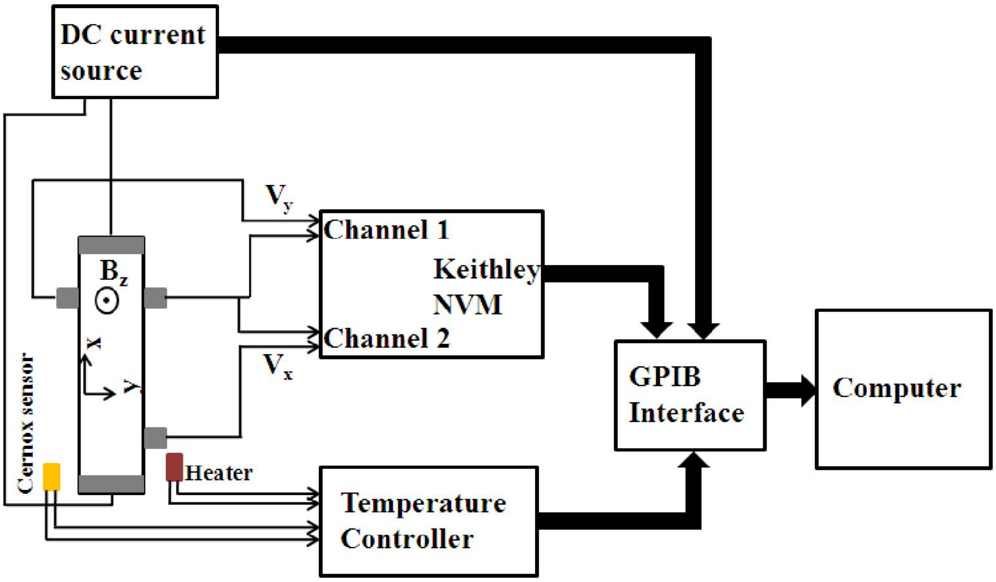

Figure 2.13 – Schematic diagram of the longitudinal resistance and Hall resistance measurement in MR experiments.

The electrical leads that are used for measuring the longitudinal voltage (V_x) and Hall voltage (V_y) are connected to the two channels of the Keithley Nano-voltmeter (NVM). A pre-calibrated Cernox sensor is used as a thermometer and is placed in proximity to the sample. A heater located near the sample space is connected to the Lakeshore temperature controller so as to monitor and control the temperature in the vicinity of the sample. The magnetic field B_z is applied via a NbTi-Nb_3Sn hybrid magnet which can provide magnetic fields in the range of -15 T to +15 T. The magnet is energized with the help of a magnet power supply. The longitudinal voltage and Hall voltage are measured simultaneously using a special switching unit. The data collection protocol involves: (a) stabilizing the sample at a specific temperature and (b) sweeping the magnetic field from -15 T to +15 T in small steps of 0.1 T. The data collection is automated using *LabView* program through a GPIB interface to the computer.

2.5 Positron Lifetime Spectroscopy

Positron annihilation lifetime spectroscopy is a non-destructive spectroscopy technique that allows studying a variety of phenomena and material properties on an atomic scale. The principle of this technique is based on the process of annihilation that occurs when a particle and its anti-particle meet. Positron (e^+) is the anti-particle of electron (e^-) with the same mass but with a positive charge as opposed to negative charge of the electron. The electromagnetic interaction between electrons and positrons makes possible annihilation of $e^+ - e^-$ pairs in which the total energy of the annihilating pair may be transferred to quanta of the electromagnetic field (photons). Principal channel of this reaction is the two-photon annihilation

$$e^+ + e^- \rightarrow \gamma_1 + \gamma_2 \tag{2.5}$$

When a positron is implanted into a solid, it undergoes a thermalisation process whereby it loses its energy to the matrix by scattering at ion sites, by electronic excitations and finally via phonon excitation. The thermalisation process happens within ~ tens of picoseconds. In the thermalised state, the positron undergoes a random walk through the ionic Bloch potential. In the absence of any defects, the positron wave function itself shows a Bloch like behaviour which is maximized around the interstitial position. In the presence of open volume defects like vacancies, the positron gets trapped in the attractive potential of the vacancy. This attractive potential is a result of the absence of the repulsive ion core and thus, the positron gets preferentially trapped at the vacancy trap site as shown in Figure 2.14(a) [8].

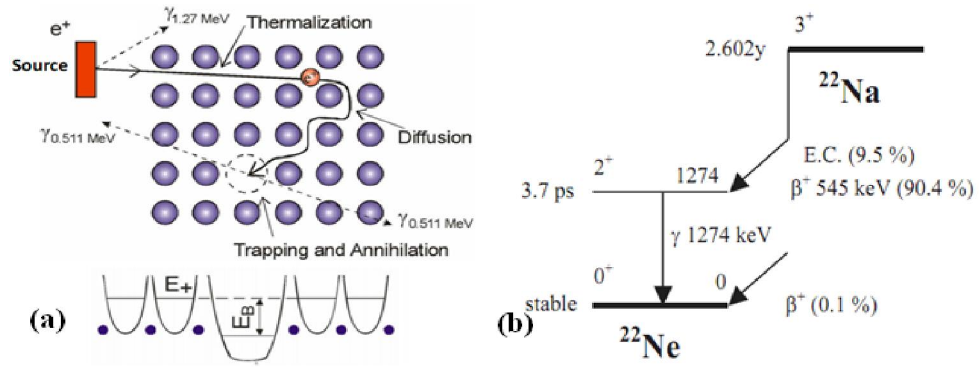

Figure 2.14 – **(a)** Schematic of the various processes which positron undergoes inside solid before its annihilation. The potential trap at a vacancy site is also shown schematically; **(b)** the decay scheme of the Na^{22} radioactive atom which is used as the positron source.

The annihilation process is also characterized with an annihilation rate λ (positron lifetime $\tau = \lambda^{-1}$), where λ is proportional to the effective electron density n_e sampled by positron. The annihilation rate of positrons (λ) which is inverse of the lifetime (τ) of positron inside the solid is directly proportional to the overlap of the positron $(n_+(r))$ and electron $(n_-(r))$ densities and is given by [8]

$$\lambda = \frac{1}{\tau} = \pi r_0^2 c \int n_+(r) n_-(r) \gamma dr \tag{2.6}$$

Where γ is the enhancement in electron density around positron due to Coulomb attraction, r_0 is the classical electron radius and c is the speed of light. When a vacancy is created by the removal of ion core, the net reduction in the local electron density is reflected as an increase in the lifetime of positron trapped at the site. The intensity of such a lifetime component gives the concentration of such trap sites.

The experimental lifetime spectrum can be understood in terms of simple rate equations, provided trapping of non-thermalised positrons is negligible and that the non interacting defects are homogeneously distributed in the sample. Under these conditions the time dependent positron diffusion equation for a sample with only one defect type can be written as [8]

$$\frac{dn_f(t)}{dt} = -\lambda_f n_f(t) - \kappa_1 n_f(t) \tag{2.7}$$

$$\frac{dn_d(t)}{dt} = -\lambda_d n_d(t) - \kappa_1 n_f(t) \tag{2.8}$$

Where

n_f is the fraction of positrons annihilating from the Bloch like delocalized state

$\lambda_f = 1/\tau_f$ is the annihilation rate in the defect free state

κ_1 is the trapping rate of the defect d

$\lambda_d = 1/\tau_d$ is the annihilation rate at the defect site

n_d is the fraction of positrons annihilating from defect d

The solution to the coupled differential equation is the decay spectrum which is expressed as

$$D(t) = I_1 e^{-t/\tau_1} + I_2 e^{-t/\tau_d} \tag{2.9}$$

Where

I_1 and I_2 are the intensities of the two annihilation sites such that $I_1 + I_2 = 1$

$\tau_1 = 1/(\lambda_f + \kappa_1)$ is the reduced bulk lifetime in the presence of the defect site.

The actual lifetime spectrum is the absolute value of the time derivative of the expression (4). Through the lifetime measurement, one tries to identify these lifetime components and thus get an idea of the defect species and their concentration in the sample.

For positron lifetime measurements, the Na^{22} positron source evaporated on a 1.25 micron Ni foil was sandwiched between two crystal surfaces. The measurements were carried out using a fast-fast coincidence spectrometer, having a time resolution of ~260 ps [9]. The positron data were analyzed using the LT program [10]. The mean lifetime is measured as the time delay between the birth of a positron, marked by the emission of the 1274 keV gamma photon due to the de-excitation of Ne (as shown in the decay scheme in Figure 2.14(b)) and its annihilation inside the solid, which is marked by the emission of two 511 keV gamma photons. Figure 2.15 shows a typical lifetime spectrum on a standard sample.

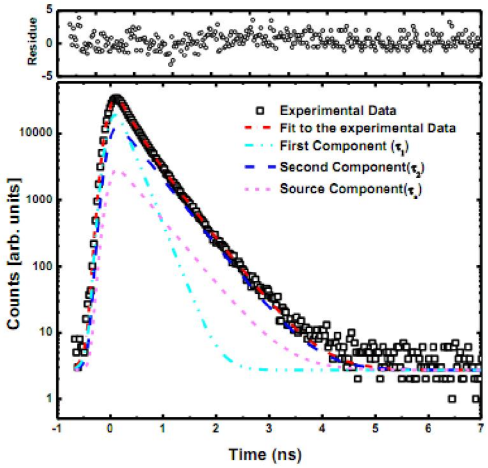

Figure 2.15 – A typical lifetime spectrum which shows the fit after subtracting the lifetime from the source. Two components have been resolved. The Gaussian like behaviour on the left side arises from the spectrometer resolution function with time resolution ~ 260 ps.

In general, in the presence of defects there are two components in the lifetime spectrum, corresponding to annihilations from bulk and the defects. The lifetime spectra analysed in terms of the convolution of the resolution function with the exponential decay functions. The annihilation rates from the bulk and defects are obtained from the nonlinear fit of the experimental data, to the above function. In general there is an annihilation that arises from the source foil, this component is obtained by carrying out an experiment on a standard sample, such as annealed iron (Fe). This is used in the fits to subtract out the source component (shown in Figure 2.15). In the present thesis most samples are characterized by positron annihilation lifetime measurements to throw light on the presence of Se vacancy in the systems investigated.

References

[1] Shuang Jia, Huiwen Ji, E. Climent-Pascual, M. K. Fuccillo, M. E. Charles, Jun Xiong, N. P. Ong, and R. J. Cava, *Phys. Rev. B* **84** (2011) 235206

[2] A. K. Sinha, Archna Sagdeo, Pooja Gupta, Ashok Kumar, M. N. Singh, R. K. Gupta, S. R. Kane and S. K. Deb, *AIP Conf. Proc.* **1349** (2011) 503

[3] A. P. Hammersley, S. O. Svensson, M. Hanfland, A. N. Fitch and D. Häusermann, *High Pressure Research* **14** (1996) 235

[4] W. Kraus and G. Nolze, *J. Appl. Cryst.* **29** (1996) 301

[5] B. D. Cullity, *Elements of X-Ray Diffraction* (Addison-Wesley Publishing Company, Inc., Massachusetts) 1956 p. 246

[6] L. J. vander Pauw, *Philips Res. Repts.* **13** (1958) 1

[7] Awadhesh Mani , A. Bharathi , V. S. Sastry , T. S. Radhakrishnan and Y. Hariharan, *ICEC18: Proc. 18th Int. Cryogenic Engineering Conf.* (2000) ed K G Narayankhedkar (New Delhi: Narosa Publishing House), p 615

[8] Krause-Rehberg R and Leipner H S *"Positron Annihilation in Semiconductors: Defect Studies" (Springer series in solid-state sciences)* **127** (1999) ed Manuel Cardona et al (Berlin: Springer)

[9] R. N. Viswanath, V. A. Chirayath, R. Rajaraman, G. Amarendra and C. S. Sundar, *Appl. Phys. Lett.,* **102** (2013) 253101

[10] J. Kansy, *Nucl. Instrum. Methods A*, **374** (1996) 235

CHAPTER 3

Quantum oscillations from Topological Surface States in Bi_2Se_3

It is clear from Chapter 1 that the Topological Insulators (TI) are small gap semiconductors, with band inversion occurring across the gap at TRIMs, rendering Topological Surface States (TSS) with Dirac cone dispersion [1][2][3][4]. To access these surface states, the Fermi surface needs to be in the TSS with virtually no states being occupied in the conduction band. In practise, this is seldom possible in Bi_2Se_3, as the system is prone to the host native thermodynamic defects such as Se and Bi vacancies (V_{Bi} & V_{Se}), Bi_{Se} & Se_{Bi} antisite defects [5][6]. As a consequence of their small gap, the presence of these defects renders the system to be highly n-doped and even for the lowest defect concentration realised in experiments the Fermi level gets pinned to the conduction band minima. The transport from the bulk carriers is in parallel to that of the metallic surface state and thus transport measurements would have a significant contribution from the bulk masking the signatures of TSS. Hence the initial studies were focussed on achieving lower charge carrier density and observing Shubnikov de Haas (SdH) oscillations from the TSS in these samples [7]. The earliest report on observation of SdH oscillation in Bi_2Se_3 was by G. R. Hyde et al. [8], who studied the angle dependence of the Magneto-resistance (MR) by carrying out the measurement in various configurations viz. sample plane perpendicular, parallel and at an acute angle to the external magnetic field direction, with SdH oscillations being observed in all the configurations. The fact that oscillations were observed by G. R. Hyde et al. even from $\theta = 90^\circ$ implies that the SdH oscillations arose from the quantized 3D bulk Fermi surface. To avoid transport from 3D Fermi surface individual reports by Analytis et al. [9] and Butch et al. [10] reported successfully synthesized samples with lower carrier densities of the order ~

10^{16} cm^{-3}; however oscillations from the TSS were observed only in the crystals grown by Analytis et al. SdH oscillations from the Quantized 3D bulk Fermi surface were observed in studies carried out by Eto et al. (carrier density 10^{18} cm^{-3}) [11] and Petrushevsky et al. (carrier density 10^{17} cm^{-3}) [12], as oscillations were seen in experiments with applied magnetic field parallel and perpendicular to the sample surface. In contrast, samples with carrier density 10^{19} cm^{-3} grown by M. Petrushevsky et al. exhibited characteristic oscillations from the TSS. Thus it is apparent that carrier density tuning alone is not sufficient to ensure that transport occurs from bulk or surface electronic states. M. Brahlek et al. [13] hypothesized that the carrier density and their dimensional nature depends crucially on the Fermi energy levels of the bulk and the surface states which are in turn governed by the concentration of defects in the surface and bulk respectively. When the Fermi level in the bulk is higher than that of the surface; there is charge depletion from the surface state and 2D SdH oscillations from the TSS will be observed. In the reverse scenario there is downward band bending and the bulk predominates in transport. It is therefore of interest to understand clearly, the role played by defects in observing SdH oscillations from TSS in magneto-transport measurements in single crystals.

Towards realising this objective, studies were undertaken along the following directions

i. Synthesizing Bi_2Se_3 crystal with different Se/Bi ratio; simulating Se and Bi atmosphere synthesis
ii. Synthesizing Bi_2Se_3 crystals by varying the rate of cooling from the melt.

The crystals were then characterized for structure, defects and transport, and the results obtained are discussed.

3.1 Synthesizing Bi_2Se_3 crystal with different Se/Bi ratio

3.1.1 Synthesis and X-Ray diffraction

Single crystals of Bi_2Se_3 were synthesized with varying Se/Bi ratio so as to simulate the following conditions:

a) Bismuth rich $Bi_{2.1}Se_3$ with Se/Bi ratio of 1.428

b) Stoichiometric Bi_2Se_3 with Se/Bi ratio of 1.5

c) Selenium rich $Bi_2Se_{3.1}$ and $Bi_2Se_{3.2}$ with Se/Bi ratio of 1.55 and 1.6 respectively.

For the crystal growth, the elements Bi and Se, taken in their high pure form, were melted at 850ºC in an evacuated quartz tube. The melt was then slow cooled at the rate of 1ºC/hour until 550ºC, kept at 550ºC for 24 hours followed by rapid cooling. These crystals could be easily cleaved along the basal plane yielding a silvery shiny mirror like surface. The cleaved crystals were powdered for characterization of their phase formation and crystalline purity using room temperature powder X-Ray diffraction at BL-12 beam-line of INDUS-II synchrotron, RRCAT – Indore. Figure 3.1 shows the powder diffraction pattern for the various compositions. All the major peaks could be indexed to those of the Rhombohedral Bi_2Se_3 structure. No Se or Bi impurity peaks were observed in the patterns confirming the phase purity of the prepared samples. The lattice parameters a and c were obtained by analyzing the powder diffraction data using the refinement routine in *PowderCell* [14]. Figure 3.2 shows the lattice parameter values as a function of Se/Bi ratio. It is observed that both a and c lattice parameters increase with increase in Se/Bi ratio from 1.428 to 1.55. For the sample with the highest Se/Bi ratio i.e. $Bi_2Se_{3.2}$, a and c are observed to decrease to values closer to the value for stoichiometric Bi_2Se_3.

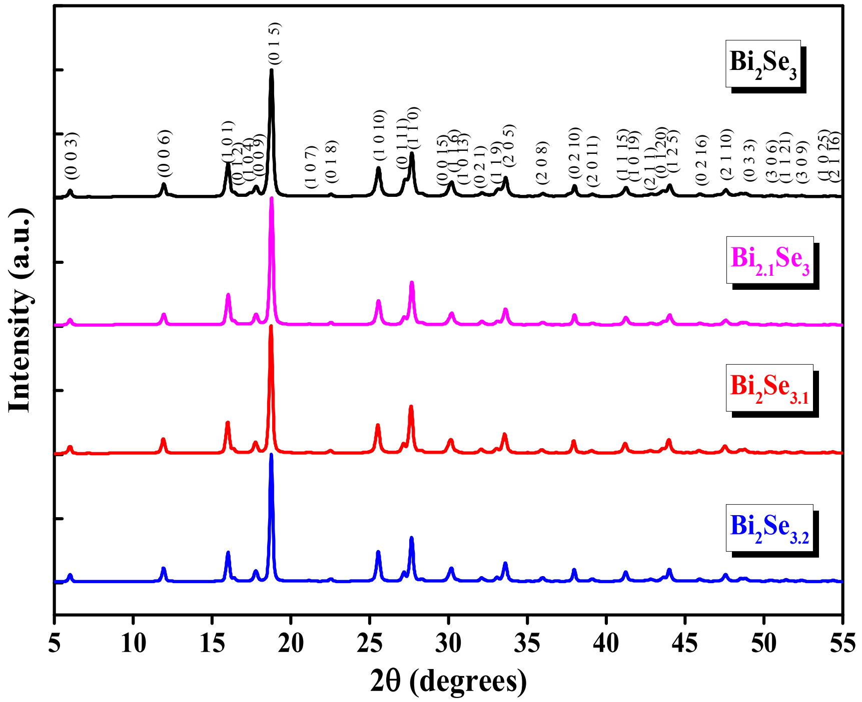

Figure 3.1 – Powder diffraction pattern of Bi_2Se_3 samples with different Se/Bi ratios. The peaks have been normalised to the highest observed peak intensity and have been shifted vertically for clarity.

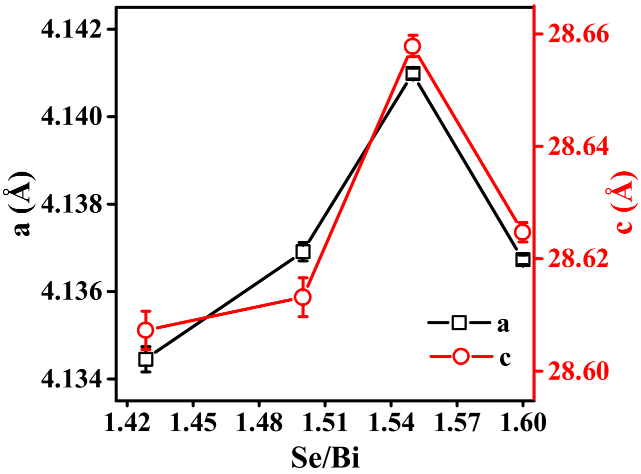

Figure 3.2 – Variation of *a* and *c* lattice parameters as a function of Se/Bi ratio.

Laue diffraction measurements in transmission and back reflection geometry were undertaken on the cleaved crystals using a Molybdenum X-ray source, and the patterns were recorded in both, transmission geometry and back-reflection geometry using a HD-CR-35 NDT image plate system. Figure 3.3 shows the Laue pattern collected in both transmission and back-reflection geometry. From the back-reflection pattern it is deduced that the cleavage plane of the crystal is (001). It is observed that while the spots are sharp in the Bi_2Se_3 sample, predominant radial streaking is observed in the non-stoichiometric samples $Bi_2Se_{3.1}$ and $Bi_2Se_{3.2}$, pointing to the presence of lattice deformations. These lattice deformations could manifest due to stacking faults along the c-axis and strain inhomogeneities [15][16][17]. In addition, some spots in the Laue pattern of $Bi_2Se_{3.1}$ show streaking in directions along the Debye arc, indicative of the presence of small angle tilt grain boundaries in the sample. The absence of back-reflection Laue pattern in $Bi_2Se_{3.1}$ sample indicates the presence of very strong stacking disorder, as can be observed from the large *c* lattice parameter value of 28.657 Å. The Laue pattern of the Bi rich sample $Bi_{2.1}Se_3$ has larger spots probably due to uniform strain due to presence of excess Bi.

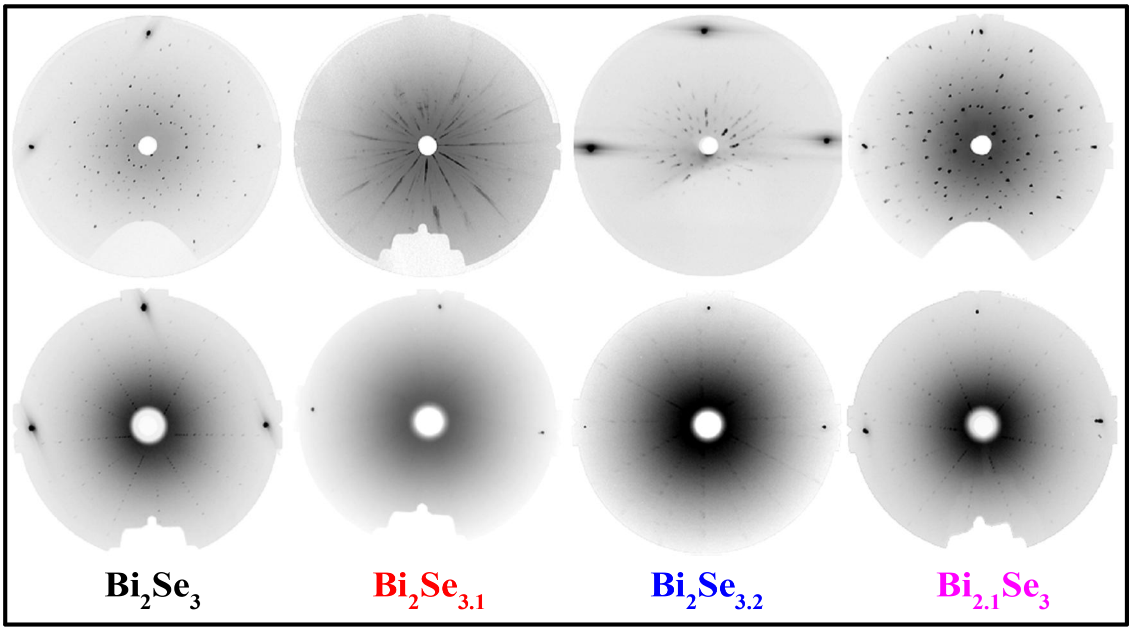

Figure 3.3 – Laue diffraction pattern of the crystals in transmission (above) and back-reflection (below) geometries. The sharp spots observed in the Laue pattern of stoichiometric Bi_2Se_3 indicate high crystallinity of the same.

3.1.2 Resistivity

Figure 3.4(a) shows the resistivity versus temperature data measured in the Van der Pauw geometry. The positive temperature co-efficient of resistivity indicates metallic behaviour in all samples, with a tendency of the resistivity to saturate below 30 K. In the samples with excess Se viz. $Bi_2Se_{3.1}$ and $Bi_2Se_{3.2}$, an increase in resistivity below 30 K was observed. The ρ/ρ_{50K} vs. temperature plots for $Bi_2Se_{3.1}$ and $Bi_2Se_{3.2}$, which depict the resistivity upturn at low temperatures are shown in Figure 3.4(b). The results obtained are similar to the one obtained by J. G. Analytis et al. [9]. Such an upturn suggests a significant contribution to the conductivity from the thermally activated carriers from an impurity band apart from that from the conduction bands.

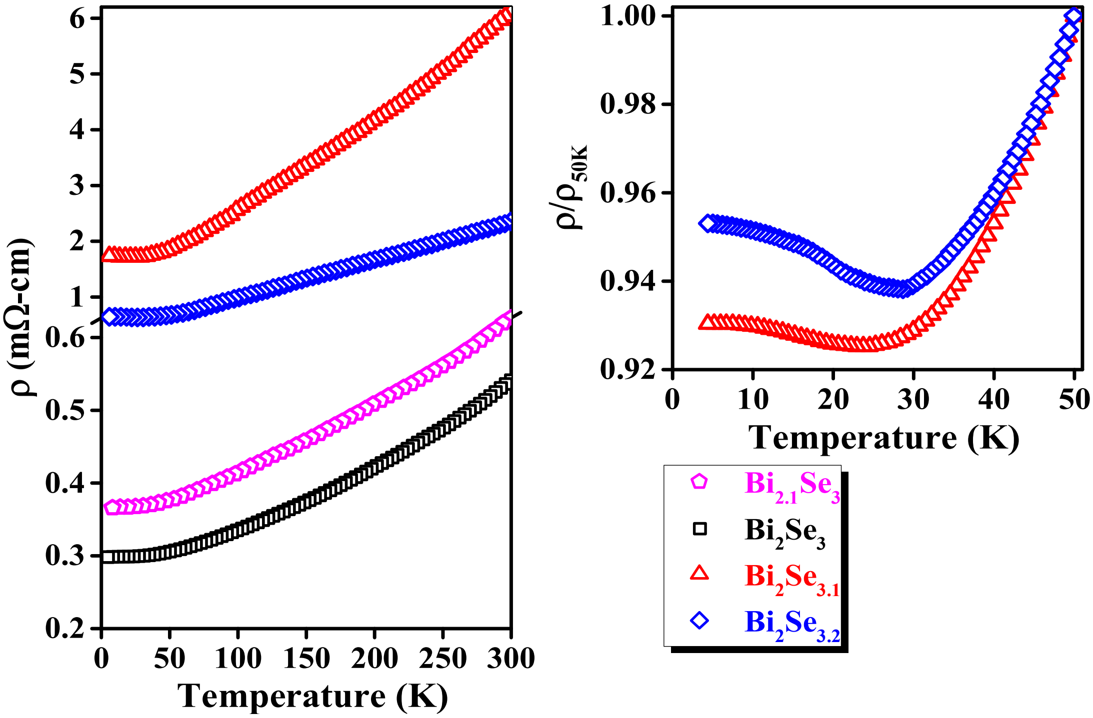

Figure 3.4 – (a) Resistivity vs. temperature behaviour of the synthesized samples marked in separate legend; **(b)** The upturn in resistivity at low temperatures (below 30 K) in the Se rich samples $Bi_2Se_{3.1}$ and $Bi_2Se_{3.2}$ is shown in normalized form.

3.1.3 Hall Effect measurements

To get an idea of the nature of charge carriers, Hall measurements were carried out at 4.2 K, (shown in Figure 3.5(a)). From the negative slope of the Hall data it is inferred that the carriers are electrons. The charge carrier density for the samples is estimated from the slope of the Hall data at low fields. Figure 3.5(b) shows the variation of charge carrier density with respect to Se/Bi ratio. The values of the charge carrier concentration initially increases with increase in Se/Bi ratio from 1.428 ($Bi_{2.1}Se_3$) to 1.55 (Bi_2Se_3) beyond which there is a significant reduction in the number of charge carriers for higher Se/Bi ratio. A possible reason for the reduction in charge carrier density with increasing Se Se/Bi ratio could be the reduction in the number of Se vacancies that contribute to the carriers in the system, which get compensated by the excess Se added during synthesis.

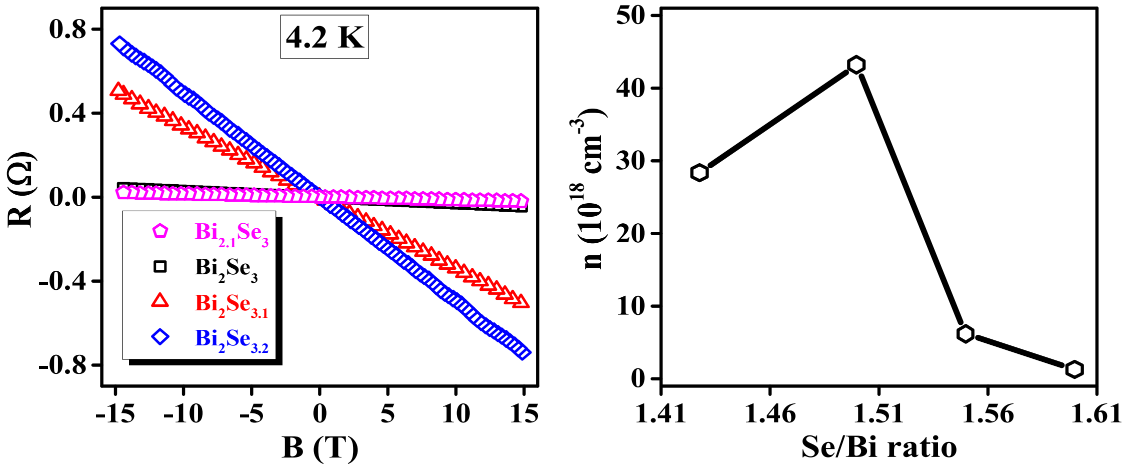

Figure 3.5 – **(a)** Hall data on the synthesized samples with different Se/Bi ratio; **(b)** estimated charge carrier density vs. Se/Bi ratio. The charge carrier density is observed to decrease with increase in Se/Bi ratio.

3.1.4 Magneto-resistance (MR)

The results of magneto-resistance ($R_{xx}(B)$ - $R_{xx}(0)$) measurements, carried out on (001) oriented single crystals in the magnetic field range of -15 T to 15 T at 4.2 K are shown in Figure 3.6. The resistivity contacts were made in the linear geometry as shown in Figure

2.11. R_{xx} is the longitudinal resistance at all fields and $R_{xx}(0)$ is the value of resistance at 0 T. As described in Section 1.8.1, the MR measurement was carried out in two different configurations with respect to the (001) sample plane viz., field out-of-plane ($H \| C_3$), where C_3 for Bi_2Se_3 is the *c*-axis and field in-plane ($H \| C_1$-C_2), where C_1-C_2 plane corresponds to the *a*-*b* plane of Bi_2Se_3. It is observed that the quantum oscillations i.e. Shubnikov de Haas oscillations are absent in the stoichiometric Bi_2Se_3 and present in the samples with higher Se/Bi ratio and lower charge carrier density (cf. Figure 3.5(b)). The frequency of the oscillations is determined by the Fourier transform on R_{xx} vs. 1/B data (shown on the right panel of corresponding MR data in Figure 3.6). It is noticed that the oscillations are dominated by a single frequency only in samples with an excess Se content viz., $Bi_2Se_{3.1}$ and $Bi_2Se_{3.2}$. The frequency of oscillations for $Bi_2Se_{3.1}$ and $Bi_2Se_{3.2}$ in the $H \| c$ direction, are 47.91 T and 36.78 T respectively. In the $H \| ab$ direction, the frequency of oscillations for $Bi_2Se_{3.1}$ and $Bi_2Se_{3.2}$ are 70.62 T and 58.92 T respectively. In the Bi rich sample $Bi_{2.1}Se_3$, multiple frequencies are observed in the oscillations.

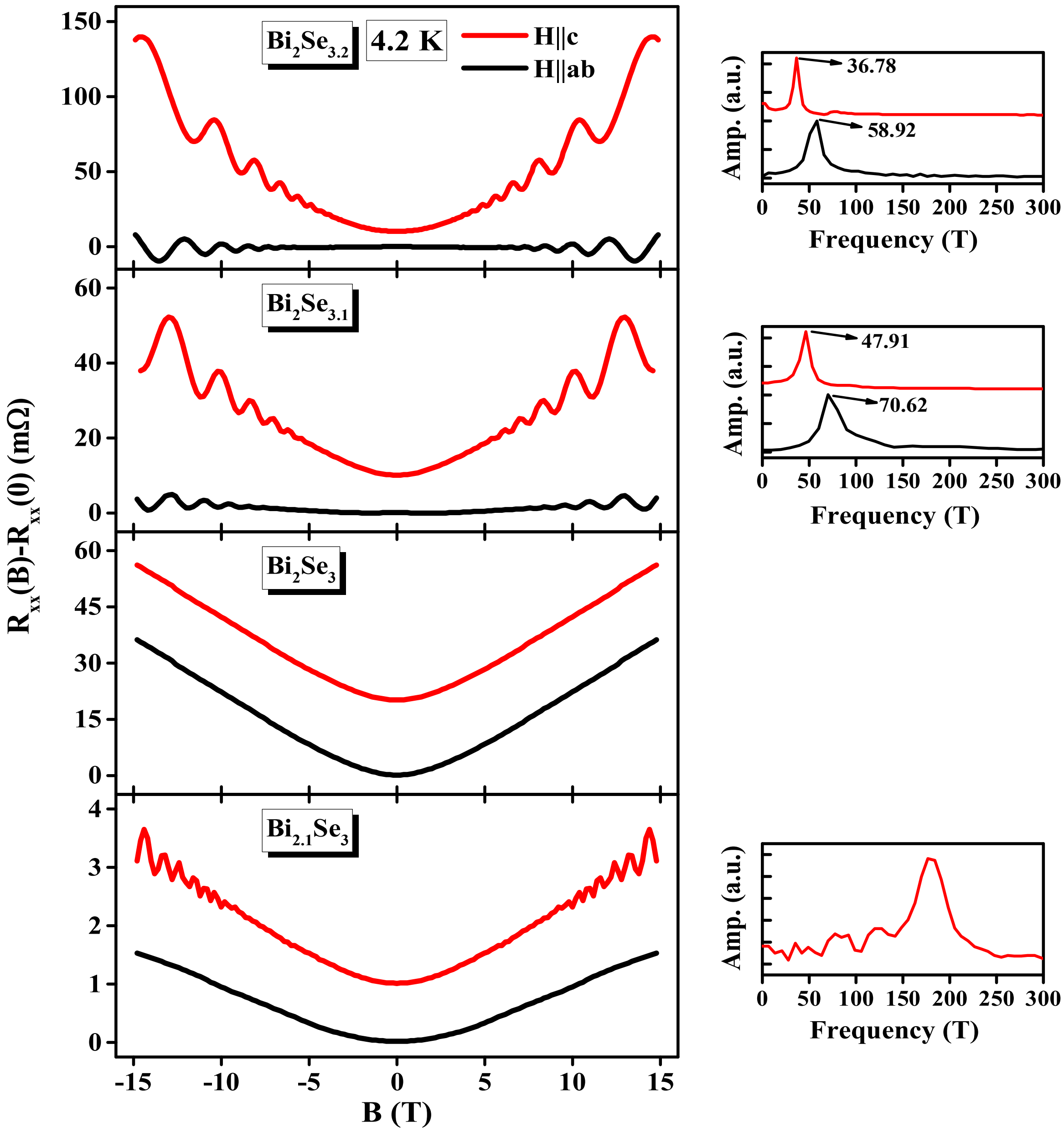

Figure 3.6 – Magneto-resistance data on the single crystals of Bi_2Se_3 with varying Se/Bi ratio in H‖c and H‖ab configurations. The data from the two configurations are offset for clarity. SdH oscillations are observed only in samples with higher Se/Bi ratio and lower charge carrier density. On the right side of each panel are the corresponding FFT plots indicating the frequency of oscillations. It is seen that the oscillations in $Bi_{2.1}Se_3$ do not have a single frequency.

Further analysis of the SdH oscillations is carried out using the Lifshitz-Kosevich (L-K) equation (described in Section 1.8.1). The L-K equation is given as [18]

$$\Delta R_{xx} = A_0 R_T R_D R_S \cos\left[2\pi\left(\frac{F}{B}+\frac{1}{2}-\beta\right)\right] \tag{3.1}$$

Figure 3.7 shows the L-K equation fits to the oscillations in $Bi_2Se_{3.1}$ and $Bi_2Se_{3.2}$ in both the H‖c and H‖ab configurations. The fitting parameters k_f, T_D, m_0, β, g and the physical quantities derived from them are tabulated in Table 3.1.

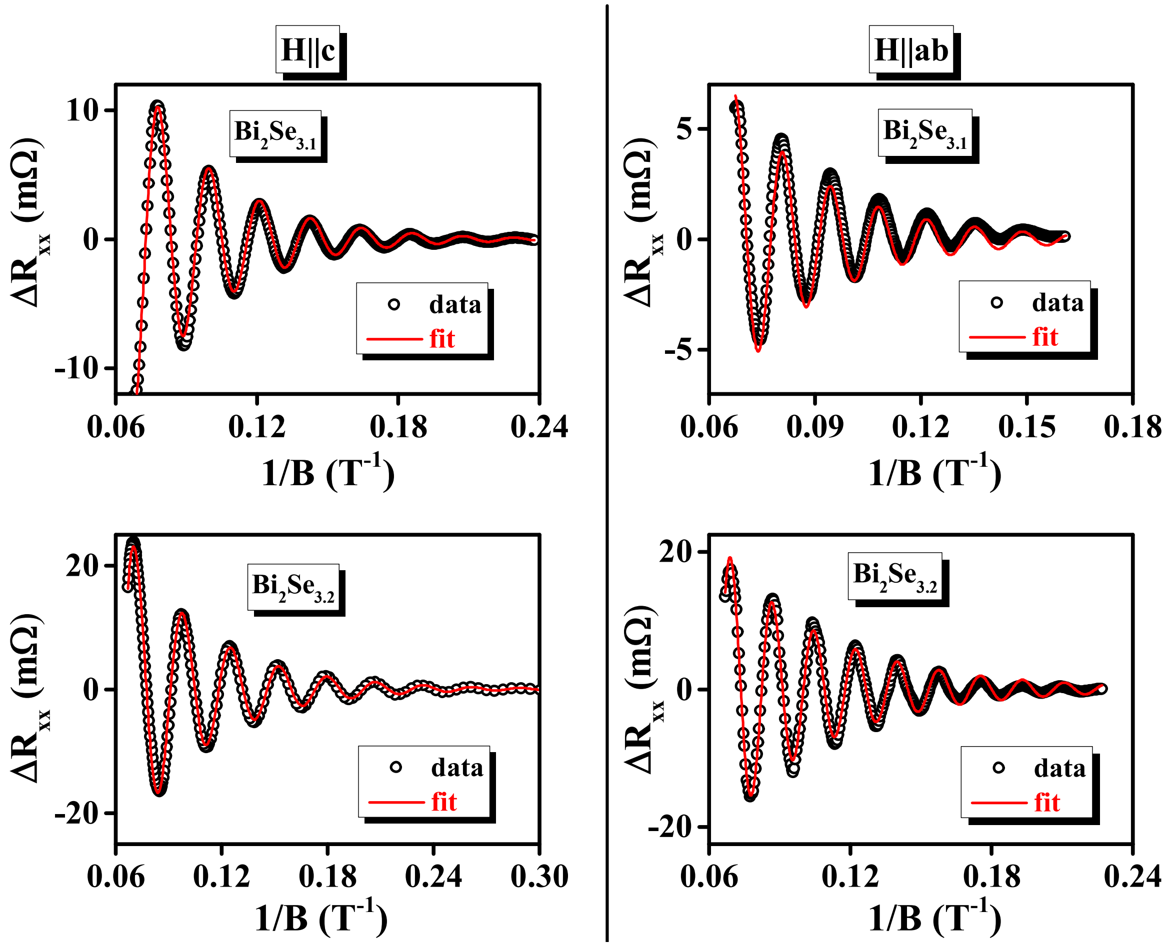

Figure 3.7 – L-K equation fit to the SdH oscillations in $Bi_2Se_{3.1}$ and $Bi_2Se_{3.2}$ in **(Left)** H‖c configuration and **(Right)** H‖ab configuration

Table 3.1 The fitting parameters and the derived physical quantities from the L-K equation fit to the oscillations in $Bi_2Se_{3.1}$ and $Bi_2Se_{3.2}$ in H‖c and H‖ab configuration

Fitting Parameters	**$Bi_2Se_{3.1}$**		**$Bi_2Se_{3.2}$**	
Applied Magnetic Field Direction	**H‖c**	**H‖ab**	**H‖c**	**H‖ab**
Fermi wave-vector k_F (10^6 cm^{-1})	3.7495	4.7221	3.3321	4.1371
Dingle Temperature T_D (K)	7.32	17.06	6.49	16.36
Cyclotron mass m^* (m_0)	0.181	0.116	0.152	0.068
quantum scattering time $[\tau_q = \hbar/(2\pi k_B T_D)]$ (fs)	166	71	187	74
Fermi velocity $[v_F = (\hbar k_F)/m^*]$ (10^5 ms^{-1})	2.42	4.71	2.52	7.03
2D carrier density $[n_s = (k_F^2)/4\pi]$ (*10^{12} cm^{-2})	1.12	1.77	0.88	1.36
Surface mean free path $[l_s^{SdH} = v_F \tau_q]$ (nm)	40.17	33.44	47.12	52.02
surface mobility $[\mu_s^{SdH} = (e l_s^{SdH})/(\hbar k_F)]$(cm^2/V.s)	1619	1075	2146	1908
β	0.62	-0.05	0.60	-0.08
g	2	2	2	2

The values of Berry phase obtained from the L-K equation fits to $Bi_2Se_{3.1}$ and $Bi_2Se_{3.2}$ in the H‖c configuration are 0.62 and 0.6 respectively, close to the value of 0.5 that should be obtained when transport occurs via TSS and the value of Berry phase obtained from SdH fit for H‖ab configuration is nearly zero; a value expected when transport is due to fermions with a parabolic dispersion.

As discussed in Section 1.8.1(a), the positions of minima and maxima in oscillations have a $(B_\perp \cos\theta)^{-1}$ dependence and hence oscillations from a 2D Fermi surface should be absent for $\theta = 90°$. Thus the occurrence of oscillations in the H‖ab configuration implies that there is a 3D Fermi surface which in the present case is the ellipsoidal bulk Fermi surface of Bi_2Se_3, as reported by Eto et al [11]. Therefore it can be surmised that the oscillations in H‖c configuration, has contributions from both 2D and 3D Fermi surface with the contribution from the bulk being predominant.

3.2 Synthesizing Bi_2Se_3 crystals by varying the rate of cooling from the melt

3.2.1 Synthesis and X-ray diffraction

Single crystals of Bi_2Se_3 were synthesized in the route as described in Section 3.1.1, with an exception to the cooling stage where the rate of cooling from melt at 850°C was varied as 1°C/hour, 2°C/hour and 137°C/hour. The purpose of growing the crystals at a faster cooling rate was to introduce strain disorder in the system. The single crystals grown from the above conditions would be referred to as BS1, BS2 and BS137 corresponding to the rate of cooling from the melt which are 1°C/hour, 2°C/hour and 137°C/hour respectively. Powder diffraction experiments were carried out on powdered single crystals (shown in Figure 3.8). No visible impurity phases of Se or Bi are observed. Figure 3.9 shows the variation of *a* and *c* lattice constants obtained from analysis of the powder diffraction pattern using *PowderCell* [14]. The lattice parameters of BS2 are lower than the values for the BS1, however both *a* and *c* lattice parameters of the fast cooled sample (BS137) are found to be very large compared to the slow cooled ones (BS1 and BS2). Such a significant increase suggests the presence of a uniform strain in the lattice.

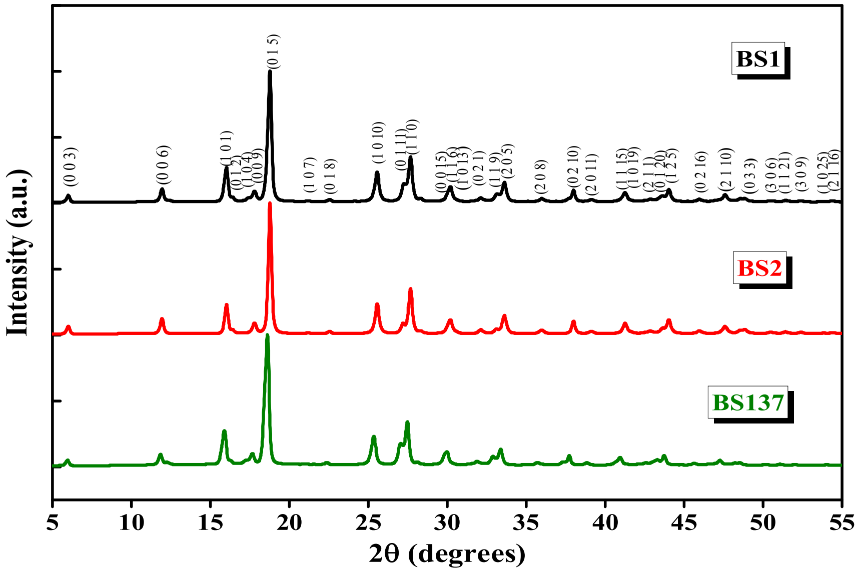

Figure 3.8 – Powder diffraction data of samples BS1, BS2 and BS137 measured on powdered single crystals. The peaks have been normalised to the highest observed peak intensity and have been shifted vertically for clarity.

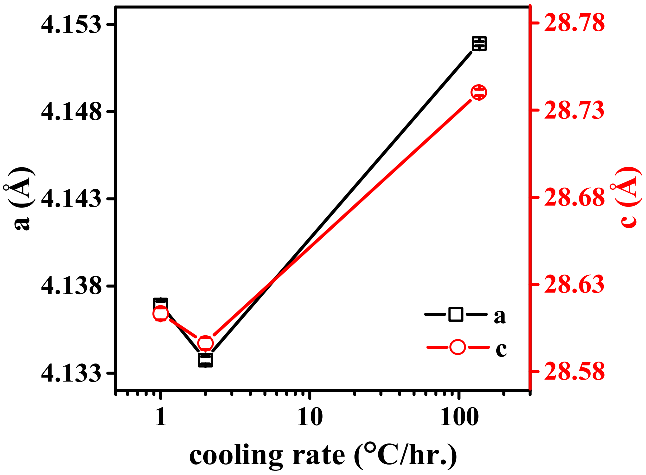

Figure 3.9 – Variation of *a* and *c* lattice parameters as a function of cooling rate from melt.

Figure 3.10 shows the Laue diffraction pattern for the three crystals BS1, BS2 and BS137. The Laue pattern of BS2 is found to be very similar to the pattern observed for $Bi_2Se_{3.1}$ (cf. Figure 3.3), both exhibit radial streaking. The Laue spots of BS137 are found to be enlarged in comparison to the sharp Laue spots observed in BS1.

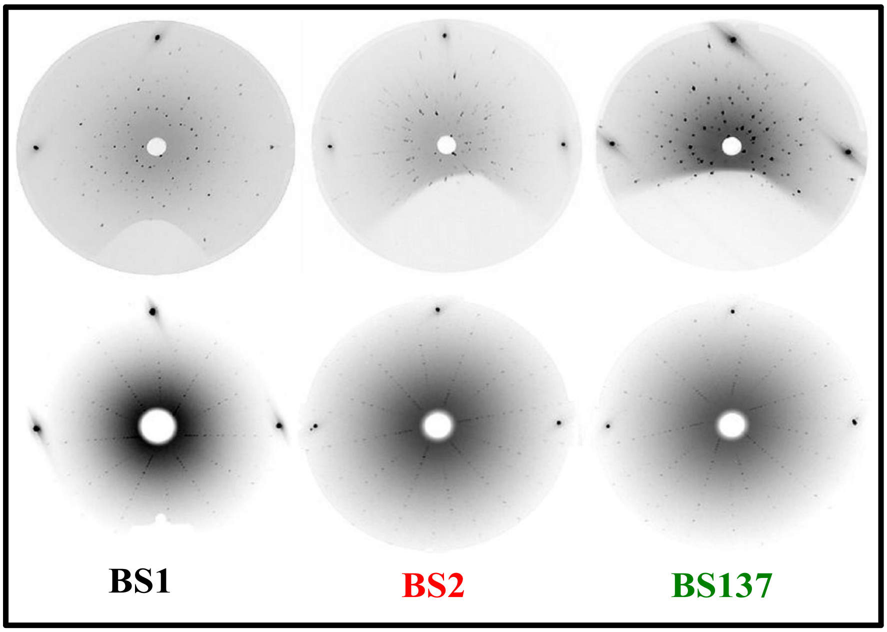

Figure 3.10 – Laue diffraction pattern for the Bi_2Se_3 single crystals grown from melt at different cooling rates in transmission (above) and back-reflection (below) geometries.

3.2.2 Resistivity

The resistivity vs. temperature data for BS1, BS2 and BS137 samples are shown in Figure 3.11. The resistivity is seen to decrease monotonously with increase in cooling rate.

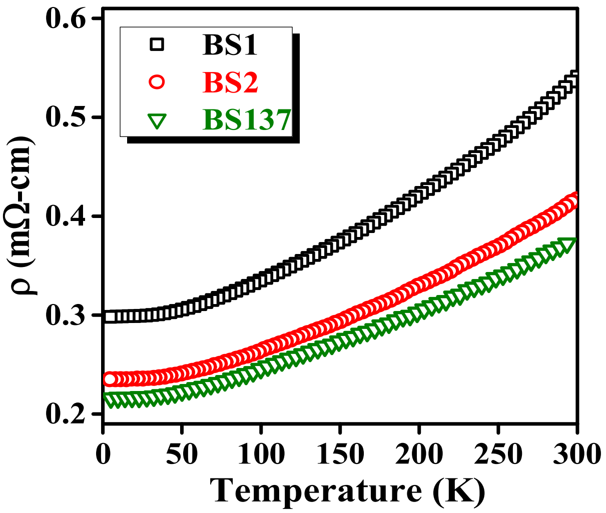

Figure 3.11 – Resistivity vs. Temperature data for the Bi_2Se_3 single crystals grown at different cooling rates.

To understand the resistivity behaviour, it is essential to look at the charge carrier concentration in the samples, which is determined from the Hall Effect measurements

3.2.3 Hall Effect measurements

Figure 3.12(a) shows the data of Hall Effect measurements on the single crystals of BS1, BS2 and BS137. The charge carrier concentration estimated from the slope of the Hall resistance (R_{xy}) vs. B curve at low fields is shown in Figure 3.12(b). It is observed that the charge carrier density (n) of both BS2 and BS137 are lesser in comparison to BS1. A possible reason for the lowering of charge carrier density in the samples cooled faster could be the reduction in number of Se vacancies by arresting Se evaporation from the lattice as a consequence of faster cooling rate.

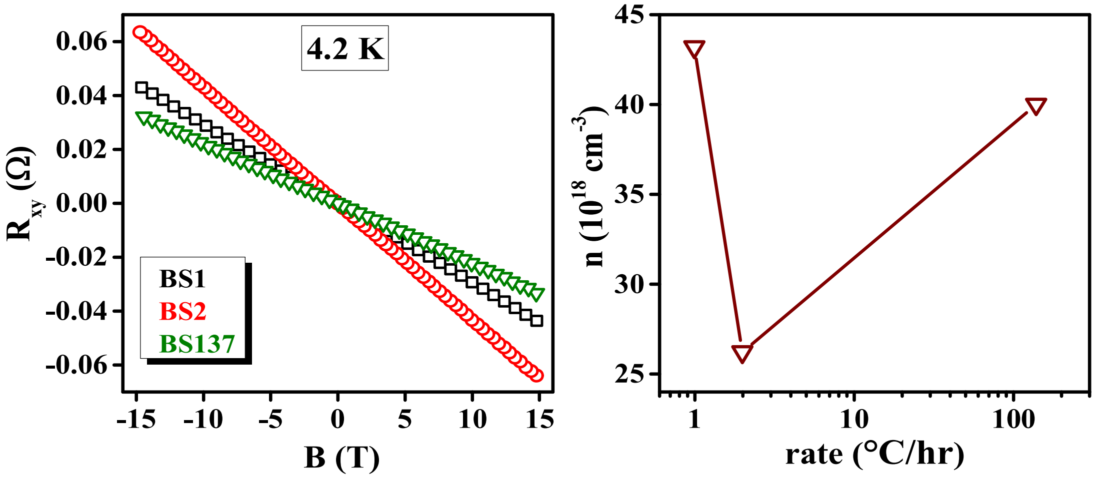

Figure 3.12 – **(a)** Hall effect data on the samples grown at different cooling rates; **(b)** variation of charge carrier density

The decrease in charge carrier density with increase in cooling rate implies that the resistivity must increase with increase in cooling rate. However, from Figure 3.11, it is observed that the resistivity decreases. The electron relaxation time estimated from the relation $\tau = \frac{m}{ne^2\rho}$, is found to be 0.15 ps, 0.33 ps, 0.41 ps for BS1, BS2, and BS137 at 300 K respectively. The increase in relaxation time suggests that the disorder in the system reduces, which is contrary to the result obtained from Laue diffraction which shows a streaking behaviour with increasing in cooling rate and points to an increase in disorder. The reduction in resistivity (as observed in Figure 3.11) can then be due to increased contribution from TSS in transport.

3.2.4 Magneto-resistance:

Figure 3.13 shows the MR data collected on the different stoichiometric Bi_2Se_3 crystals viz. BS1, BS2 and BS137 in $H\|c$ and $H\|ab$ configurations. It is observed that both BS2 and BS137 exhibit visible Shubnikov-de Haas oscillations only in the $H\|c$ configuration which suggest that the oscillations arise from an underlying 2D Fermi surface. The L-K equation analysis [18] is carried out on the oscillatory component of MR in both BS2 and BS137. The fits to the L-K equation are shown in Figure 3.14(a)-(b) for BS2 and BS137 respectively. The fitting parameters k_F, T_D, m_0, β and the various physical quantities derived from them are tabulated in Table 3.2.

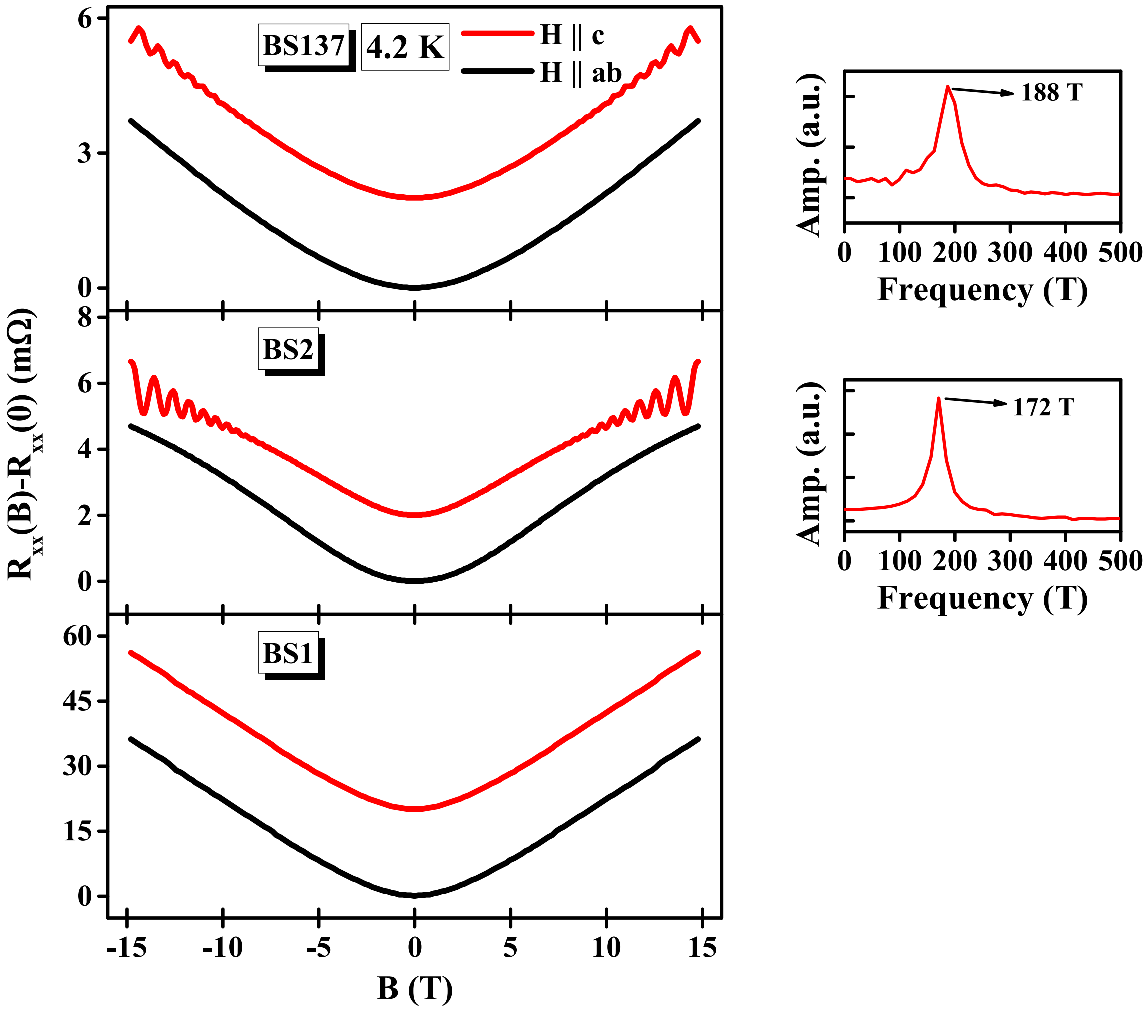

Figure 3.13 – MR data on Bi_2Se_3 crystals grown at different cooling rates viz. BS1, BS2 and BS137. Oscillations in MR were observed in the crystals BS2 and BS137 in the H‖c configuration. On the right side of each panel are the corresponding FFT plots indicating the frequency of oscillations.

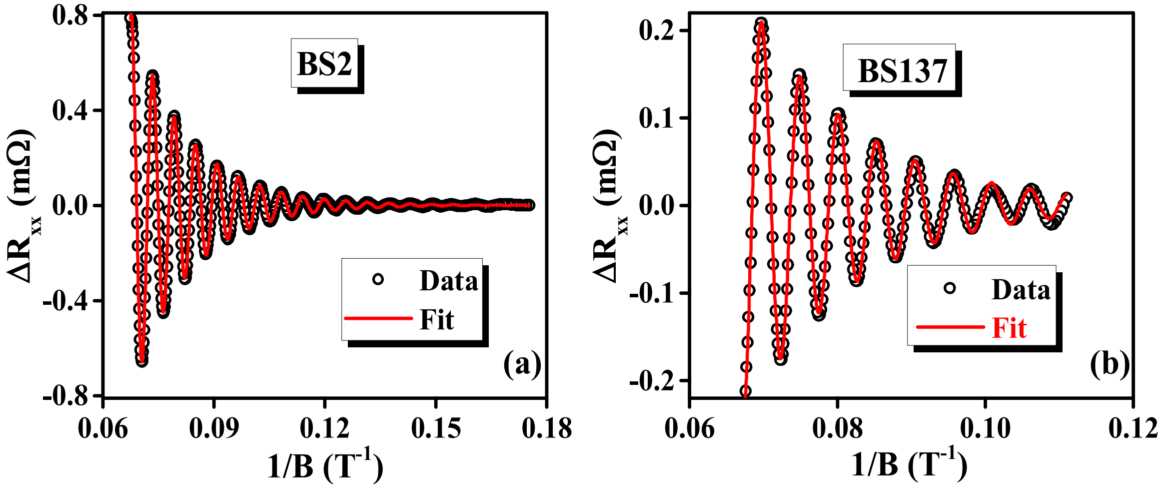

Figure 3.14 – L-K equation fit to the oscillations observed in the H‖c configuration in MR in **(a)** BS2; **(b)** BS137

Table 3.2 The fitting parameters and the derived physical quantities from the L-K equation fit to the oscillations in BS2 and BS137 in H‖c configuration

Fitting Parameters	**BS2**	**BS137**
Applied Magnetic Field Direction	**H‖c**	**H‖c**
Fermi wave-vector k_F (10^6 cm^{-1})	7.2321	7.6486
Dingle Temperature T_D (K)	25.61	38.87
Cyclotron mass m^* (m_0)	0.1523	0.1055
quantum scattering time [$\tau_q = \hbar/(2\pi k_B T_D)$] (fs)	47.46	31.27
Fermi velocity [$v_F = (\hbar k_F)/m^*$] (10^5 ms^{-1})	5.49	8.38
2D carrier density [$n_s = (k_F^2)/4\pi$] (*$10^{12}cm^{-2}$)	4.16	4.65
Surface mean free path [$l_s^{SdH} = v_F \tau_q$] (nm)	26.07	26.20
surface mobility [$\mu_s^{SdH} = (e l_s^{SdH})/(\hbar k_F)$]($cm^2$/V.s)	547	519
β	0.5	0.46
g	2	2

It can be seen from Table 3.2 that the value of β for BS2 and BS137 are 0.5 and 0.46, which are nearly equal to the ideal value of 0.5 for transport from Topological Surface States. To further confirm the validity of the Berry's phase obtained from the L-K equation fit, the preferred approach in literature [7] is to carry out a Landau-Level Fan diagram analysis of the SdH oscillations in which the maxima and minima in SdH oscillations in $1/B$ are plotted against an index "*n*", which is undefined upto an addition or subtraction by an integer. With respect to TI systems, as suggested by Ando [7], the oscillations in resistivity are first converted to oscillations in conductivity using the relation $\sigma_{xx} = \frac{\rho_{xx}}{\left(\rho_{xx}^2 + \rho_{xy}^2\right)}$, following which the minima and maxima in conductivity oscillations are assigned integer and half-integer values respectively and plotted vs. $1/B_n$; B_n being the field at which the Fermi energy E_F lies in between two consecutive Landau Levels i.e. minima in oscillations in conductivity. The value of intercept at 0 T^{-1}, obtained from a linear fit to the data; with slope being fixed by the frequency of oscillations, obtained from the FFT analysis to determine the exact nature of the 2D oscillations – for TSS, the presence of a π Berry phase would lead to an intercept of 0.5 in the LL fan diagram. The LL-Fan diagrams obtained for BS2 and BS137 are shown in Figure 3.15(a) and Figure 3.15(b) respectively. The intercept values obtained from the LL-Fan diagram analysis are 0.5 for BS2 and 0.25 for BS137.

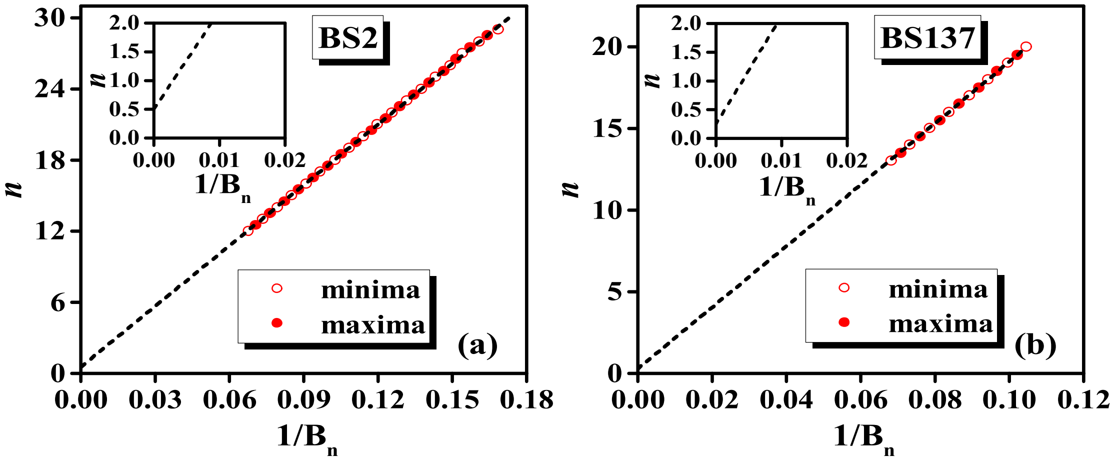

Figure 3.15 – Landau Level Fan diagram (*n* vs. $1/B_n$ plot) for the oscillations in conductivity in **(a)** BS2; **(b)** BS137. The insets in the figures are the same plots in expanded scale to show the intercept in "n" axis with more clarity.

The intercept of 0.5 obtained from the LL Fan diagram for BS2 sample indicates that the oscillations may arise from the 2D TSS. This is further confirmed by the Fermi velocity value of $v_F \sim 5.49*10^5$ ms^{-1} obtained from the L-K equation fit to the SdH oscillations, which agrees well the literature value of $5*10^5$ ms^{-1} obtained from ARPES measurements on Bi_2Se_3 by Y. Xia et al. [2] In addition, the single valued frequency value of 172 T corresponds to a large Fermi surface as expected for the TSS. Though observed SdH oscillations in the H‖c configuration in BS137 also suggests a 2D origin with a large Fermi surface (F = 188 T), the intercept value of 0.25 indicates that the oscillations observed are not purely from the Topological Surface States.

From the above results in section 3.1 and section 3.2, it is seen that SdH oscillations arising from a single frequency are observed only in samples that exhibit a predominant strain in their Laue patterns viz. $Bi_2Se_{3.1}$, $Bi_2Se_{3.2}$, BS2 and BS137. It is thus important to understand if this is in any way linked to controlling Se vacancies (as observed from Hall Effect data) that introduce charge carriers in the system, leading to shift of the Fermi level away from the Dirac point, and it is with this motivation, positron lifetime measurements are carried out.

3.3 Positron Lifetime measurements:

Figure 3.16 shows the results of positron lifetime measurements carried out at room temperature for the various samples synthesized viz. stoichiometric Bi_2Se_3 which includes BS1 and BS2; Bi rich $Bi_{2.1}Se_3$; Se rich $Bi_2Se_{3.1}$, $Bi_2Se_{3.2}$, on which the magneto-resistance measurements have been carried out. Lifetime measurements on BS137 crystals could not be carried out as the size of the cleaved crystals were very small in comparison to the positron source which would have lead to a large source and background component in the experimental data and thus error in the measured lifetime value. The lifetime values obtained experimentally for the various samples are tabulated in Table 3.3. It is observed that the positron lifetime reduces with the increase in Se/Bi ratio. The lifetime of BS2 sample is also found to be lower than that of BS1.

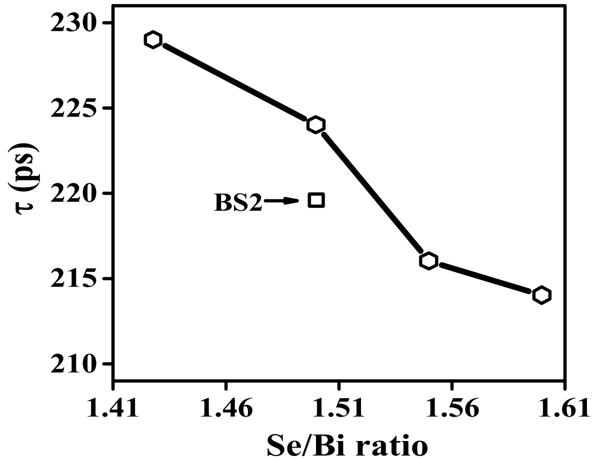

Figure 3.16 – Positron lifetime value on the various single crystals synthesized in the present study. The data points represented by open hexagons are the samples synthesized with varying Se/Bi ratio. The data point represented by an open square corresponds to the sample BS2.

Table 3.3 Carrier concentration n obtained from the low field Hall data, experimental positron lifetime τ and Se vacancy concentration estimated from positron experiments

Sample	**Charge carrier density from Hall n (10^{18} cm^{-3})**	**Positron Lifetime τ (ps)**	**V_{Se} (10^{17} cm^{-3})**
$Bi_{2.1}Se_3$	28.3	229±2	5.4
Bi_2Se_3 (BS1)	43.2	224±2	2.8
$Bi_2Se_{3.1}$	6.1	216±2	1.1
$Bi_2Se_{3.2}$	1.2	214±2	0.9
Bi_2Se_3 (BS2)	26.2	219±2	1.6

From Table 3.3 it is observed that with the decrease in charge carrier density corresponding to the increase in Se/Bi ratio, the positron lifetime decreases. To understand the experimental positron data, theoretical estimates of positron lifetimes are carried out from a calculation of the overlap of the positron density distribution with the electron density within the unit cell. These calculations are carried out for both the perfect crystal, and crystal containing various vacancy defects, viz., vacancy at the Se(1), Se(2) and the Bi site. The positron density distribution is calculated by solving the Schrödinger equation for the positron, using the Doppler code [19]. Figure 3.17 shows the plot of the positron density distribution in crystalline Bi_2Se_3 and in the presence of a vacancy at the Bi, Se(1) and Se(2) sites.

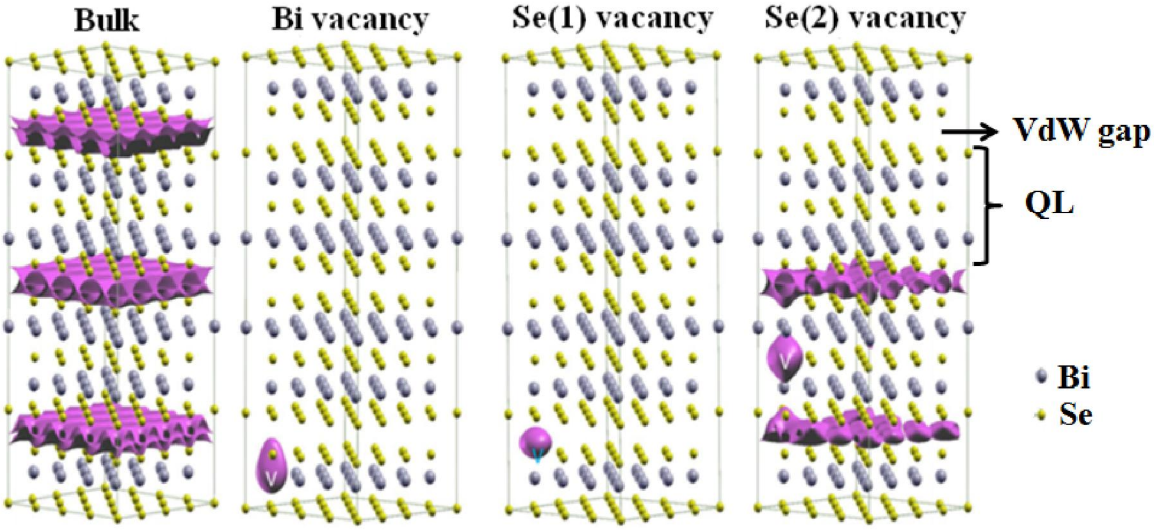

Figure 3.17 – Positron density distribution in crystalline Bi_2Se_3 and in the presence of vacancy at Bi, Se(1) and Se(2) sites. The positron density distribution for vacancies is carried out for the 441 super-cell, with vacancies in each layer. In defect-free Bi_2Se_3, the positron density is confined to the van der Waals gap, and in the presence of Bi and Se(1) vacancy, it gets localized at the vacancy site. For the Se(2) vacancy within the quintuplet layer, the positron samples both the vacancy and the van der Waals gap. The overlap of this positron density distribution with the atomic superposition of electron density is used to calculate the corresponding positron lifetimes.

As discussed in section 1.8 in the introduction chapter, the structure of Bi_2Se_3 consists of two non-equivalent Se positions in the lattice Se(1) and Se(2). Se(1) lies close to the Vander Waals gap and Se(2) lies sandwiched between the two Se(1)-Bi layers. It is seen that in the perfect crystalline solid the positron density is confined to the Van der Waals gap in the Bi_2Se_3 structure, which are the open regions within the crystal. In the presence of Bi and Se(1) vacancy, it gets localized at the vacancy site. For the Se(2) vacancy within the quintuplet layer, the positron density is diffuse in that it samples both the vacancy and the Van der Waals gap. The above positron density distribution in the presence of vacancies has been calculated using a super-cell of 441 unit cells. Using the above positron density distribution, the annihilation rate is calculated from the overlap with the electron density. The positron total annihilation rate (λ_{tot}) is given by [20]

$$\lambda_{tot} = \lambda_{core} + \lambda_{val} \tag{3.2}$$

Where, λ_{core} arises from the annihilations from the core electron density and λ_{val} is the annihilation rate from the valence electron density. For these calculations, the electronic configuration of Bi is taken to be ([Xe] $4f^{14}$ $5d^{10}$) $6s^2$ $6p^3$ and Se to be ([Ar] $3d^{10}$ $4s^2$) $4p^4$, with the orbitals in brackets taken as core electrons and those outside as valence electrons. The above partitioning into valence and core electrons seems reasonable, as recent band structure calculations [21] suggests that the electronic structure of Bi_2Se_3 is well represented as ppσ bonding of the 6p Bi and 4p Se orbitals. The annihilation rate is calculated taking into account the enhancement of valence electron density around the positron [22]. Using the above methodology, the positron lifetime in defect free Bi_2Se_3 bulk is calculated to be 201 ps. In the case of positron localization and annihilation at Se(1), Se(2) and Bi vacancies, the lifetimes sre calculated to be 238 ps, 202 ps and 224 ps respectively (ref. Table 3.4). It is seen that the positron lifetime at Se(2) vacancy, within the quintuplet layer is not very different from that in the bulk. This is also reflected in the fact that the positron density distribution is not very localized for the Se(2) vacancy (ref. Figure 3.17), and the binding energy is small as indicated in Table 3.4 implying that vacancy at Se(2) site is not an efficient positron trap.

Table 3.4 The calculated lifetimes in the perfect crystal of Bi_2Se_3 and at various vacancy defects. The positron binding energies at various vacancy defects are also shown. Se(1) is vacancy in the Se layer closest to the van der Waals gap, the Se(2) is vacancy in the Se layer inside the quintuple layer.

Species	τ (ps)	Binding energy (eV)
Bi_2Se_3(bulk)	201	0.0
Se(1) vacancy	238	0.281
Se(2) vacancy	202	0.014
Bi vacancy	224	0.213

However, the other Se vacancy, viz., the Se(1) vacancy near the Van der Waal gap is a deep trap for positrons with a lifetime substantially higher than that of the bulk. Experimentally, the positron lifetimes for the various samples $Bi_{2.1}Se_3$, Bi_2Se_3 (BS1), $Bi_2Se_{3.1}$, $Bi_2Se_{3.2}$ and BS2 were measured to be 229 ps, 224 ps, 216 ps, 214 ps and 219 ps respectively (ref. Table 3.3). First it is noted that these values are larger than the calculated bulk lifetime of 201 ps, clearly pointing to the localization and annihilation from vacancy type defects. To identify the specific vacancy defect, it is first noted that in the detailed first principles calculations by D. West et al. [5] who had incorporated a spin-orbit coupling component, it was shown that formation energy of vacancy at the Bi site was significantly larger (by a factor of 3) than that at Se site, for both Bi rich and Se rich conditions, and it was the V_{Se} that determined the n-doping level in Bi_2Se_3. Hence, the vacancies at the Bi site as a possible positron trap are not considered here. Amongst the two possible vacancy type defects at the Se site, it has already been noted that the vacancy at Se(2) is a weak trap with a lifetime (202 ps), not different from the bulk value. Hence it is inferred that the positron lifetime in the Bi_2Se_3 samples arises due to positron trapping and annihilation at the Se(1) vacancy. Using this assumption, the concentration of Se(1) can be determined from the measured value of lifetimes on samples of varying compositions within the framework of the two state trapping model [20][22]. The measured mean lifetime τ_m is given by

$$\tau_m = \tau_b \left[\frac{1 + K\tau_v}{1 + K\tau_b} \right] \tag{3.3}$$

Where τ_b is the bulk lifetime (201 ps), τ_v is the lifetime at the Se(1) vacancy (238 ps) and K is the trapping rate defined as $K = \mu_v C_v$, where μ_v is the specific trapping rate at a vacancy and C_v is the vacancy concentration. For the specific rate at the Se vacancy in Bi_2Se_3, the value for trapping rate at Se vacancy in $CuInSe_2$, viz., $\mu_v = 1 \times 10^{15}\ s^{-1}$ [24] is used. The resultant vacancy concentrations in the five samples are indicated in Table 3.3. It is observed that the concentration of vacancies, as obtained from positron experiments, is consistent with the theoretically predicted decrease in Se vacancies when grown under Se rich conditions [5].

3.4 Discussion:

From our experiments we observe that SdH oscillations are absent in the stoichiometric BS1 sample. However on addition of excess Se and growing the stoichiometric crystals at faster cooling rate, both of which introduces strain in the lattice, the SdH oscillations are being observed. Absence of SdH oscillations in the stoichiometric Bi_2Se_3 sample have been earlier reported by Butch et al. [10]. As discussed in Section 1.10, the explanation for absence of SdH oscillations was put forth by Brahlek et al. [13] based on the phenomena of band-bending occurring at the metal/semiconductor interface in Bi_2Se_3. The absence of oscillations in MR was attributed to the presence of downward band-bending in Bi_2Se_3 [13]. In the case of downward band bending (ref. Figure 1.24(b)), the size of the Fermi surface of the TSS becomes much larger than in the case of an upward band bending (ref. Figure 1.24(c)). As the period of the oscillations varies inversely as the cross-sectional area of the Fermi surface, a larger Fermi surface would translate into a small period of oscillation which would make the observations of oscillations from TSS in transport difficult. Also, the presence a downward band-bending leads to the accumulation of surface charges leading to formation of quantum well structures (QWS) which have the characteristics of a conventional 2D electron gas (Figure 1.24(b)). The presence of such a 2DEG state has been experimentally confirmed by M. Bianchi et al. using ARPES (cf. Figure 1.25) [25]. These states have high mobility and thus oscillations from these QWS also exhibit 2D characteristics and hence the transport would have mixed signatures from both these QWS and the TSS. However, the only difference arises because the dispersion of electrons in a conventional 2DEG is essentially parabolic and does not carry the π Berry phase of the relativistic Dirac fermions of the TSS and thus would not give an intercept of 0.5 in the LL Fan diagram analysis, as seen from the result for sample BS137 (ref. Figure 3.15(b)). Thus origin of oscillations in BS137 sample can be attributed to a mixed contribution from the conventional 2DEG that forms due to band-bending and the TSS. As discussed at the end of section 3.1.4, the SdH oscillations in $Bi_2Se_{3.1}$ and $Bi_2Se_{3.2}$ in H‖c configuration have contributions from both the bulk 3D Fermi surface and the 2D TSS with the bulk characteristics predominant. However the absence of 2 frequencies that should arise from the two different Fermi surfaces and should be seen in FFT of oscillations can be explained if the two Fermi levels lie in close proximity to each other such that their cross-section areas are nearly the same. As discussed in Section 3.2.4, the oscillations in the sample BS2 are purely from the TSS.

It is also noted that the oscillations from TSS are observed in the samples with inherent strain, as inferred from their Laue patterns. This observation is further supported by a recent study on thin films of Bi_2Se_3 by Liu et al. [17] where it has been demonstrated with the help of calculations and Scanning Tunneling Microscopy data that the introduction of low angle grain boundaries in Bi_2Se_3 plays a major role in shifting the Dirac point (as shown in Figure 3.18). The unshifted band structure of the bulk and the TSS are shown as solid lines, where there is downward band bending. In a strained crystal, the Dirac point (DP) shifts such that the band-bending becomes upward, resulting in the domination of transport from non-trivial surface states.

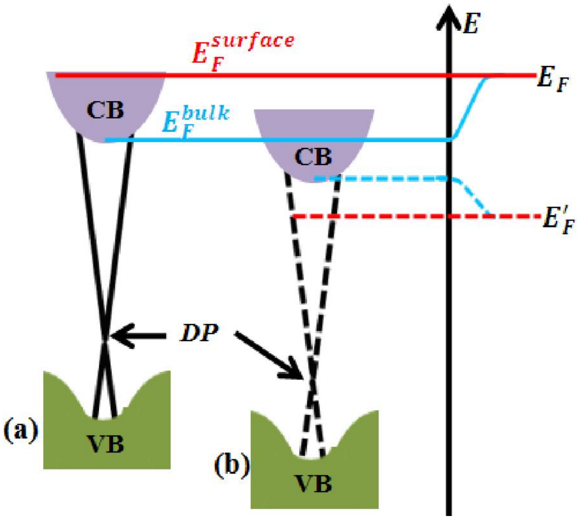

Figure 3.18 – (a) Downward band bending in stoichiometric Bi_2Se_3 (BS1) (red lines denote the E_F of the surface state, blue lines denote the Bulk E_F); **(b)** In samples with strain (shown with broken lines), the Dirac point shifts due to strain leading to the upward band bending.

3.5 Conclusion

Bi_2Se_3 crystals, synthesized by varying growth conditions such as Se/Bi ratio and rate of cooling were subjected to detailed Magneto-transport and Positron Lifetime studies. From Positron Lifetime experiments and calculations it is observed that Se vacancies play the major role in n-type doping of the Bi_2Se_3 system. From Laue diffraction experiments and magneto-transport measurements it is noted that while SdH oscillations are not observed in the Bi_2Se_3 sample with perfect crystalline nature, introduction of stacking faults and low angle grain boundaries that induce strain in the lattice can shift the Dirac point to lower energies (as shown in Figure 3.18) leading to an upward band bending and consequently in the manifestation of signature of Topological Surface States (TSS) in transport measurements.

References

[1] Haijun Zhang, Chao-Xing Liu, Xiao-Liang Qi, Xi Dai, Zhong Fang & Shou-Cheng Zhang, *Nature Physics* **5**, (2009) 438

[2] Y. Xia, D. Qian, D. Hsieh, L. Wray, A. Pal, H. Lin, A. Bansil, D. Grauer, Y. S. Hor, R. J. Cava & M. Z. Hasan, *Nature Physics* **5**, (2009) 398

[3] M. Z. Hasan & C. L. Kane, *Rev. Mod. Phys.* **82** (2010) 3045

[4] Dimitrie Culcer, *Physica E* **44** (2012) 860

[5] D. West, Y. Y. Sun, Han Wang, Junhyeok Bang, & S. B. Zhang, *Phys. Rev. B* **86** (2012) 121201

[6] L. Xue, P. Zhou, C. X. Zhang, C. Y. He, G. L. Hao, L. Z. Sun & J. X. Zhong, *AIP* Advances **3** (2013) 052105

[7] Y. Ando, *J. Phys. Soc. Jpn.* **82** (2013) 102001

[8] G. R. Hyde, H. A. Beale & I. L. Spain, *J. Phys. Chem. Solids* **34** (1974) 1719

[9] James G. Analytis, Jiun-Haw Chu, Yulin Chen, Felipe Corredor, Ross D. McDonald, Z. X. Shen & Ian R. Fisher, *Phys. Rev. B* **81** (2010) 205407

[10] N. P. Butch, K. Kirshenbaum, P. Syers, A. B. Sushkov, G. S. Jenkins, H. D. Drew & J. Paglione, *Phys. Rev. B* **81** (2010) 241301(R)

[11] Kazuma Eto, Zhi Ren, A. A. Taskin, Kouji Segawa & Yoichi Ando, *Phys. Rev. B* **81** (2010) 195309

[12] M. Petrushevsky, E. Lahoud, A. Ron, E. Maniv, I. Diamant, I. Neder, S. Wiedmann, V. K. Guduru, F. Chiappini, U. Zeitler, J. C. Maan, K. Chashka, A. Kanigel &Y. Dagan, *Phys. Rev. B* **86** (2012) 045131

[13] Matthew Brahlek, Nikesh Koirala, Namrata Bansal & Seongshik Oh, *Solid State Communications* **54** (2015) 215

[14] W. Kraus & G. Nolze *J. Appl. Cryst.* **29** (1996) 301

[15] Gene E. Ice and Judy W.L. Pang, *Mater. Charact.* **60** (2009) 1191

[16] B. D. Cullity, *Elements of X-Ray Diffraction* (Addison-Wesley Publishing Company, Inc., Massachusetts) 1956 p. 246

[17] Y. Liu, Y. Y. Li, S. Rajput, D. Gilks, L. Lari, P. L. Galindo, M. Weinert, V. K. Lazarov & L. Li, *Nature Phys.* **10** (2014) 294

[18] D. Schoenberg, *Magnetic Oscillations in metals* (Cambridge University Press, London) 1984 p. 66

[19] J. Kansy, *Nucl. Instr. Methods A* **374** (1996) 235

[20] M. J. Puska and R. M. Nieminen, *Rev. Modern Phys.* **66** (1994) 841

[21] S. K. Mishra, S. Satpathy & O. Jepsen, *J. Phys.: Condens. Matter* **9** (1997) 461

[22] B B. Barbiellini, M. J. Puska, T. Torsti, & R. M. Nieminen, *Phys. Rev. B.* **51** (1995) 7341

[23] C. S. Sundar, *Bull. Mater. Sci.* **17**, (1994) 1215

[24] A. Polity, R. Krause-Rehberg, T. E. M. Staab, M. J. Puska, J. Klais, H. J. Möller & B. K. Meyer, *J. Appl. Phys.* **83** (1998) 71

[25] Marco Bianchi, Dandan Guan, Shining Bao, Jianli Mi, Bo Brummerstedt Iversen, Philip D.C. King & Philip Hofmann, *Nat. Commun.***1** (2010) 128.

Chapter 4

Magneto-transport studies on Sb substituted Bi_2Se_3 single crystals

The paper by Zhang et al. [1] on 3D Topological Insulators (TIs) Bi_2Se_3, Bi_2Te_3 and Sb_2Te_3 had pointed out that a similar compound Sb_2Se_3 does not show a topologically non-trivial phase. The reason ascribed was the absence of adequate spin-orbit coupling (SOC) strength in Sb_2Se_3 that could bring about a band-inversion at the Γ point, observed in the other three materials. It would be of interest to study the effect of substituting Sb with a smaller SOC parameter (of 0.40 eV) in the place of Bi (SOC parameter = 1.25 eV), in Bi_2Se_3 and in turn see the effect on the signatures of Topological Surface States in transport measurements viz. Shubnikov de Haas oscillations. Since the end compounds viz., Bi_2Se_3 and Sb_2Se_3 are topologically distinct; a quantum phase transition is expected to occur at a certain critical concentration (x_c) of Sb substitution. Independent ab-initio calculations on the $Bi_{2-x}Sb_xSe_3$ system by Liu et al. [2] and Abdalla et al. [3] determined the value of $x_c = 1.2$, corresponding to the alloy composition $Bi_{0.8}Sb_{1.2}Se_3$. However experimentally, the solid solubility of the Sb_2Se_3 in Bi_2Se_3 is less than 16 mol% [4] and it is therefore difficult to synthesize single phase crystals with Sb substitution required to observe the Quantum Phase transition.

The transport co-efficients viz. Hall co-efficient R_H, electrical conductivity σ and the Seebeck co-efficient α of the $Bi_{2-x}Sb_xSe_3$ system as a function of temperature in the solid solubility range were first reported by Drašar et al [5]. Kulbachinskii et al. [6] was the first to observe Shubnikov de Haas oscillations (SdH) on $Bi_{2-x}Sb_xSe_3$ single crystals. However this study was undertaken before Bi_2Se_3 was identified as a TI and hence it is worthwhile to repeat the experiment and understand it in this context of the subject of TI. Zhang et al. presented a detailed ARPES study on MBE grown $Bi_{2-x}Sb_xSe_3$ thin films in which they observed that with increase in Sb substitution till x = 0.3, the Dirac point shifted towards the Fermi level and then disappeared for higher concentration [7]. Here we look at how the SdH oscillations from the TSS in Bi_2Se_3, evolves with Sb substitution in the bulk single crystalline form. Since the previous chapter clearly indicated that the stoichiometric Bi_2Se_3 sample BS2, corresponding to the cooling rate of 2°C/hour exhibits oscillations from the Topological Surface States, we use this procedure for all substitutions. Thus we investigate the effect of lowering of SOC and reduction of bulk band gap on the presence of TSS in the system, in particular its effect on the transport behaviour.

4.1 Synthesis and X-Ray diffraction

Single crystals of $Bi_{2-x}Sb_xSe_3$ (x = 0, 0.05, 0.1, 0.3, 0.5) were grown by slow cooling stoichiometric melts of high purity Bismuth (Bi), Antimony (Sb) and Selenium (Se) from 850°C to 550°C for over 150 hours (2°C/hour), followed by annealing at 550°C for 24 hours and rapid cooling. Phase formation was checked by room temperature powder x-ray diffraction (XRD) on powdered single crystals carried out at BL-12 beam-line of Indus II, RRCAT – Indore. Figure 4.1 shows the powder diffraction data on the $Bi_{2-x}Sb_xSe_3$ crystals with all the peaks indexed to Rhombohedral Bi_2Se_3. Absence of peaks corresponding to elemental Sb or Sb-Se secondary phase confirms the substitution of Sb at Bi lattice position. Further a systematic shift in peak positions, in particular (015) peak (shown in Figure 4.2(a)) is observed in the powder diffraction pattern, indicating Sb substitution in Bi site. Impurity peaks indexed to elemental Selenium (marked as # in Figure 4.2(b)) are observed in the sample with x = 0.5 composition.

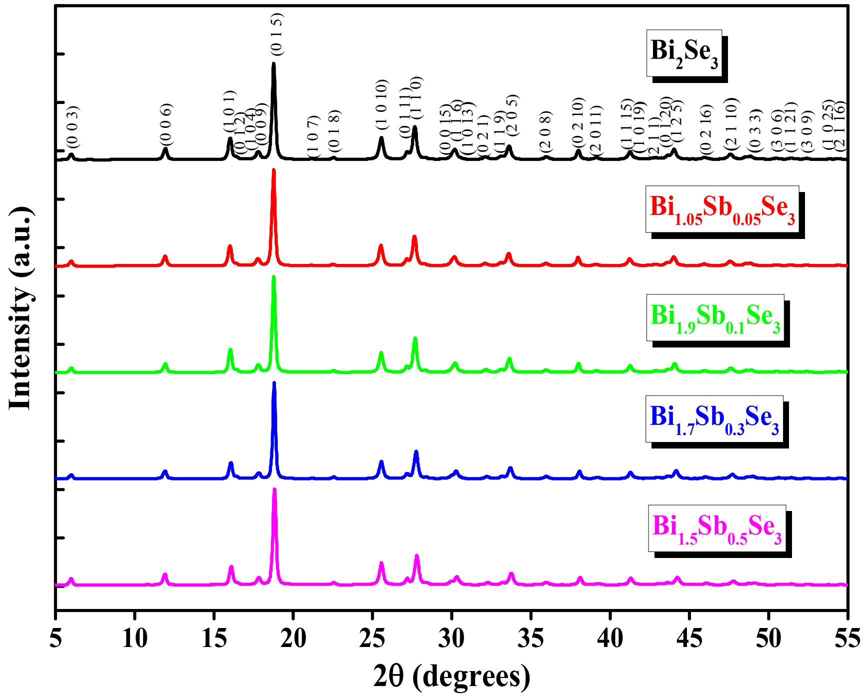

Figure 4.1 – Powder diffraction pattern of $Bi_{2-x}Sb_xSe_3$ crystals. The peaks have been normalised to the highest observed peak intensity and have been shifted vertically for clarity.

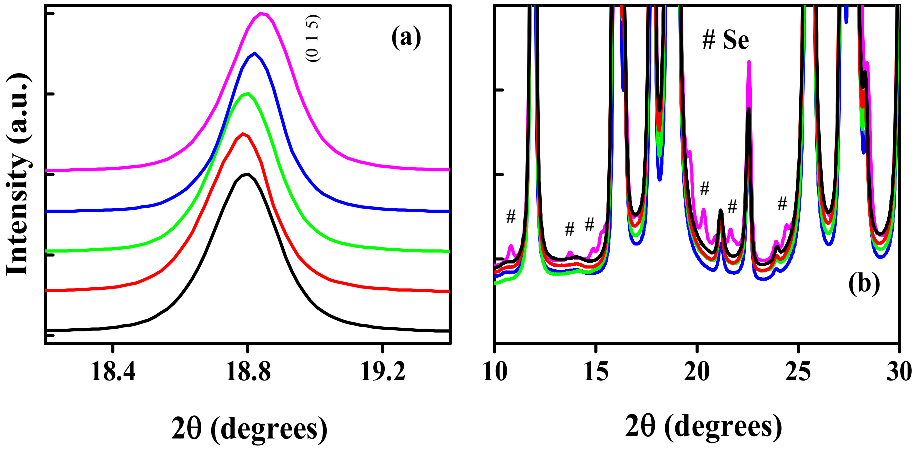

Figure 4.2 – **(a)** observed shift in the 100% peak (015) with increasing Sb substitution; **(b)** Se impurity peaks observed in sample x = 0.5 denoted by # at their positions.

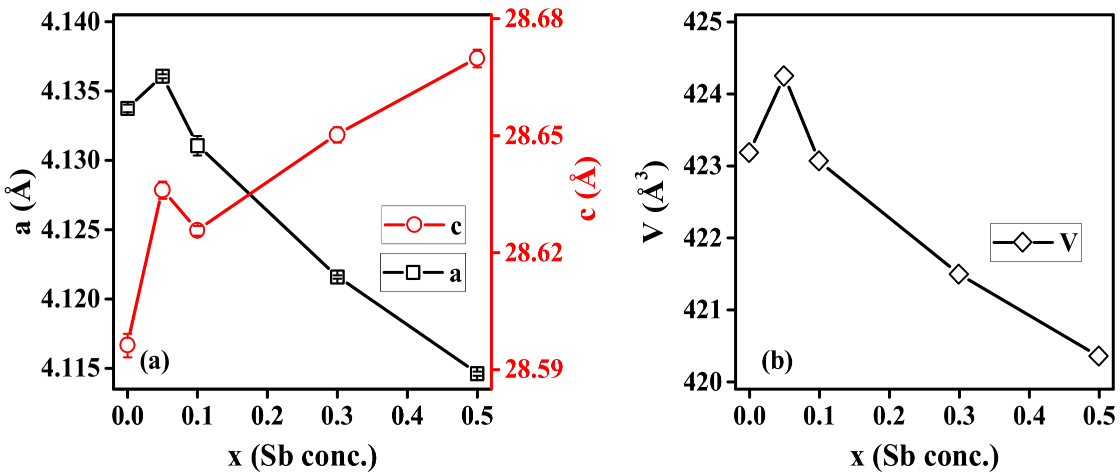

Figure 4.3 – (a) variation of *a* and *c* lattice parameters of $Bi_{2-x}Sb_xSe_3$ crystals as a function of Sb concentration; **(b)** variation of unit cell volume as a function of Sb concentration

Figure 4.3(a) shows the variation of *a* axis and *c* axis lattice parameters as a function of increasing Sb substitution, determined from the powder diffraction patterns using *PowderCell* [8]. It is evident from the figure that there is a non-monotonic variation in the lattice parameters with increasing Sb substitution. In particular, the *a* and *c* lattice parameters for x = 0.05 sample display an anomalous deviation from the overall variation. Figure 4.3(b) shows the variation of the unit cell volume as a function of increasing Sb substitution. The decrease of unit cell volume with increasing Sb substitution further substantiates the incorporation of Sb in the lattice, consistent with the smaller ionic radius of Sb when compared to Bi. We try to reconcile these observations of anomalous *a* and *c* lattice parameters variation with the help of their Laue diffraction patterns shown in Figure 4.4.

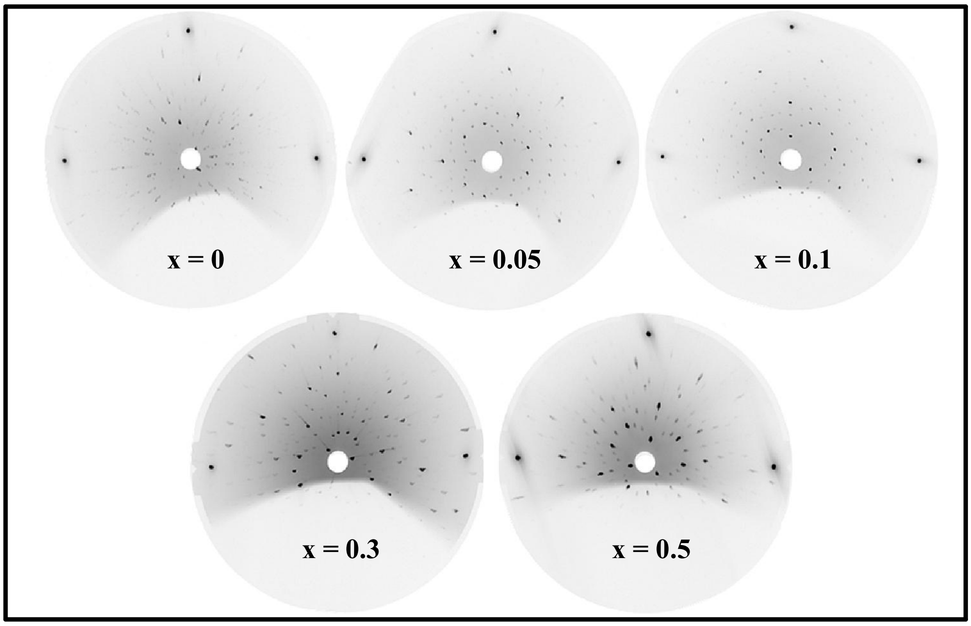

Figure 4.4 – Laue diffraction pattern of $Bi_{2-x}Sb_xSe_3$ crystals in the transmission geometry. The Laue spots in x = 0 sample display radial streaking

The Laue diffraction patterns on freshly cleaved crystals were recorded in the transmission mode using a Molybdenum X-ray source and a HD-CR-35 NDT image plate system. It is observed that the Laue spots in the pristine Bi_2Se_3 show radial streaking. Such streaking has been attributed to strain inhomogeneities [9][10] along the c-axis arising due the sub-stoichiometry of Se because of inherent Se vacancies. On introducing a small amount of Sb (x = 0.05), the lattice stabilizes as witnessed from the sharp spots in the Laue pattern, the c-axis parameter value increases to 28.636 Å. For x = 0.1, the value of c = 28.625 Å and the nature of the Laue spots does not change much from that of x = 0.05. For higher concentrations x = 0.3 and 0.5, the Laue spots become larger and also show slight radial streaking, which can be ascribed to the presence of a uniform strain in the lattice as is evident from the larger values of c = 28.650 Å & 28.669 Å for x = 0.3 & 0.5 respectively. The observed increase in *c* lattice parameter may also be attributed to the reduced cation-anion bonding strength on substitution of the larger and hence more polarizable ion (Bi) with a lighter one (Sb), which could result in an increase in the intra-QL distances and in turn expand the lattice parameter.

4.2 Resistivity

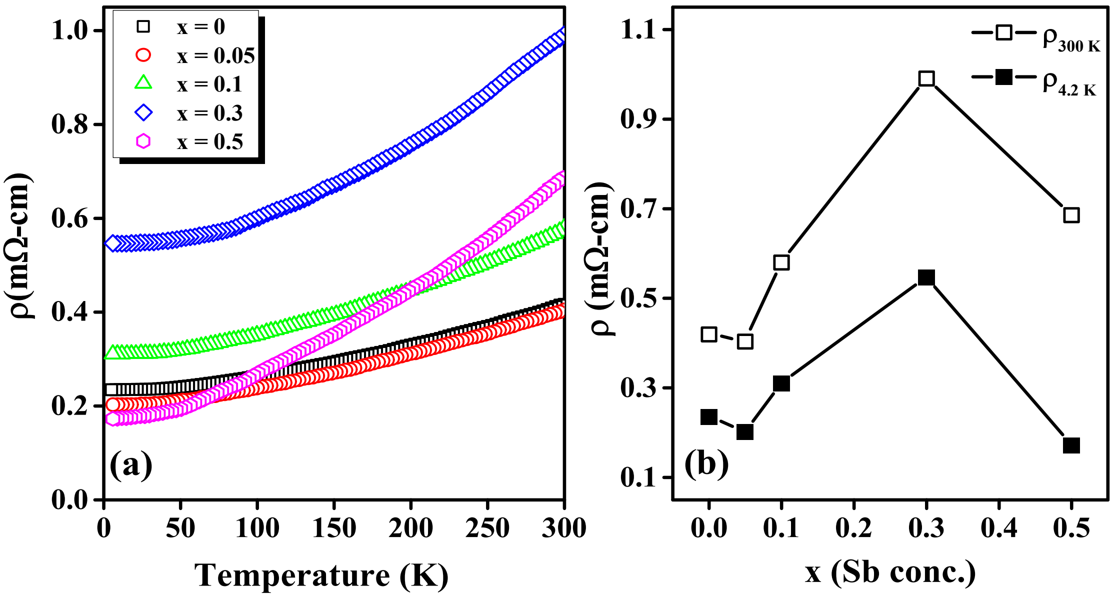

Figure 4.5 – (a) Resistivity vs. Temperature as a function of Sb concentration; **(b)** variation of resistivity as a function Sb concentration at 300 K (open symbol) and at 4.2 K (closed symbol)

Figure 4.5(a) shows the temperature dependent resistivity behaviour of the $Bi_{2-x}Sb_xSe_3$ samples. It is evident from the figure that resistivity behavior shows a positive temperature co-efficient and the low temperature resistivity shows a tendency to saturate to constant value below ~ 30 K. It is observed that the magnitude of resistivity shows an increase with Sb substitution. The variation of resistivity as a function of Sb concentration at 300 K and 4.2 K is shown in Figure 4.5(b). The resistivity value decreases marginally from that in the pristine sample to the low Sb concentration sample i.e. x = 0 and 0.05, whereas for higher Sb concentrations it shows an increase. The anomalous drop in resistivity value for x = 0.5 sample can be attributed to the presence of the secondary Se phase (cf. Figure 4.2(b)).This observed behaviour agrees well with earlier resistivity reports in $Bi_{2-x}Sb_xSe_3$ system [6]. To understand the reason for the observed variation in resistivity with Sb substitution, viz., whether the observed trend is a consequence of reduction in the number of carriers or due to introduction of disorder by Sb substitution, Hall Effect measurements are undertaken.

4.3 Hall Effect

Figure 4.6(a) shows the Hall Effect data on the various samples at 4.2 K. The linear behaviour and the negative slope indicate that the major charge carriers are electrons. The charge carrier density in $Bi_{2-x}Sb_xSe_3$ system, obtained from the low field slope of the Hall data, is plotted as a function of Sb concentration in Figure 4.6(b).

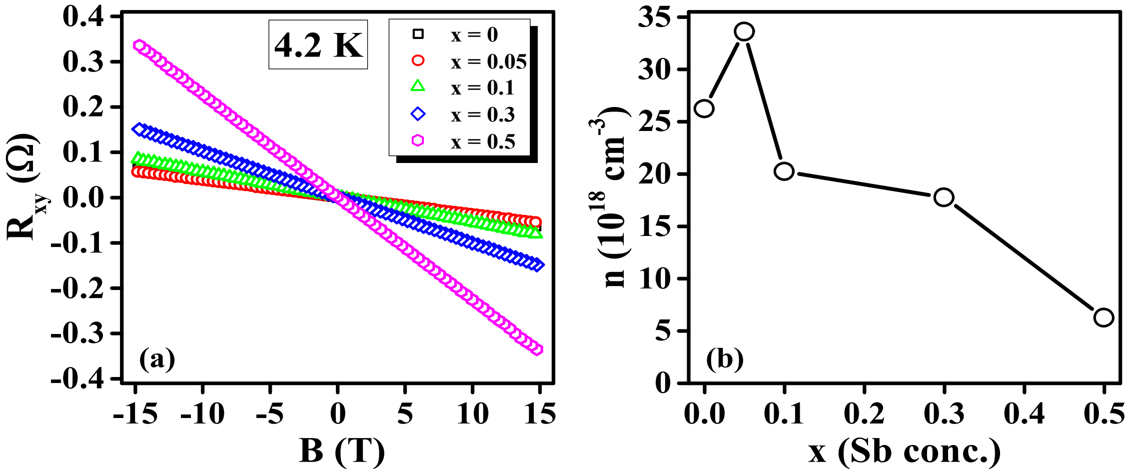

Figure 4.6 – (a) Hall resistance (R_{xy}) as a function of Sb concentration; **(b)** charge carrier density as a function of Sb concentration.

It is observed that the carrier density increases from 26 x 10^{18} cm^{-3} for the pristine Bi_2Se_3 to 33 x 10^{18} cm^{-3} in the low Sb concentration sample i.e. x = 0.05. At higher concentrations of Sb, the charge carrier density decreases, with pre-factors for x = 0.05 and x = 0.5 decreasing by ∽ 25. The overall variation of charge carrier density with increase in Sb concentration in the pristine Bi_2Se_3 lattice is consistent with earlier reports on the same system [6]. As Sb is an iso-electronic substituent at the Bi site in Bi_2Se_3, no external charges are expected to be introduced in the system. Besides, the decrease in unit cell volume as observed in Figure 4.3(b), can only lead to an increase in charge density, which implies that the reduction in charge density seen in the $Bi_{2-x}Sb_xSe_3$ system (ref. Figure 4.6(b)) is not due to volume change consequent to Sb substitution but could be due to defect introduced into the system by Sb substitution. To look for any possible variation in the vacancy concentration as a function of Sb substitution, we employ positron lifetime measurements.

4.4 Positron Lifetime measurements

Figure 4.7 shows the measured positron lifetime values (τ in ps) in the $Bi_{2-x}Sb_xSe_3$ samples. It is observed that the lifetime values decrease initially, from ~ 220 ps for the pristine Bi_2Se_3 to ~ 215 ps for $Bi_{1.9}Sb_{0.1}Se_3$ and then shows no further change in the higher Sb doping. Since the mean positron lifetime τ in a system is given by inverse of the total annihilation rate λ_{tot}, where λ_{tot} is proportional to the enhanced charge carrier density in the system [11]; the observed decrease in τ should imply an increase in charge carrier density if the positron annihilation is purely from the bulk charge density in the $Bi_{2-x}Sb_xSe_3$ samples, which is contrary to the Hall data (cf. Figure 4.6(b)). However the decreasing trend of the positron lifetime value with increase in Sb substitution could imply that Se vacancy concentration decreases with Sb substitution. This is substantiated by the fact that the theoretically estimated positron lifetime value (from Chapter 3) at uncompensated Selenium vacancy V_{Se1} is 238 ps, which is much larger than that compared to the value of 201 ps in bulk Bi_2Se_3 (ref. Table 3.4). The magnitude of lifetime values obtained in the $Bi_{2-x}Sb_xSe_3$ samples is consistent with the fact that V_{Se1} should be present in Bi_2Se_3 whose concentration decreases with Sb substitution. Thus the variation of charge carrier density obtained from Hall Effect measurements taken in conjunction with behaviour of positron lifetime behavior points to the decrease in the concentration of V_{Se1} with Sb substitution.

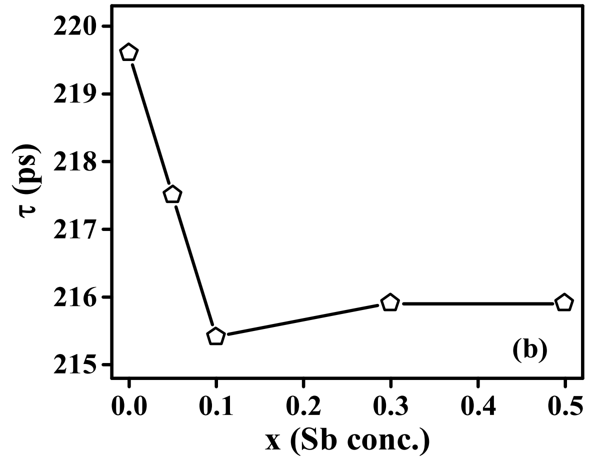

Figure 4.7 – Positron Lifetime as a function of Sb concentration in $Bi_{2-x}Sb_xSe_3$

As discussed in section 1.8, single crystalline Bi_2Se_3 with strong Spin-Orbit interaction (SOI) has the following defects: (i) anion vacancy V_A (V_{Se1}) – a double donor; (ii) cation antisite C_A (Bi_{Se}) – a single donor; (iii) anion antisite A_C (Se_{Bi}) – single donor and (iv) cation vacancy V_C (V_{Bi}) – a triple acceptor [12][13]. Since the Bi_2Se_3 system is known to have inherent Se vacancies, a crystal grown from stoichiometric precursors tends to be sub-stoichiometric in Se i.e. $Bi_2Se_{3-\delta}$, making it cation rich. Under cation rich conditions, the energies of formation of defects in pristine Bi_2Se_3 with increasing order of energies are $V_{Se} \leq Bi_{Se} < Se_{Bi} < V_{Bi}$ [12]. Thus the lowest formation energy is for V_{Se} and the negative carriers seen in the pristine Bi_2Se_3 crystals are consistent with the presence V_{Se} in the pristine Bi_2Se_3 crystals. Therefore, the reduction in positron lifetime with increase in Sb doping observed in the samples upto x = 0.1 can be attributed to the reduction in V_{Se1} with increase in Sb concentration in $Bi_{2-x}Sb_xSe_3$ samples. The reduction in Se(1) vacancies with increase in Sb concentration, can be attributed to the increase in the vacancy formation energy due to reduction in the unit cell volume (as observed in Figure 4.3(b)) with increase in Sb substitution [14]. The positron lifetime (cf. Figure 4.7) beyond x = 0.1 shows no change suggesting there is no further decrease in the V_{Se1} vacancy concentration for crystals with Sb fraction beyond x = 0.1. However, the charge carrier density obtained from Hall Effect measurements shows a further reduction even beyond x = 0.1, implying that carriers other than those that arise from V_{Se1}, could be responsible for charge density variations seen for these concentrations.

The observed decrease could be due to the reduction in the number of Bi_{Se} and Se_{Bi} antisite defects on substitution of Bi by Sb, which may contribute to the variation of charge density in the system, and the lack of variation in positron lifetime could arise because of positrons not being sensitive to antisite disorder. Taking clue from an earlier report by Van Vechten [15] which showed that in binary crystals iso-structural to Bi_2Se_3, the possibility of formation of a vacancy defect is determined by the surface area of the defect; the larger the surface area, the higher the energy of formation and vice-versa. Since the substitution of Sb at Bi site in Bi_2Se_3 leads to a reduction in the effective radius of the cation sub-lattice in $Bi_{2-x}Sb_xSe_3$ system, a reduction in the formation energy of cation vacancies V_C (V_{Bi}) is expected, which in turn could give rise to an increase in the number of V_{Bi} defects. Since the V_{Bi} defect level in Bi_2Se_3 is known to be a triple acceptor, it can also be responsible for the observed reduction in the charge density, shown in Figure 4.6(b). From our calculation in Chapter 3, the positron lifetime in uncompensated Bi vacancy was seen to be 224 ps, much higher than that in the bulk Bi_2Se_3 (201 ps). The increased lifetime from positron trapped at V_{Bi}, could also be responsible for the arresting of decrease in the positron lifetime at higher Sb concentration of x = 0.3 and 0.5. However, a triple acceptor would have a negligibly small mobility and may not show up as a positive contribution in Hall Effect measurement and as a consequence, non-linear slope of the Hall data versus magnetic field expected due to the presence of two types of carriers might not be observed.

4.5 Magneto-resistance

Figure 4.8 shows the Magneto-resistance (MR) plots ($R_{xx}(B)$-$R_{xx}(0)$ vs. B) of $Bi_{2-x}Sb_xSe_3$ samples in two different configurations – field out-of-plane (H||c) and field in-plane (H||ab). R_{xx} is the longitudinal resistance at each field applied and $R_{xx}(0)$ is the value of resistance at 0 T. It is observed that oscillations in MR viz. Shubnikov de-Haas (SdH) oscillations are observed in the samples i.e. x = 0, 0.05, 0.1 & 0.3 in H||c configuration alone and only in x = 0.5 in both H||c and H||ab configuration. As discussed in the previous chapter, in angular dependent magneto-resistance measurements, the positions of maxima and minima in oscillations depend only on the perpendicular component of field $(B_\perp)$ as $(B_\perp)^{-1} \equiv (B\cos\theta)^{-1}$, where θ is the angle between the field direction and the normal to the crystal surface [16]. If the oscillations disappear for θ = 90° i.e. the H||ab (field in-plane) configuration, the SdH oscillations could be from a 2D Fermi surface. It is evident from Figure 4.8 that oscillations are not observed for H||ab configuration, in x = 0, 0.05, 0.1 and 0.3 crystals which is a clear indication that the observed SdH oscillations for these compositions arise from an underlying 2D Fermi Surface. In x = 0.5 sample, oscillations are observed in both H||c and H||ab plane which suggest a bulk 3D origin.

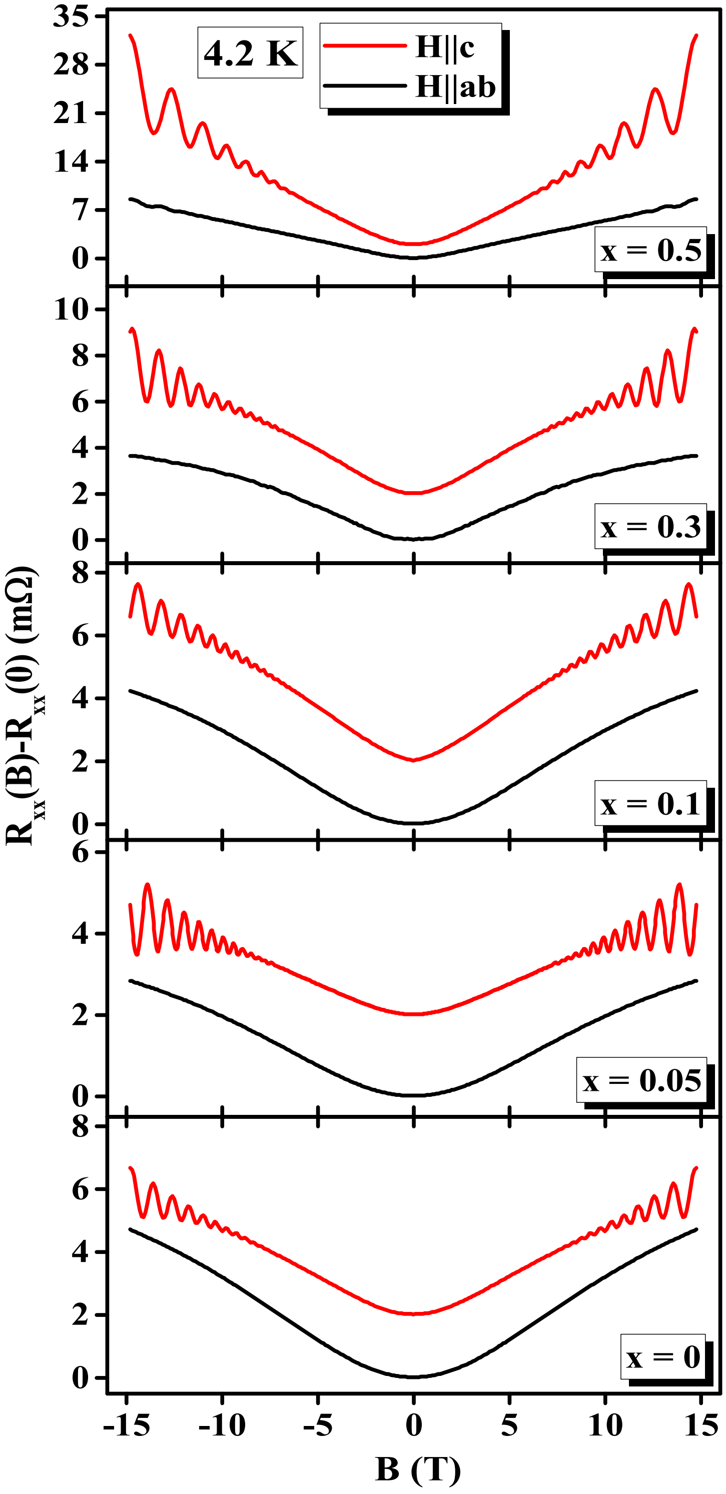

Figure 4.8 – Magneto-resistance data of $Bi_{2-x}Sb_xSe_3$ crystals. The data in both H||c and H||ab configuration are plotted in the same panel for each composition and are offset for clarity.

The SdH oscillations obtained experimentally are further analysed using the Lifshitz-Kosevich (L-K) equation [17] after suitable background subtraction. This fit results in the extraction of valuable parameters such as Fermi wave-vector (k_F), Fermi velocity (v_F). The L-K equation is given as [17]

$$\Delta R_{xx} = A_0 R_T R_D R_S \cos\left[2\pi\left(\frac{F}{B}+\frac{1}{2}-\beta\right)\right] \tag{4.1}$$

Figure 4.9 shows the L-K equation fit to the oscillatory component $\varDelta R_{xx}$, for all the compositions viz. x = 0, 0.05, 0.1, 0.3, 0.5 in the H||c configuration. As can be seen from the figure, the L-K equation fits are very good.

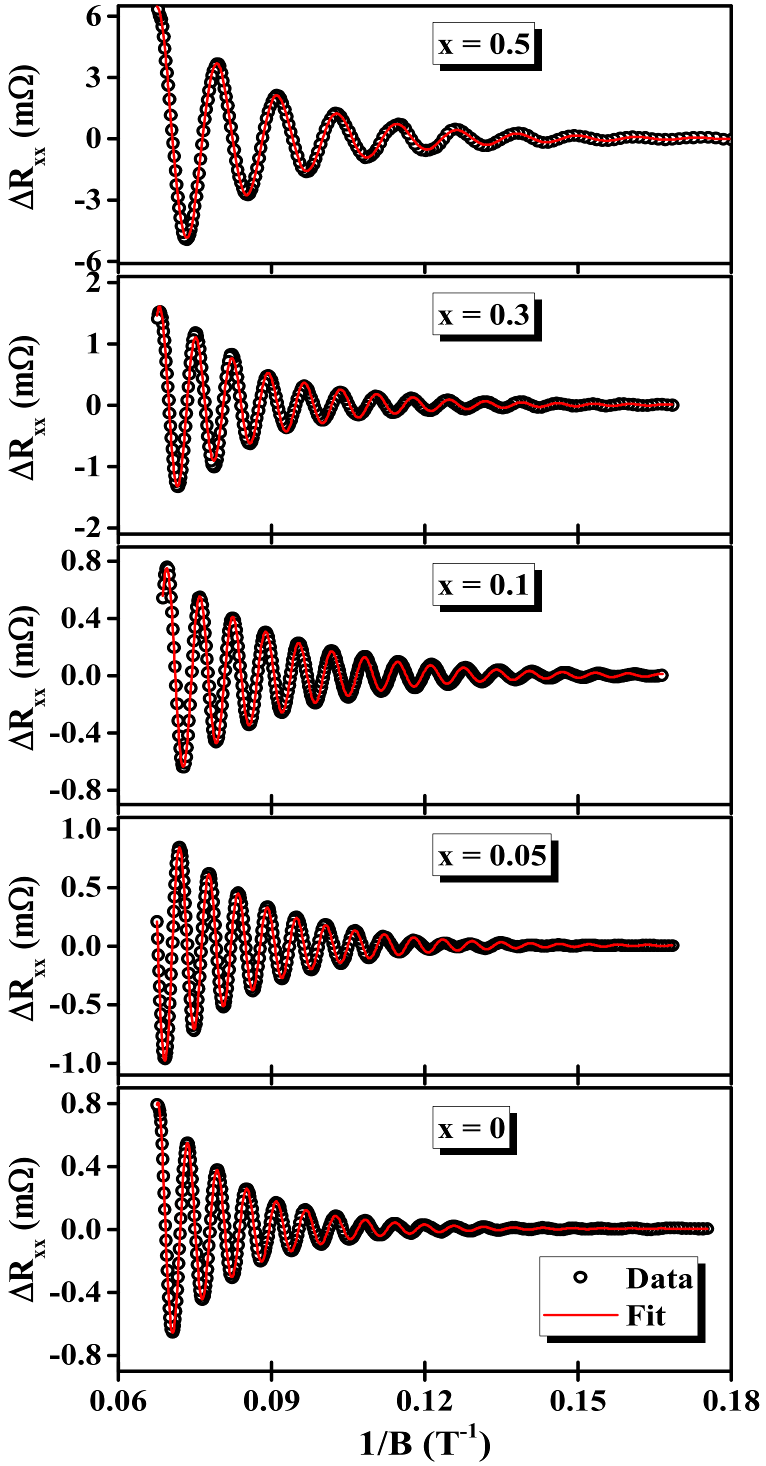

Figure 4.9 – L-K equation fit to the SdH oscillations in MR in $Bi_{2-x}Sb_xSe_3$

The fitting parameters k_F, T_D, m_0, β, g and other derived physical parameters obtained from the L-K equation fit to the MR data of $Bi_{2-x}Sb_xSe_3$ samples (x = 0, 0.05, 0.1, 0.3) are tabulated in **Table 4.1**.

Table 4.1 Fitting parameters and derived physical constants from L-K equation fit to SdH oscillations in $Bi_{2-x}Sb_xSe_3$ system.

Fitting Parameters	**Bi_2Se_3**	**$Bi_{1.95}Sb_{0.05}Se_3$**	**$Bi_{1.9}Sb_{0.1}Se_3$**	**$Bi_{1.7}Sb_{0.3}Se_3$**	**$Bi_{1.5}Sb_{0.5}Se_3$**
Fermi wave-vector k_F (10^6 cm^{-1})	7.23	7.27	6.85	6.54	5.08
Dingle Temperature T_D (K)	25	27	22	26	23
Cyclotron mass m^* (m_0)	0.1523	0.1170	0.1174	0.1169	0.1161
quantum scattering time $[\tau_q = \hbar/(2\pi k_B T_D)]$ (fs)	47	44	54	46	52
Fermi velocity $[v_F = (\hbar k_F)/m^*]$ (10^5 ms^{-1})	5.49	7.19	6.75	6.47	5.06
2D carrier density $[n_s = (k_F^2)/4\pi]$ (10^{12} cm^{-2})	4.16	4.21	3.73	3.40	2.05
Surface mean free path $[l_s^{SdH} = v_F \tau_q]$ (nm)	25	31	35	29	26
surface mobility $[\mu_s^{SdH} = (e l_s^{SdH})/(\hbar k_F)]$ (cm^2/V.s)	541	659	804	690	785
β	0.5	0.6	0.6	0.875	-
g	2	2	2	2	2

Some of the fit parameters and their variation with Sb concentration are shown in Figure 4.10. The β value for x = 0.5 sample is not considered as the oscillations exhibit 3D character and thus are likely to arise from the quantization of the bulk 3D Fermi surface of Bi_2Se_3 as observed by Kazumo Eto et al. [18].

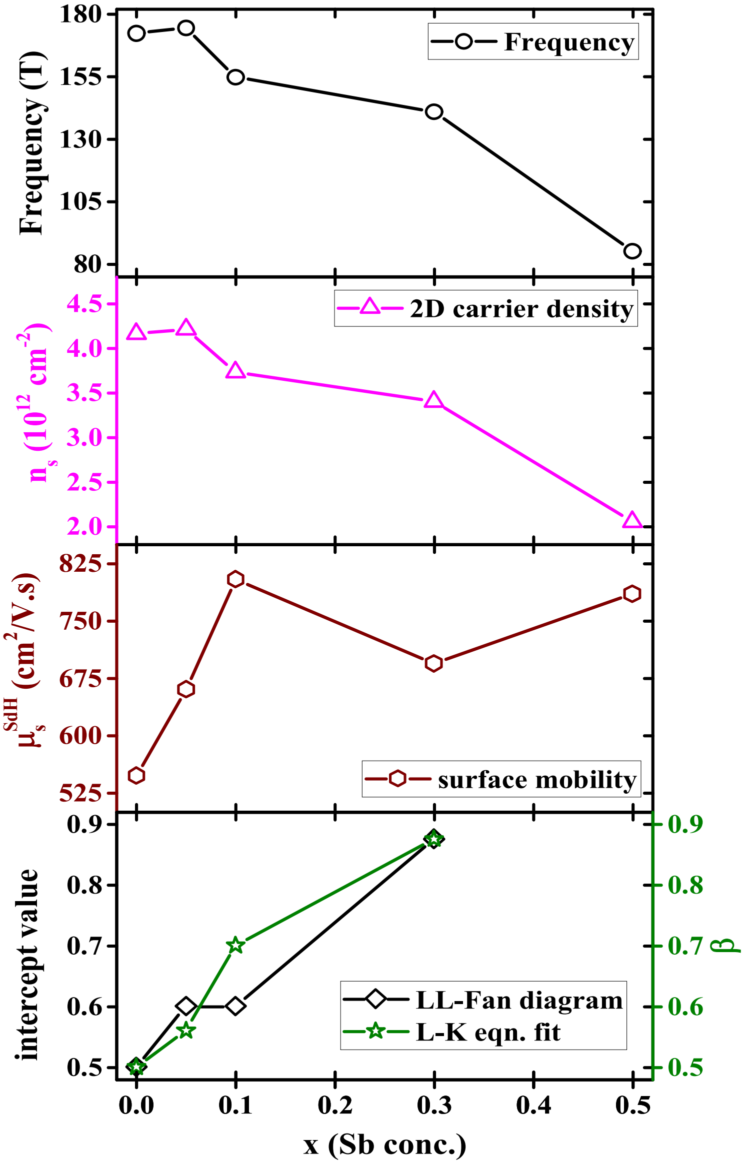

Figure 4.10 – Variation of Frequency (F), 2D carrier concentration (n_s), surface mobility (μ_s^{SdH}), β and the LL-fan diagram intercept as a function of Sb concentration in $Bi_{2-x}Sb_xSe_3$ single crystals.

The oscillation frequency in x = 0 sample is 172 T, which increases marginally to 174 T in x = 0.05 sample. For higher Sb concentrations viz. x = 0.1, 0.3 and 0.5 the frequency decreases. The Fermi wave-vector (k_F), defined as the radius of the 2D Fermi sphere, shows a marginal increase in value from the pristine x = 0 to x = 0.05 sample and then decreases for higher concentrations of Sb substitution. The reduction in its value implies a reduction in the cross-section of the Fermi level at E_F. The cyclotron mass of 0.1523 m_0 observed in x = 0 reduces to 0.1170 for x = 0.05 and nearly remains the same for the higher Sb substitutions. The values of Fermi-velocity (v_F) obtained from the values of k_F and m_0 shows a variation with Sb, which is similar to that seen for k_F. The magnitude of the 2D carrier density n_s shows a decreasing trend with increasing Sb substitution. The dingle temperature (T_D), quantum scattering time (τ_q) and surface mean free path (l_s^{SdH}) do not show any systematic variation with Sb substitution implying that Sb substitution in Bi_2Se_3 does not introduce any disorder into the system. These results are consistent with earlier calculations on the $Bi_{2-x}Sb_xSe_3$ system [2]. The surface mobility (μ_s^{SdH}) initially increases from 541 $cm^2/V.s$ in x = 0 to 804 $cm^2/V.s$ in x = 0.1, reduces to 690 $cm^2/V.s$ for x = 0.3 sample and increases again to 785 $cm^2/V.s$ in x = 0.5. The value of β for x = 0, 0.05, 0.1, 0.3 are 0.5, 0.56, 0.7, 0.875 respectively. The value of g obtained is 2 for all compositions.

The LL-fan diagram analysis [19] is then carried out to ascertain the origin of the oscillations viz. the relativistic Dirac fermions of the TSS that have linear dispersion or a trivial 2D electron gas (2DEG) that forms at the interface of semiconducting bulk/metallic surface as a consequence of equilibration between the bulk and surface Fermi levels and have a parabolic dispersion. As discussed in Chapter 3, the oscillations in resistivity are first converted to oscillations in conductivity using the relation $\sigma_{xx} = \rho_{xx}/(\rho_{xx}^2 + \rho_{xy}^2)$ following which the minima and maxima in conductivity oscillations are assigned integer and half-integer values respectively and plotted vs. $1/B_n$. The value of intercept at 0 T^{-1}, obtained from a linear fit to the data; with slope being fixed by the frequency of oscillations helps in determining the exact nature of the 2D oscillations – for TSS, the presence of a π Berry phase should lead to an intercept of 0.5 in the LL fan diagram. Figure 4.11 shows the LL-fan diagram analysis for the oscillations in H||c configuration in the compositions x = 0, 0.05, 0.01, and 0.3. The x = 0.5 sample is not considered for LL Fan diagram analysis as it presents oscillations of 3D character i.e. SdH oscillations in both H||c and H||ab configurations.

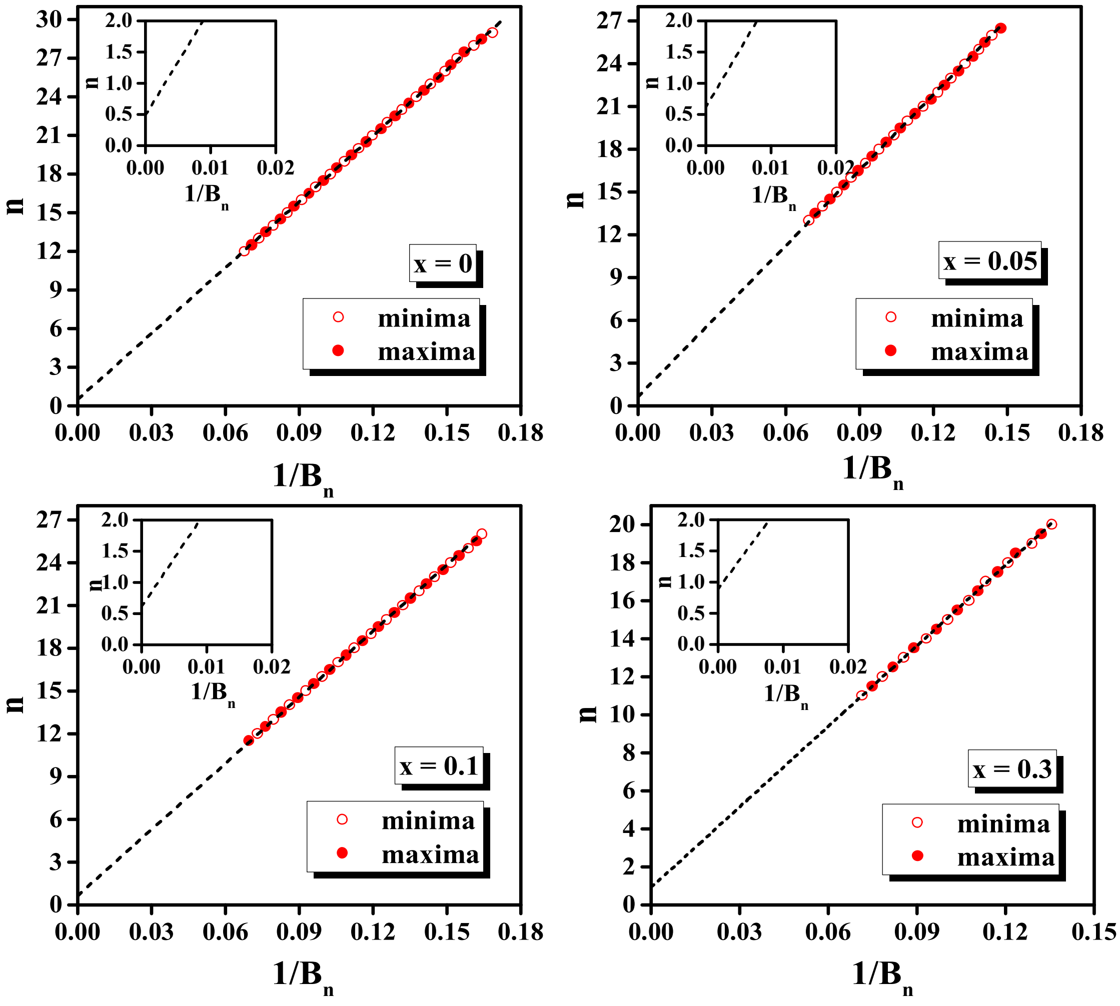

Figure 4.11 – LL-Fan diagram analysis ($1/B_n$ vs. n plot) for the oscillations in H||c configuration in the compositions x = 0, 0.05, 0.1, and 0.3. Minima and Maxima in conductivity are assigned integer and half integer values corresponding to the number of Landau levels inside the Fermi surface. The insets in each panel are the enlarged view of the same panels near 0 T^{-1}, to show the intercept.

It is observed that for the x = 0 sample the plot intercepts exactly at 0.5 and for the other compositions i.e. x = 0.05, 0.1 and 0.3, the intercepts are 0.6, 0.6 and 0.875 respectively.

4.6 Discussion

The Berry phase of 0.5, obtained from the LL-fan diagram analysis and a Fermi velocity value of $v_F \sim 5.49 \times 10^5$ ms^{-1} obtained from the L-K equation fit to the SdH oscillations which is in agreement with the Fermi velocity value of 5×10^5 ms^{-1} for the Dirac cone states in Bi_2Se_3 as observed from ARPES measurements reported earlier [20] gives strong evidence for the presence of TSS signatures in transport in the pristine x = 0 sample. In addition the single valued frequency value of 172 T corresponds to a large Fermi surface as expected for TSS. As discussed in Chapter 1, SdH oscillations from the surface states can be realized in TIs only when there is an upward band bending in the system where the surface Fermi level lies below the bulk Fermi level in energy. With the origin of oscillation in the pristine sample assigned to the TSS using Berry phase values from the LL fan diagram analysis (Figure 4.11) and v_F (Table 4.1); it is clear that the band-bending in our pristine Bi_2Se_3 system is upward. The 2D carrier density of $n_s \sim 4.12 \times 10^{12}$ cm^{-2}; estimated from the SdH analysis is also well within the theoretically calculated value of 5×10^{12} cm^{-2}, below which upward band bending is expected in pristine Bi_2Se_3 [21]. The introduction of Sb into the lattice is seen to give rise to two visible changes in the MR data viz. the change in frequency of oscillations (ref. Figure 4.10) and the change in LL Fan diagram intercept (ref. Figure 4.11). The reduction in frequency of oscillations could arise due to a reduction in the Fermi level, as a consequence of an upward shift of the Dirac Point (DP) due to reduction in the bulk band-gap. Such an upward shift of the DP in Sb substituted Bi_2Se_3 system has been predicted from band-structure calculations [2][3] and also been observed by ARPES in thin films of Sb substituted Bi_2Se_3 films grown by MBE technique [7]. The deviation in LL-Fan diagram intercept is marginal; from 0.5 for x = 0 to 0.6 for x = 0.05 & 0.1 samples, well within the spread observed in literature [19] and thus the SdH oscillations observed in x =

0.05 & 0.1 can still considered as the signature of TSS states. For x = 0.3, the intercept deviates significantly to a value of 0.875. This could imply that the observed SdH oscillations cannot be purely attributed to the TSS.

Alternatively, the 2D oscillations in x = 0.3 sample could arise from a trivial 2D state of 2DEG. This could arise due to the expected changes in Band gap with Sb substitution [2][3]. Since the band-gap is expected to reduce with Sb substitution, as mentioned earlier the DP shifts to higher energy with increase in Sb substitution [7]. It can then be conceived that the shift could result in the swapping of the Fermi level positions, such that in $E_F^{surface} > E_F^{bulk}$ leading to surface charge accumulation and hence formation of Quantum Well States (QWS). This QWS at the surface being inherently 2D in nature, can show SdH oscillations of 2D character, but have a parabolic dispersion such that their Berry phase deviates from 0.5. Thus the variation in the L-K equation parameters could then be reconciled with transport arising from TSS moving over to a topologically trivial 2DEG state. This cross-over made plausible with Sb substitution is illustrated schematically in Figure 4.12.

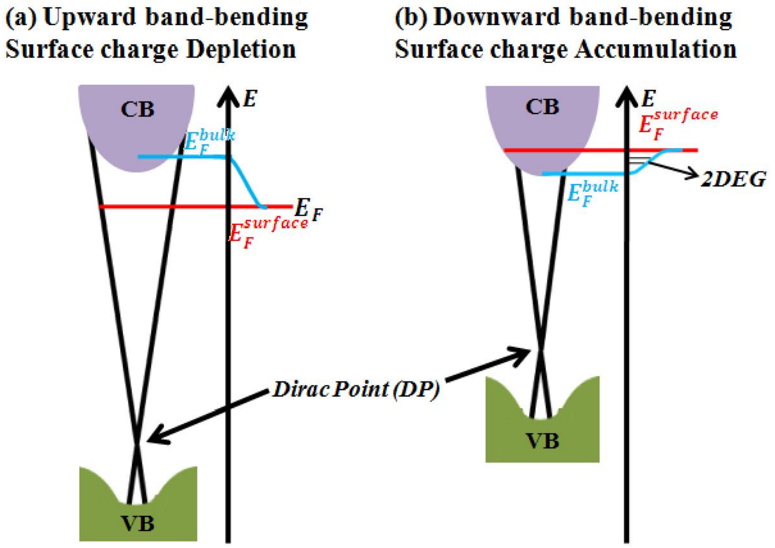

Figure 4.12 – Schematic diagram of Band structure in $Bi_{2-x}Sb_xSe_3$ showing **(a)** upward band bending and **(b)** downward band-bending and also reduction of bulk band gap [2][3] with Sb substitution. E_F^{Bulk} and $E_F^{Surface}$ are the bulk Fermi level and surface Fermi level respectively. DP corresponds to the Dirac Point and 2DEG corresponds to the trivial 2D electron gas that can form due to surface charge accumulation. The bulk Fermi level is pinned to the bottom of the conduction band as defined by the value of carrier concentration obtained from Hall Effect measurement [21]

4.7 Conclusions

Synchrotron measurements suggests that the $Bi_{2-x}Sb_xSe_3$ (x = 0, 0.05, 0.1, 0.3, 0.5) crystal system is highly single phase only for low Sb substitution concentration i.e. ≤ 15%. The resistivity increases with increase in Sb substitution which is supported by the observed reduction in charge carrier density from Hall Effect measurements. From analysis of the SdH oscillations obtained from magneto-resistance measurements we surmise that the signatures of the TSS are observed for Sb concentration of upto x = 0.1, whereas for x = 0.3 the trivial 2DEG masks the transport from TSS. Thus we can conclude that a reduction in the bulk band-gap can shift the DP in such a manner that the positions of the Fermi levels interchange leading to a transport being dominated by the electronic structure of the bulk/surface interface which can mask signatures from TSS in transport measurements.

References

[1] Haijun Zhang, Chao-Xing Liu, Xiao-Liang Qi, Xi Dai, Zhong Fang & Shou-Cheng Zhang, *Nature Physics* **5** (2009) 438

[2] Jianpeng Liu & David Vanderbilt, *Phys. Rev. B* **88** (2013) 224202

[3] L. B. Abdalla, Jose E Padilha, T. M. Schmidt, R H Miwa & A. Fazzio, *J. Phys.: Condens. Matter* **27** (2015) 255501

[4] V. G. Kuznetsov, K. K. Palkina, and A. A. Reshchikova, *Inorg. Mater.* **4** (1968) 670

[5] Č. Drašar, I. Klichová, L. Koudelka, P. Lošták, *Cryst. Res. Technol.* **31** (1996) 805

[6] V. A. Kulbachinskii, N. Miura, H. Nakagawa, H. Arimoto, T. Ikaida, P. Lostak & C. Drasar, *Phys. Rev. B* **59** (1999) 15733

[7] Yi Zhang, Cui-Zu Chang, Ke He, Li-Li Wang, Xi Chen, Jin-Feng Jia, Xu-Cun Ma & Qi-Kun Xue, *Appl. Phys. Lett.* **97** (2010) 194102

[8] W. Kraus & G. Nolze *J. Appl. Cryst.* **29** (1996) 301

[9] Gene E. Ice and Judy W.L. Pang, *Mater. Charact.* **60** (2009) 1191

[10] B. D. Cullity, *Elements of X-Ray Diffraction* (Addison-Wesley Publishing Company, Inc., Massachusetts) 1956 p. 246

[11] C. S. Sundar, *Bull. Mater. Sci.* **17**, (1994) 1215

[12] D. West, Y. Y. Sun, Han Wang, Junhyeok Bang, & S. B. Zhang, *Phys. Rev. B* **86** (2012) 121201

[13] L. Xue, P. Zhou, C. X. Zhang, C. Y. He, G. L. Hao, L. Z. Sun & J. X. Zhong, *AIP* Advances **3** (2013) 052105

[14] T. Plencháček, J. Navrátil and J. Horák, *Journal of Solid State Chemistry* **165** (2002) 35

[15] A. Van Vechten, *J. Electrochem. Soc.* **122** (1975) 419

[16] A. A. Taskin, Kouji Segawa &Yoichi Ando, *Phys. Rev. B* **82** (2010) 121302(R)

[17] D. Schoenberg, *Magnetic Oscillations in metals* (Cambridge University Press, London) 1984 p. 66

[18] Kazuma Eto, Zhi Ren, A. A. Taskin, Kouji Segawa & Yoichi Ando, *Phys. Rev. B* **81** (2010) 195309

[19] Y. Ando, *J. Phys. Soc. Jpn.* **82** (2013) 102001

[20] Y. Xia, D. Qian, D. Hsieh, L. Wray, A. Pal, H. Lin, A. Bansil, D. Grauer, Y. S. Hor, R. J. Cava & M. Z. Hasan, *Nature Physics* **5**, (2009) 398

[21] Matthew Brahlek, Nikesh Koirala, Namrata Bansal & Seongshik Oh, *Solid State Communications* **54** (2015) 215

CHAPTER 5

Magneto-transport studies on Te substituted disordered Bi_2Se_3 single crystals

Both Bi_2Se_3 and Bi_2Te_3 being Topological Insulators (TIs) [1] with similar structures, naturally evoked an interest to investigate the series of intermediates $Bi_2Se_{3-x}Te_x$ compounds for the presence of Dirac cone states. Xu et al. [2] were the first to predict from ab-initio calculations and confirm by ARPES experiments the presence of a single Dirac cone in Bi_2SeTe_2 (BTS). This was followed by a report from Ren et al. [3] on the synthesis of a bulk insulating BTS crystal with a low temperature resistivity value as high as 1 Ω-cm, which showed Shubnikov de Haas (SdH) oscillations from the Topological Surface States in magneto-transport measurements. Xiong et al. [4] in another report showed similar results with the low temperature resistivity of the bulk reaching ~ 6 Ω-cm. Wang et al. [5] in their report confirmed that along with BTS, another intermediate Bi_2Se_2Te (BST) is also a TI, based on observed parity inversion at the Γ point in band structure calculations. Highly insulating crystals (420 Ω at 4.2 K) of BST were synthesized by Bao et al. [6] and signatures of TSS viz. SdH oscillations and Weak Antilocalization (WAL) were observed.

While most of the studies in this ternary TI system viz. $Bi_2Se_{3-x}Te_x$, have focussed on synthesis of individual compounds which are highly insulating in the bulk, there exists no comprehensive study on the behaviour of magneto-transport across the $Bi_2Se_{3-x}Te_x$ series of TI single crystals. With recent band structure calculations suggesting that the introduction of large size defects viz., stacking faults can shift the Dirac point of the topological insulator, thereby favouring Fermi level to lie in surface states and in-turn affect the relative contribution of surface states and bulk state towards the transport property [7]; it would be interesting to look at the evolution of magneto-transport behaviour with introduction of Te into the Bi_2Se_3 lattice. Since the emphasis of this chapter is the influence of strong disorder on magneto-transport investigations, we use for synthesis of the samples, the procedure employed for BS137 mentioned in Chapter 3 viz., very fast cooling rate. It may be recalled that this sample was seen to be strongly disordered and it had much larger lattice parameters in comparison to BS1 (cf. Figure 3.9) and displayed SdH oscillations that had contribution from both the TSS and the trivial 2DEG.

5.1 Synthesis and X-Ray diffraction

Single crystals of $Bi_2Se_{3-x}Te_x$ (x = 0, 1, 1.8 and 2) were grown from stoichiometric mixtures of high purity Bi, Se and Te powders. The mixtures were melted at 850°C for 6 hours in an evacuated sealed quartz tube environment, followed by rapid cooling at the rate of 137°C/hour. This step of rapid cooling is drastically different from the other reports in the literature and was intended to introduce strong disorder in the system [3][4][6][8][9]. Synchrotron X-ray diffraction measurements were carried out on the powdered single crystal samples at room temperature, at the beam line BL-12 of the Indus II synchrotron at RRCAT – Indore, India, using 12.6 keV X-rays. Figure 5.1 shows the powder diffraction patterns on the powdered single crystals, for samples with nominal compositions of Bi_2Se_3 (BS), Bi_2Se_2Te (BST), $Bi_2Se_{1.2}Te_{1.8}$ and Bi_2SeTe_2 (BTS). All the diffraction peaks could be indexed to rhombohedral $R\bar{3}m$ structure. The *a* and *c* axis lattice parameters were obtained by analyzing the powder diffraction data using the refinement routine in *PowderCell* [10]. Figure 5.2(a) shows the variation of the lattice constants as a function of Te substitution in the Bi_2Se_3 system. It is observed that both the *a* and *c* increase with increase in Te concentration. The unit cell volume as a function of Te concentration is shown in Figure 5.2(b). The progressive increase in unit cell volume substantiates the incorporation of the bigger Te atom at the Se position in the lattice. The values agree with earlier reports on the system [11].

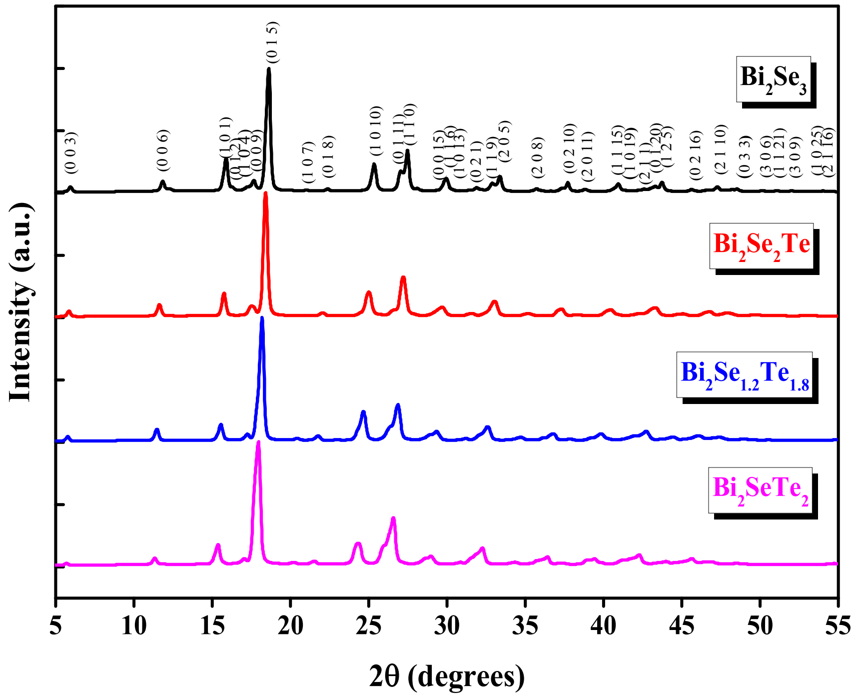

Figure 5.1 – Powder diffraction patterns of $Bi_2Se_{3-x}Te_x$ samples normalised to the highest observed peak intensity. The graphs has been shifted vertically for clarity, the indices of the rhombohedral structure are shown for Bi_2Se_3.

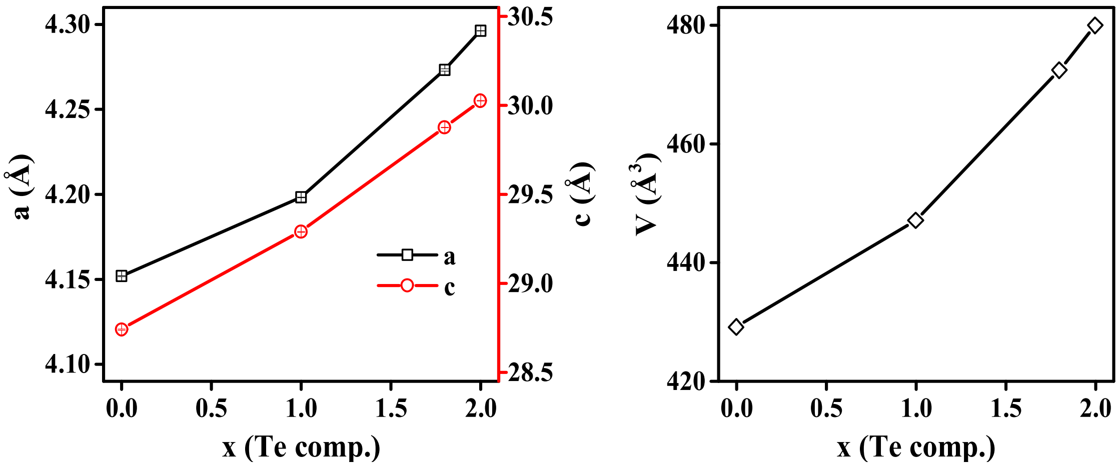

Figure 5.2 – **(a)** variation of *a* and *c* lattice parameters of $Bi_2Se_{3-x}Te_x$ crystals as a function of Te concentration; **(b)** variation of unit cell volume as a function of Te concentration

Figure 5.3(a) shows the enlarged view of the (015) diffraction peak for the various compositions. It is observed that the peak broadens with increasing Te substitution, which is indicative of increasing extended disorder in the sample [8][12]. This is also reflected in Laue diffraction patterns acquired in back scattering geometry as observed in Figure 5.3(b). A clear six-fold symmetry with a line of close spots that is observed in the pristine crystals indicating good long range order is seen to get distorted with increasing Te substitution and become less distinctive, indicative of the increasing crystalline stacking disorder in the samples with large Te substitution.

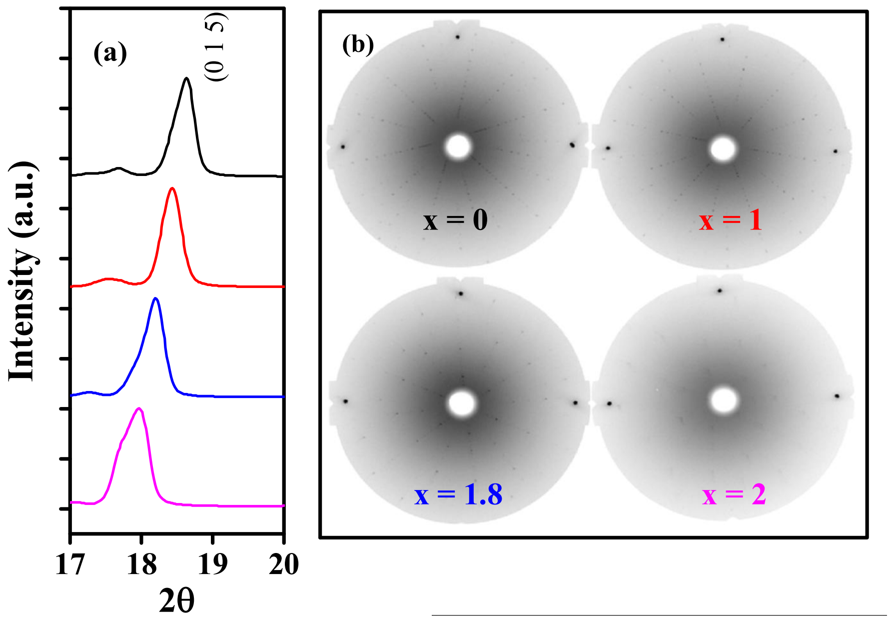

Figure 5.3 – (a) broadening of (015) peak upon Te substitution **(b)** Laue diffraction patterns in the backward scattering geometry shows the six fold symmetry with distinct spot in Se rich samples (x = 0, 1) and the gradual degradation of crystalline order inferred from the distortion and elongation of spots along the radial direction upon Te substitution (x = 1.8, 2).

5.2 Resistivity

Figure 5.4 (a)-(d) shows the resistivity (ρ) versus temperature (T) behaviour of $Bi_2Se_{3-x}Te_x$ (x = 0, 1, 1.8 and 2) samples. It is evident from the figure that the pristine Bi_2Se_3 crystal shows a metallic behaviour with a discernible saturation in resistivity below 30 K. Such a saturation tendency at low temperature has been reported to stem from the excess carriers from Se vacancies in the sample [9][13]. It is also observed that in $Bi_2Se_{1.2}Te_{1.8}$ and BTS samples, the positive temperature coefficient of resistivity at high temperatures changes to a negative temperature co-efficient as the temperature is lowered. The observed temperature dependence of resistivity and its order of magnitude for BTS are different from that reported by Ren et al. [3][9], where resistivity changed by two orders of magnitude and clearly showed activation behaviour at high temperature and a 3D variable range hopping (VRH) at low temperature suggesting that the carriers in the system are highly localised as observed from the very low value of their bulk mobility of 11cm^2/Vs. Figure 5.4(e) shows the variation of resistivity at 300 K and 4.2 K as a function of Te concentration. The resistivity values are observed to increase with increase in Te substitution in the Bi_2Se_3 system, a behaviour that could arise due to a reduction in the carrier concentration and/or a suppression of the carrier mobility.

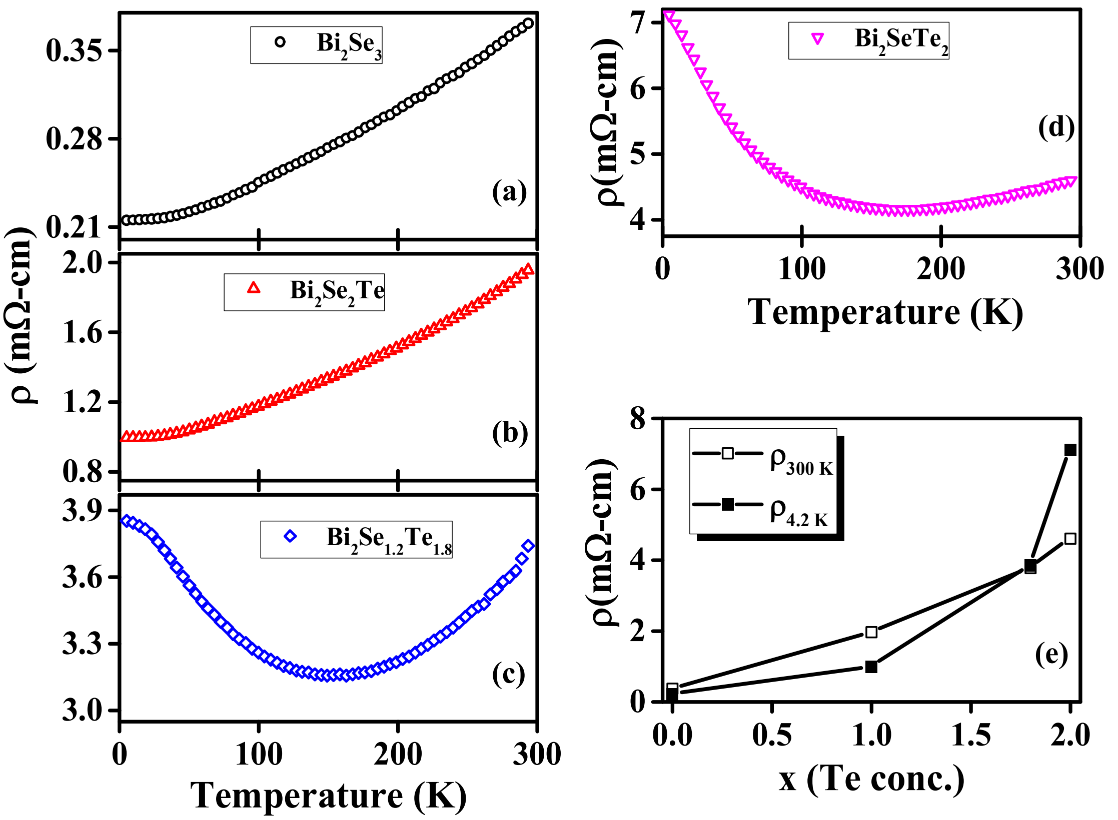

Figure 5.4 – (a)-(d) The variation of resistivity as a function of temperature of $Bi_2Se_{3-x}Te_x$ samples. A metal to insulator type of behaviour is evident upon Te substitution; **(e)** the variation of resistivity as a function of Te substitution at 300 K (open symbol) and 4.2 K (closed symbol)

To understand the origin of the negative temperature co-efficient of resistivity at low temperatures in $Bi_2Se_{1.2}Te_{1.8}$ and BTS sample, the low temperature data is fitted to known models such as Mott-VRH (shown in Figure 5.5(a)) and Arrhenius (shown in Figure 5.5(b)). The activation energy from the Arrhenius fit to BTS sample is found to be 1.5 meV. However as the temperature range for fits are too narrow, we are not able to present a conclusive argument to unequivocally establish the mechanism of transport (VRH/Arrhenius) from the present data. In order to understand the reason for the change in resistivity behaviour with Te addition, Hall Effect measurements are carried out in the samples.

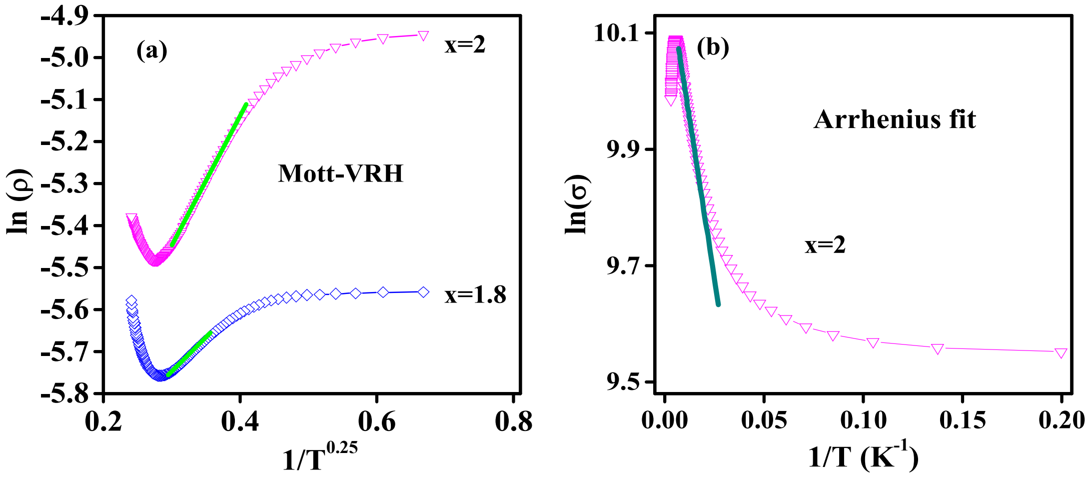

Figure 5.5 – (a) VRH fit for high Te concentration (x = 1.8, 2) samples **(b)** Arrhenius fit for x = 2 sample.

5.3 Hall Effect measurement

Figure 5.6 shows the Hall Effect measurement data on the $Bi_2Se_{3-x}Te_x$ samples. It is observed that in the pristine Bi_2Se_3 sample, Hall resistance is linear with magnetic field which evolves into a non-linear response in the higher Te substituted samples $Bi_2Se_{1.2}Te_{1.8}$ and BTS. The non-linearity in Hall data is more prominent in BTS sample. The linear behaviour in BS and BST suggest that the transport is dominated by a single type of carrier. The non-linear behaviour in $Bi_2Se_{1.2}Te_{1.8}$ and BTS suggests the presence of transport from two or more types of carriers in the system [3]. Such non-linear behaviour has been observed in similar TI samples and is reported to be due to the parallel contribution of both surface and bulk carrier to the transport [3][9][13][14].

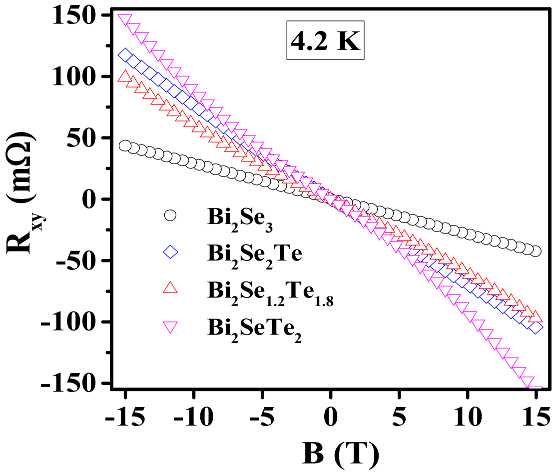

Figure 5.6 – Hall resistance as a function of Te concentration in $Bi_2Se_{3-x}Te_x$ series. With increase in Te concentration the R_{xy} plots become non-linear.

To look at the evolution of the non-linear behaviour of Hall resistance with temperature, Hall Effect measurements are carried out at various temperatures for the $Bi_2Se_{3-x}Te_x$ and the data are plotted in Figure 5.7(a)-(d). It is observed that for Bi_2Se_3 and BST samples, the Hall data is linear as a function of magnetic field and is nearly temperature independent, implying that the carrier density is unaffected by temperature. However in the $Bi_2Se_{1.2}Te_{1.8}$ and BTS samples the non-linear behaviour vanishes and a linear behaviour takes over at a temperature of 100 K.

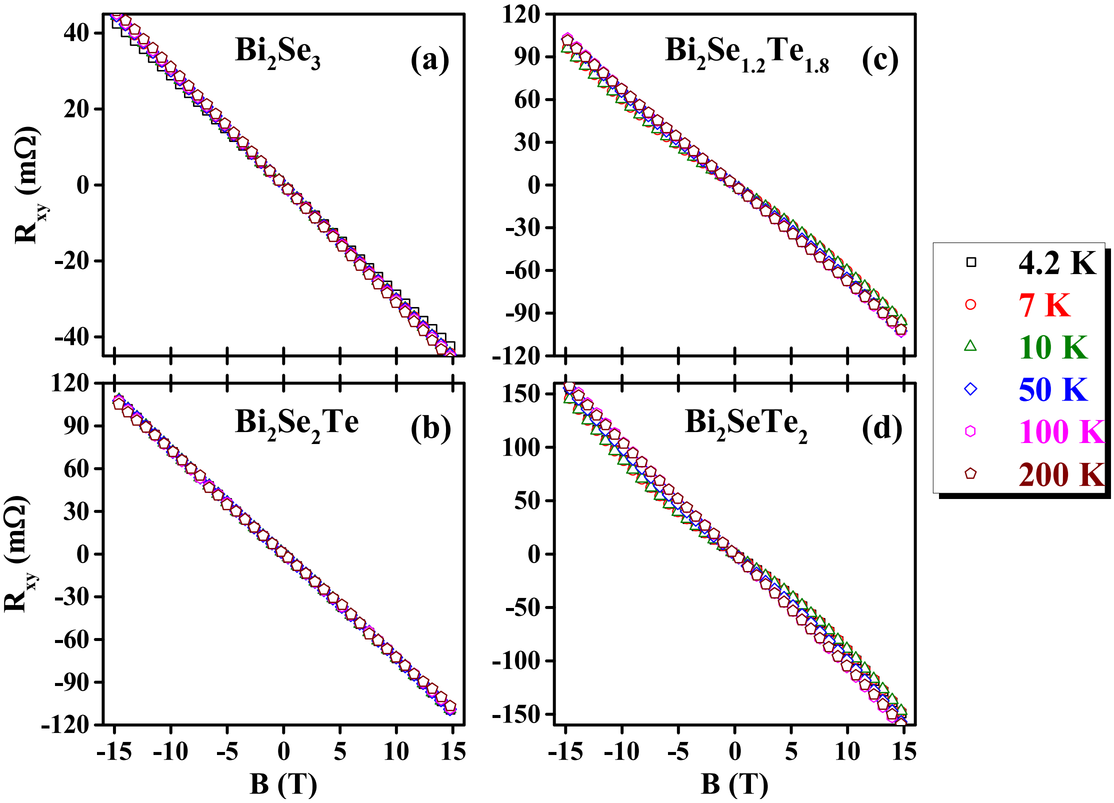

Figure 5.7 – The variation of Hall resistance as a function of magnetic field at various temperatures in Bi_2Se_3 and Te doped samples showing a linear behaviour for low Te concentration viz., **(a)** Bi_2Se_3 (BS); **(b)** Bi_2Se_2Te; and a non-linear behaviour at low T for higher Te concentration viz., **(c)** Bi_2SeTe_2; **(d)** Bi_2Te_3.

From the resistivity and Hall Effect measurements, the carrier concentration (n) and the mobility (μ) of carriers are evaluated, both, as a function of temperature in each compound and also as a function of Te concentration. Further, as this system viz., $Bi_2Se_{3-x}Te_x$ is seen to have disorder as suggested from Laue patterns, we try to quantify the disorder by using the Ioffe-Regel criterion. According to the Ioffe-Regel criterion, the metallic behaviour of a system is limited by the increase in the disorder in the system such that metallic transport would become impossible once the mean free path of the electrons reduce to values less than the inter-atomic spacing. The Ioffe-Regel [15] parameter, given by $k_f l = (3\pi n)^{2/3}\left[\frac{\hbar\mu}{e}\right]$ where k_f is the Fermi wave-vector and l is the electron mean free path, is thus evaluated for the current system. The variation of carrier density (n), mobility (μ) and $k_f l$ as a function of Te content at 4.2 K are shown in Figure 5.8(a)-(c) and their variation as function of temperature are shown in Figure 5.8(d)-(f).

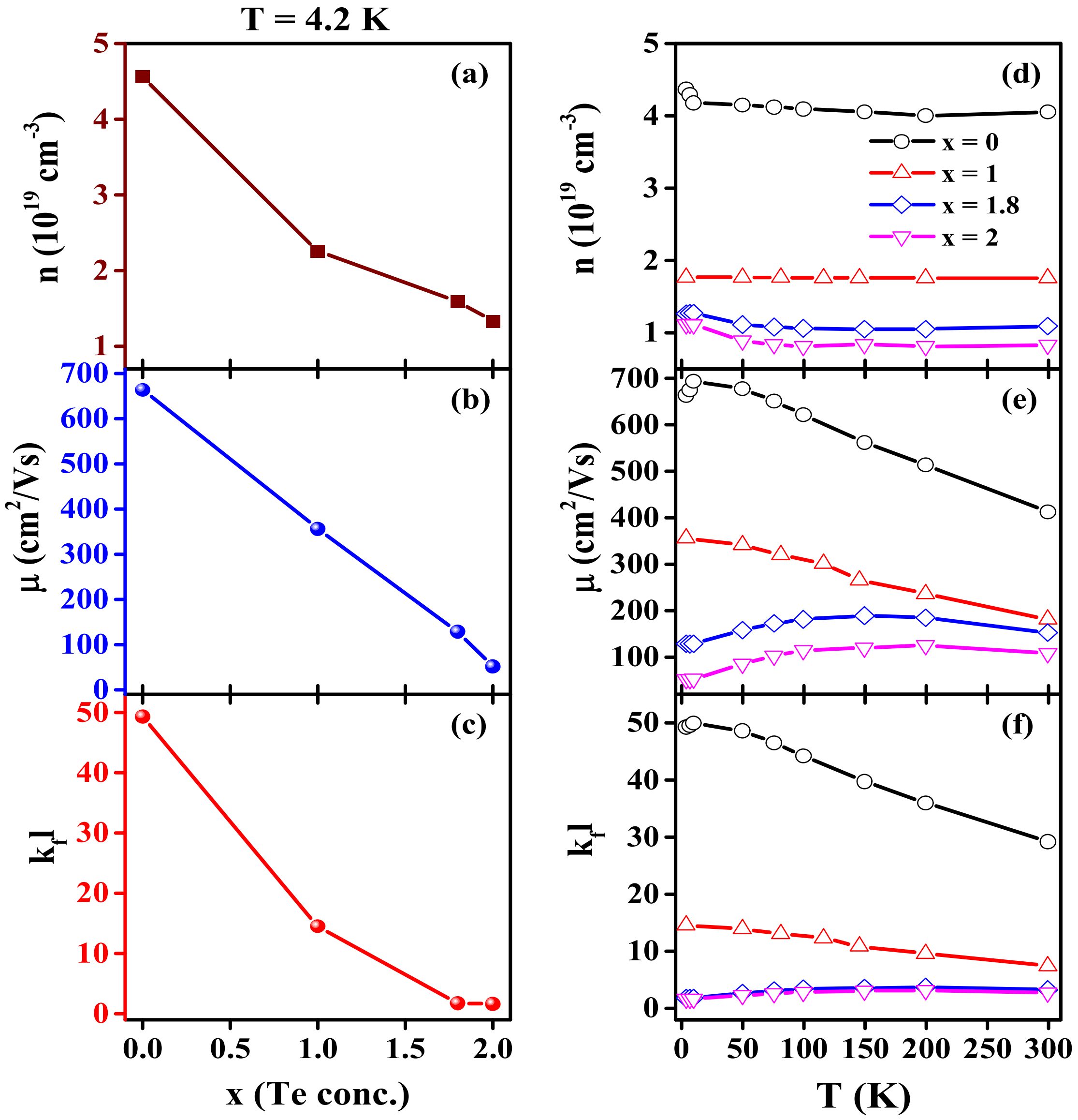

Figure 5.8 – Te concentration dependence of **(a)** carrier concentration (n), **(b)** mobility (μ), **(c)** the Ioffe-Regel parameter ($k_f l$); Temperature dependence of **(d)** carrier concentration (n), **(e)** mobility (μ) and **(f)** the Ioffe-Regel parameter ($k_f l$), as obtained from the analysis of Hall and resistivity data.

From Figure 5.8(a) we see that the carrier concentration decreases with increase in Te content, however the carrier concentrations for each individual sample do not show any temperature dependence (Figure 5.8(d)). From Figure 5.8(b) we see that the Hall mobility decreases with increase in Te concentration. This decrease in mobility with increase in Te concentration could imply a decrease in scattering time τ, and hence can imply an increase in disorder with increase in Te. Figure 5.8(e) shows the variation of mobility as a function of temperature in individual Te substituted samples. It is observed that the mobility increases with decrease in temperature in the low Te samples (x = 0, 1). The degree of increase in mobility with decrease in temperature, slows down with increase in Te content, whereas for large Te content (x = 1.8, 2) the mobility decreases with decrease in temperature. From Figure 5.8(c) we see that the $k_f l$ values obtained from the resistivity and Hall data, decrease with Te content and become close to one in the high Te concentration samples, particularly at low temperatures. This implies that the electronic disorder induced in the high concentration Te samples leads to the localisation of carriers and could account for the appearance of upturn in $\rho(T)$ of high Te doped $Bi_2Se_{3-x}Te_x$ (x = 1.8, 2) as seen in Figure 5.4(c)-(d)

5.4 Magneto-resistance

In order to see the effect of the drastic change in mobility upon Te substitution on magneto-transport, magneto-resistance ($R_{xx}(B)-R_{xx}(0)$) measurement were carried out on $Bi_2Se_{3-x}Te_x$ (x= 0, 1, 1.8 and 2) samples at 4.2 K in the field range of -15 T to 15 T (shown in Figure 5.9(a)-(d)).

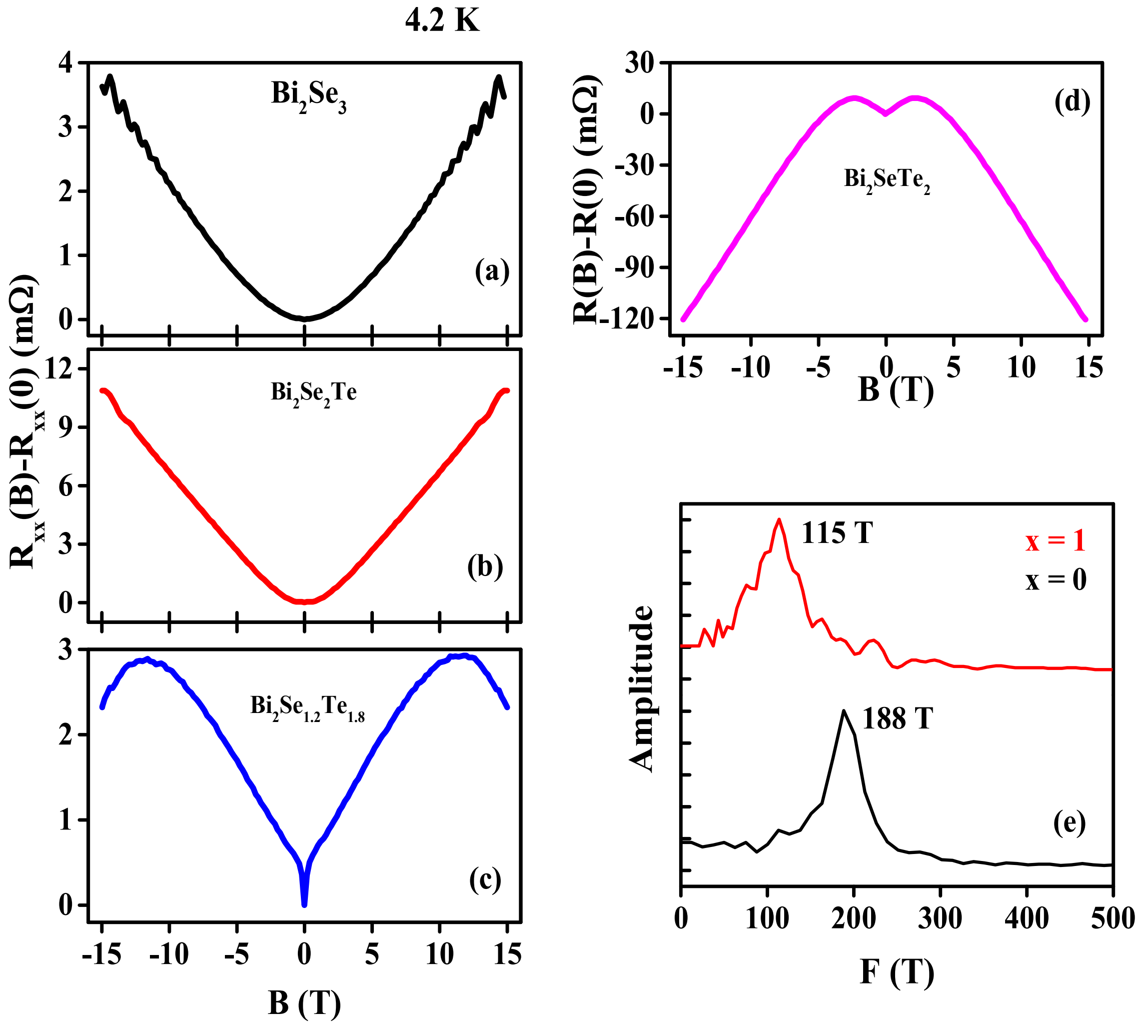

Figure 5.9 – (a)-(d) Variation of magneto-resistance ($R_{xx}(B)-R_{xx}(0)$) with magnetic field measured with magnetic field parallel to the c-axis of the crystal at 4.2 K, in the $Bi_2Se_{3-x}Te_x$ series; **(e)** Frequency of SdH oscillations in BS and BST from the FFT on the oscillatory component.

It is observed that both pristine Bi_2Se_3 and the low Te concentration BST sample show a positive MR with discernible Shubnikov-de Haas (SdH) oscillations for B > 7 T. The frequency of oscillations obtained from a Fourier transform on the oscillatory component of MR in BS and BST are shown in Figure 5.9(e). The oscillation frequency is found to decrease from 188 T for BS to 115 T for BST. This implies a contraction of the Fermi surface with Te substitution [16]. It is also noted from Figure 5.9(e) that the oscillations are not at a single frequency for BST unlike that seen in the pristine BS. This suggests a lack of coherence of the Landau levels due to disorder induced in the Te substituted samples. The SdH oscillations are observed to vanish for the $Bi_2Se_{1.8}Te_{1.2}$ and BTS samples (see Figure 5.9(c)-(d)). Interestingly the MR in these samples shows a qualitatively different behaviour from that of BS and BST viz., the MR shows a low field cusp behaviour that is associated with Weak anti-localisation (WAL) [17]. It is also evident from Figure 5.9(c) that the MR vs. Magnetic field of $x = 1.8$ shows a positive slope upto ~10 T and changes to a negative slope for $B > 10$ T. The $x = 2$ sample shown in Figure 5.9(d) shows a more pronounced positive cusp for $-2T < B < 2$ T, reaching a maximum at 2 T, and then starts to decrease on increasing the field, similar to Weak Localisation (WL). Thus as a function of Te substitution Figure 5.9(a)-(d) displays that there is a crossover from Weak Antilocalization (WAL) to Weak Localization (WL) behaviour.

It has been shown from earlier studies [6][17] that the cusp like positive magneto-resistance behaviour attributed to WAL gives way to negative magneto-resistance on account of opening of band gap at the Dirac point due to magnetic impurity [18], or due to hybridisation of the bottom and top surface states in very thin samples [16][19]. As the samples in the present study are neither in thin film form nor have any magnetic impurities, an alternative interpretation of the WAL-WL crossover needs to be sought. It is interesting to note that the WAL phenomenon is observed in samples that exhibit non-linear Hall resistance as a function of magnetic field viz. $Bi_2Se_{1.2}Te_{1.8}$ and BTS (cf. Figure 5.7(c)-(d)). As we have seen in the temperature dependence of Hall resistance that the non-linear behaviour at low temperatures changes to linear behaviour above 100 K, it of interest to study how the MR evolves across the non-linear to linear transition in temperature.

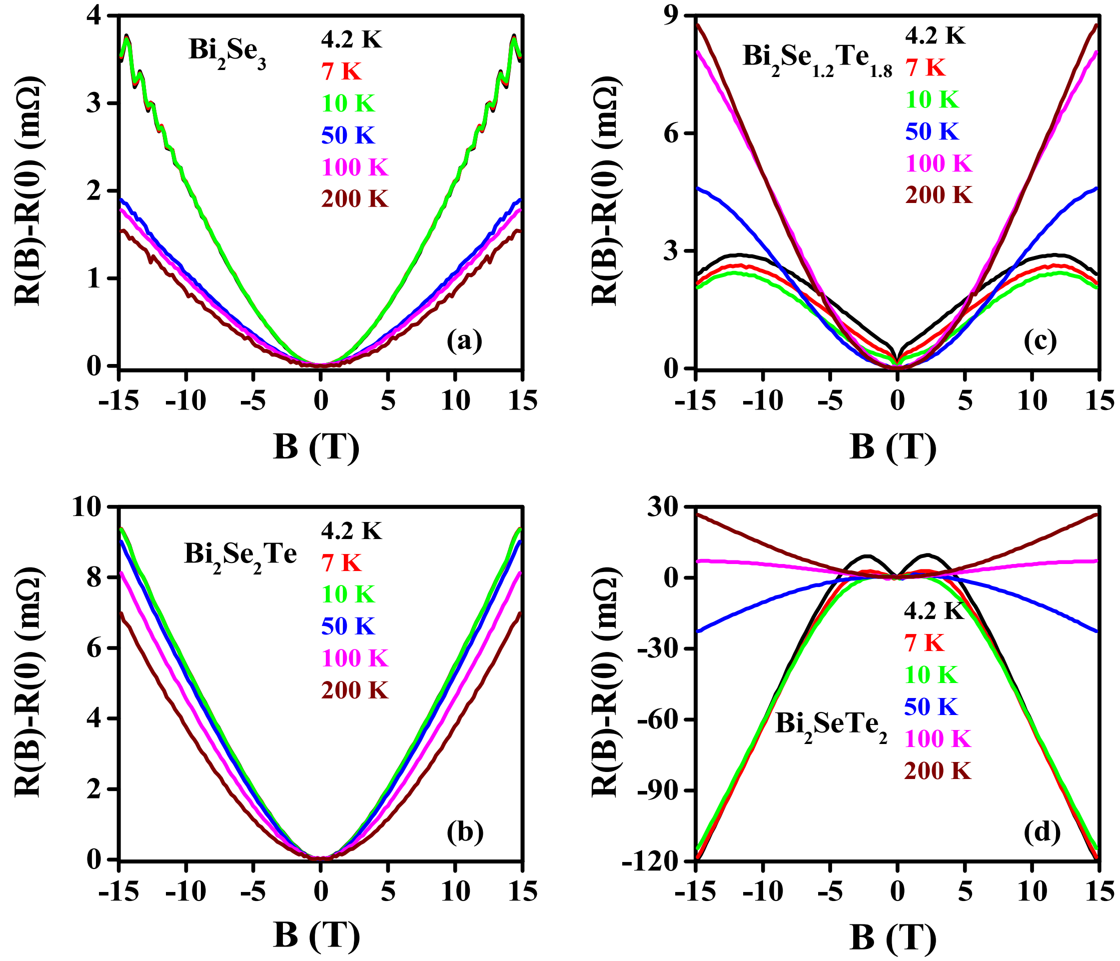

Figure 5.10 – The variation of magneto-resistance as a function of magnetic field at various temperatures in **(a)** BS, **(b)** BST **(c)** $Bi_2Se_{1.2}Te_{1.8}$ and **(d)** BTS.

Figure 5.10 (a)-(d) show the temperature evolution of the MR for all the four samples. For the pristine BS sample, the oscillatory magneto-resistance behaviour is seen for temperatures upto 10 K and gets suppressed as the temperature is increased. The oscillatory part of MR rides on a linear high field MR behaviour, whose magnitude decreases with increase in temperature. In the case of BST, the MR behaviour is qualitatively similar to Bi_2Se_3, albeit with a substantially larger MR. In the $Bi_2Se_{1.2}Te_{1.8}$ sample, the negative slope seen at B > 10 T vanishes when temperature exceeds 10 K. In the BTS sample, a systematic transition upon increasing temperature is seen. From 4.2 K to 10 K the WAL cusp decreases and vanishes at 50 K. On further increasing the temperature i.e. T > 50 K, a transition to positive MR is observed. This negative to positive MR transition occurs at the same temperature when the Hall data (shown in Figures 5.7(c)-(d)) also shows a transformation from a non-linear behaviour to a linear behaviour on increasing T. Since both WAL and WL are quantum phenomena they are not observed at higher temperatures, where a regular positive magneto-resistance is seen.

5.5 Discussion

We know from the Landau Level fan diagram analysis of the SdH oscillations in Bi_2Se_3 (in Chapter 3), that both TSS and a conventional 2DEG that forms because of band-bending contribute to the transport in Bi_2Se_3 sample BS137/BS. The mobility of the carriers are high in BS and BST and SdH oscillations are observed in MR. The addition of Te introduces an electronic disorder in $Bi_2Se_{3-x}Te_x$ systems, which in turn reduces their electronic mobility and the mean free path (see Figure 5.8). The decrease in the mean free path (*l*) makes it conducive for the condition $l_\varphi > l$ (where $l_\varphi > l$ is the phase coherence length) to be met, leading to the quantum corrections to the transport, viz. the WAL behaviour that points to the involvement of topological surface state in the transport behaviour. With the increase of magnetic field, this WAL feature is seen to transform to the WL behaviour – as has been observed in other experiments [16][20]. The significant result from the present experiments is that there is a change from SdH to WAL behaviour with Te doping, which can be attributed to the electronic disorder, arising from large defects, like stacking faults. Since the presence of large defects such as stacking faults and small angle grain boundaries can shift the Dirac point and therefore the Fermi level, the contribution to the total electrical transport from the topological surface states can be altered [7]. Similar results have observed recently in $BiSbTe_3$ samples where an SdH to WAL to WL transition has been seen [21].

5.6 Conclusion

From magneto-transport studies on $Bi_2Se_{3-x}Te_x$ (x = 0, 1, 1.8, 2) single crystals, it is seen that SdH oscillation attributed to both the TSS and the 2DEG gas are observed in the Bi_2Se_3 and low Te substituted Bi_2Se_2Te samples. In the higher Te concentration samples i.e. x = 1, 2, an interesting feature exhibiting evolution of WAL behaviour is observed which can be due to increase of underlying strong disorder as observed from the values of mobility. This WAL behaviour is accompanied by the change in character of the Hall slope from linear to non-linear. This suggests an increased contribution of TSS in transport. The WAL to WL transition observed with increase of magnetic field could be due to the 2D electron gas state that forms due to band bending in the disordered Te samples.

References

[1] Haijun Zhang, Chao-Xing Liu, Xiao-Liang Qi, Xi Dai, Zhong Fang & Shou-Cheng Zhang, *Nature Physics* **5** (2009) 438

[2] Su-Yang Xu, L. A. Wray, Y. Xia, R. Shankar, A. Petersen, A. Fedorov, H. Lin, A. Bansil, Y. S. Hor, D. Grauer, R. J. Cava & M. Z. Hasan, *arxiv:1007.5111*

[3] Z. Ren, A.A. Taskin, S. Sasaki, K. Segawa & Y. Ando, *Phys. Rev. B* **82** (2010) 241306

[4] Jun Xiong, A. C. Petersen, Dongxia Qu, Y. S. Hor, R. J. Cava & N. P. Ong, *Physica E* **44** (2012) 917

[5] Lin-Lin Wang & Duane D. Johnson, *Phys. Rev. B* **83** (2011) 241309(R)

[6] Lihong Bao, Liang He, Nicholas Meyer,Xufeng Kou, Peng Zhang, Zhi-gang Chen, Alexei V. Fedorov, Jin Zou, Trevor M. Riedemann, Thomas A. Lograsso, Kang L. Wang, Gary Tuttle & Faxian Xiu, *Scientific Reports* **2** (2012) 726

[7] L. Seixas, L.B. Abdalla, T.M. Schmidt, A. Fazzio & R.H. Miwa, *J. Appl. Phys.* **113** (2013) 023705

[8] S. Jia, H. Ji, E. Climent-Pascual, M.K. Fuccillo, M.E. Charles, J. Xiong, N. P. Ong & R. J. Cava *Phys. Rev. B* **84** (2011) 235206

[9] Z. Ren, A. A. Taskin, S. Sasaki, K. Segawa & Y. Ando, *Phys. Rev. B* **84** (2011) 165311

[10] W. Kraus & G. Nolze, *J. Appl. Cryst.* **29** (1996) 301

[11] S. Nakajima, *Journal of Physics and Chemistry of Solids* **24** (1963) 479

[12] K. Park, Y. Nomura, R. Arita, A. Llobet & D. Louca, *Phys. Rev. B* **88** (2013) 224108

[13] Z. Ren, A. A. Taskin, S. Sasaki, K. Segawa & Y. Ando, *Phys. Rev B* **84** (2011) 075316

[14] A. A. Taskin, Z. Ren, S. Sasaki, K. Segawa & Y. Ando, *Phys. Rev. Lett.* **107** (2011) 016801

[15] Matthew Brahlek, Nikesh Koirala, Namrata Bansal & Seongshik Oh, *Solid State Communications* **54** (2015) 215

[16] A. A. Taskin, S. Sasaki, K. Segawa & Y. Ando, *Phys. Rev. Lett.* **109** (2012) 066803

[17] Hai-Zhou Lu & Shun-Qing Shen-Z, *Phys. Rev. B* **84** (2011) 125138

[18] Minhao Liu, Jinsong Zhang, Cui-Zu Chang, Zuocheng Zhang, Xiao Feng, Kang Li, Ke He, Li-li Wang, Xi Chen, Xi Dai, Zhong Fang, Qi-Kun Xue, Xucun Ma, & Yayu Wang, *Phys. Rev. Lett.* **108** (212) 036805

[19] M. Lang, L. He, X. Kou, P. Upadhyaya, Y. Fan, H. Chu, Y. Jiang, J. H. Bardarson, W. Jiang, E. S. Choi, Y. Wang, N.-C. Yeh & J. Moore, K.L. Wang, *Nano Letters* **13** (2012) 48

[20] K. Banerjee, J. Son, P. Deorani, P. Ren, L. Wang & H. Yang, *Phys. Rev. B* **90** (2014) 235427

[21] X.-L.W. Fei-Xiang Xiang & Shi-Xue Dou, *arXiv:1404.7572*

CHAPTER 6

High Pressure transport studies on single crystal TI system $Bi_2Se_{3-x}Te_x$

High pressure has been a valuable tool in condensed matter research. It provides a platform wherein the ground state properties of the material to be studied can be tuned without resorting to chemical procedures such as substitution or doping and thereby retaining the original stoichiometry of the material. To mention a few examples from recent past, pressure has been observed to drive the parent compound of 122 arsenide superconductors $BaFe_2As_2$ into a superconducting phase, which otherwise exhibits superconductivity only on chemical doping [1]. Application of pressure is also seen to induce metallization in the anti-ferromagnetic insulator $BaMn_2As_2$ [2]. Thus the high pressure studies on TI system is based on two reasonable expectations: (a) pressure can help in suppressing the 3D charge carrier density responsible for the bulk conductivity and can enhance the relative contribution of 2D charge carrier density corresponding to surface states in the electronic transport, (b) pressure can induce superconductivity by employing these surface states and hence provide a valuable tool to explore topological insulator/superconductor interface. A great deal of reports on high pressure studies on end compounds Bi_2Se_3 and Bi_2Te_3 are available in literature [3][4][5][6] but little exist on the pressure dependent evolution of the transport properties of Te doped Bi_2Se_3 single crystals. Thus, this chapter brings about a systematic pressure dependent evolution of ground state behaviour of entire $Bi_2Se_{3-x}Te_x$ ($x = 0, 1, 2, 3$) series. It is known that these compounds can retain the ambient crystal structure only upto a pressure $P < 8$ GPa [3][5]. Therefore present investigations are restricted to the pressure range until which the systems remain in ambient phase, and hence purportedly retain their topologically protected surface states.

6.1 Synthesis and X-ray diffraction

Single crystals of $Bi_2Se_{3-x}Te_x$ (x = 0, 1, 2, 3) system were synthesized by melting stoichiometric mixtures of Bi, Se and Te at 850°C in an evacuated quartz tube, followed by cooling to 550°C over 300 hours. They were then maintained at this temperature for 24 hours and were then rapidly cooled to room temperature. The temperature profile for the synthesis is similar to the one mentioned in Section 3.1.1 and hence the x = 0 sample in this series is the same as Bi_2Se_3 (BS1) in Chapter 3. Phase formation was checked by room temperature powder x-ray diffraction (XRD) on powdered single crystals carried out at BL-12 beam-line of Indus II, RRCAT – Indore. Figure 6.1 shows the powder diffraction data on the $Bi_2Se_{3-x}Te_x$ crystals. All the observed XRD peaks are indexed and no extra peaks corresponding to a secondary impurity phase are observed (ref. Figure 6.1). The analysis of XRD data indicated that the samples crystallized in the $R\bar{3}m$ structure. Figure 6.2(a) shows the variation of lattice parameters *a* and *c*, deduced by analysing the pattern using *PowderCell* [7] refinement routine. It is observed that parameters *a* and *c* increase monotonically with increasing Te concentration in $Bi_2Se_{3-x}Te_x$. Figure 6.2(b) shows the variation of unit cell volume with Te substitution. It is observed that the volume increases which substantiates the incorporation of the bigger Te ion at the Se position in the lattice. The values are consistent with the earlier reports on the system [8].

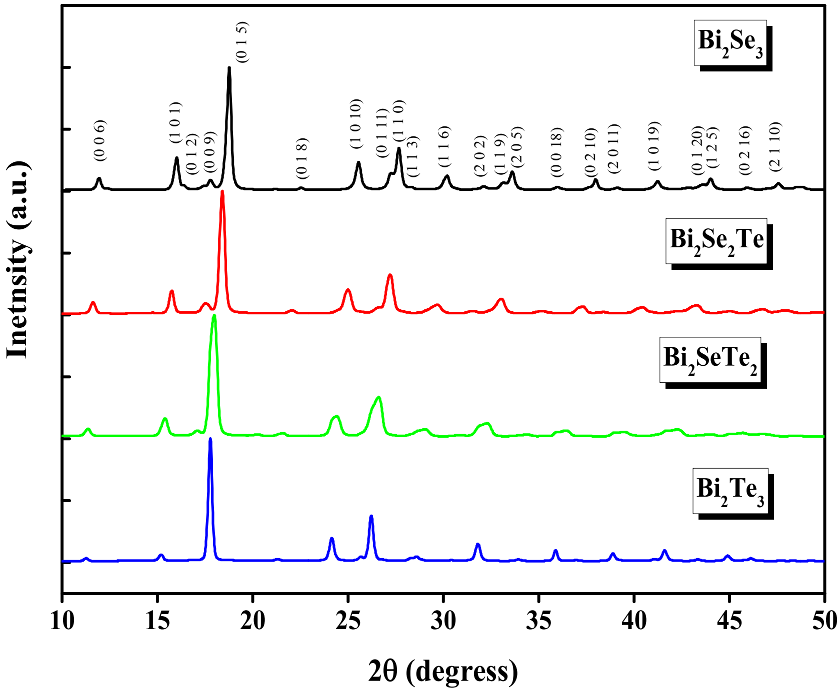

Figure 6.1 – Powder x-ray patterns of $Bi_2Se_{3-x}Te_x$ crystals normalised to the highest observed peak intensity. The graphs has been shifted vertically for clarity, the indices of the rhombohedral structure are shown.

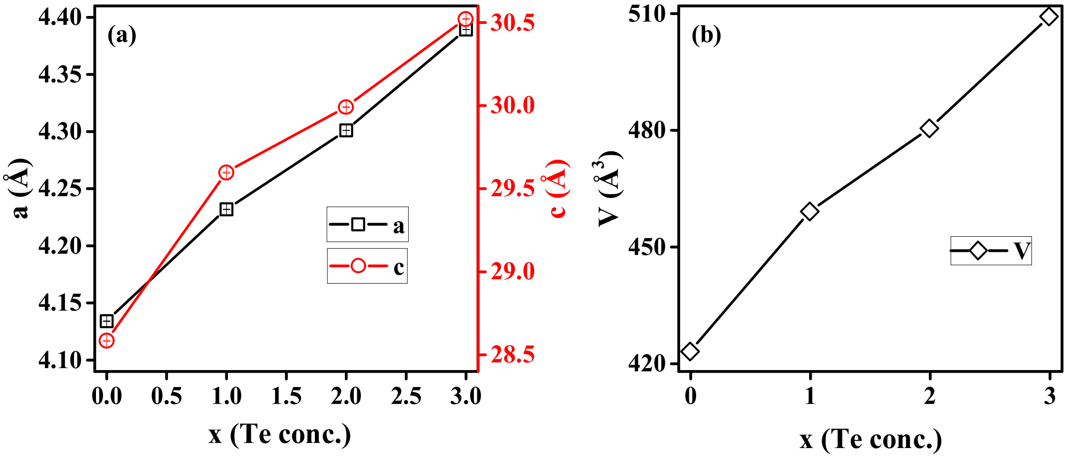

Figure 6.2 – **(a)** The variation of *a* and *c* lattice parameters for Te substituted Bi_2Se_3 samples; **(b)** variation of unit cell volume as a function of Te concentration

6.2 Ambient pressure resistivity

The evolution of temperature dependent electrical resistivity ρ(T) behaviour with Te substitution in $Bi_2Se_{3-x}Te_x$ system (x = 0, 1, 2, 3) is shown in Figure 6.3(a)-(d) respectively. It is evident from the figure that metallic behaviour observed in end compounds Bi_2Se_3 and Bi_2Te_3 is progressively suppressed under Te substitution and overall ρ(T) increases from x = 0 to x = 2. Metal to non-metal transition is observed at T = 100 K for x = 1 and T = 150 K for x = 2. This indicates that Te substitution may help in revealing, though partially, the intrinsic bulk insulating behaviour of Bi_2Se_3 which otherwise was masked by the carriers from Se vacancies. The variation of room temperature resistivity ρ_{300K}, as a function of Te concentration in $Bi_2Se_{3-x}Te_x$ system is shown in Figure 6.3(e)). It is observed that ρ_{300K} increases upto x = 2 then decreases.

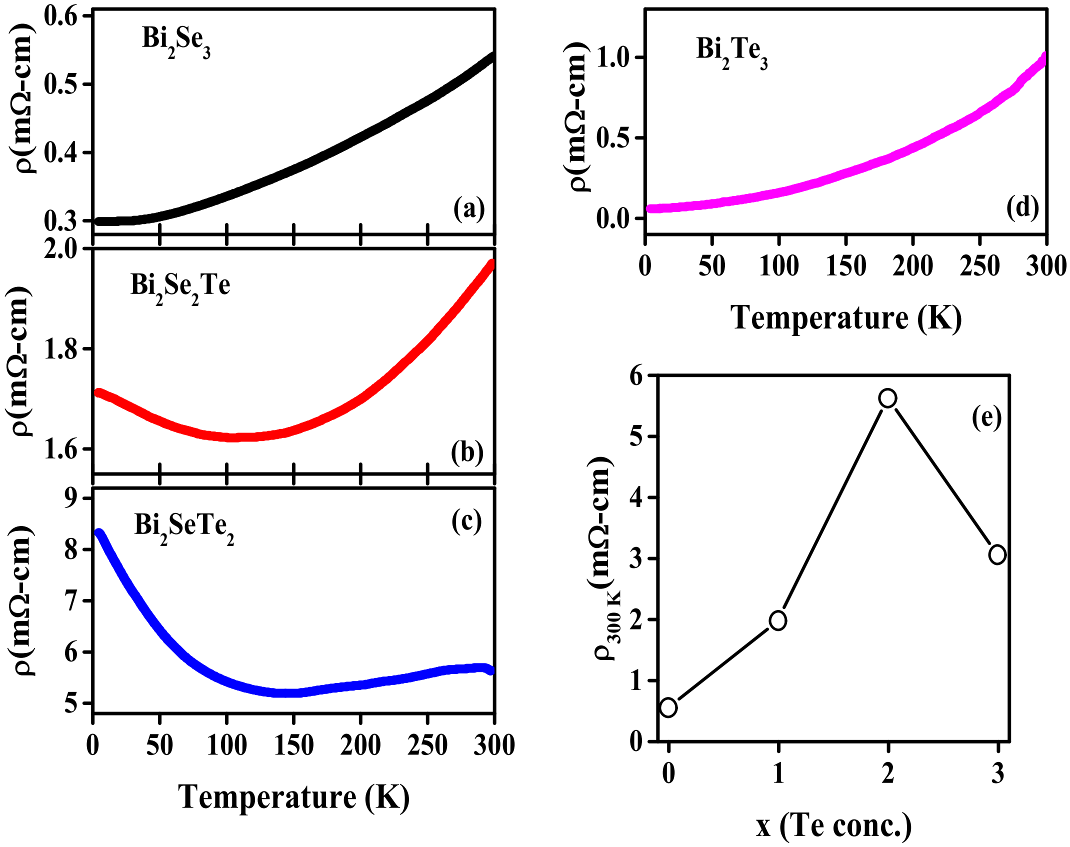

Figure 6.3 – Resistivity vs. Temperature behaviour of **(a)** Bi_2Se_3; **(b)** Bi_2Se_2Te; **(c)** Bi_2SeTe_2; **(d)** Bi_2Te_3; **(e)** Variation of ρ_{300K} as a function of Te content x in $Bi_2Se_{3-x}Te_x$.

To understand the behaviour of resistivity values with Te concentration, Hall Effect measurements were carried out to determine the nature of charge carriers and also the carrier concentration.

6.3 Hall Effect Measurements

Figure 6.4(a) shows the Hall data on the $Bi_2Se_{3-x}Te_x$ (x = 0, 1, 2, 3) samples. It is evident from the data that Bi_2Se_3, Bi_2Se_2Te and Bi_2SeTe_2 show n-type carriers and Bi_2Te_3 exhibits p-type carriers. Figure 6.4(b) & (c) show the variation of charge carrier concentration and mobility with Te concentration respectively. These quantities exhibit systematic non-monotonic variation with x, i.e., n & μ decreases upto x = 2 then increases for x = 3. The decrease in carrier density under Te substitution of iso-electronic Se is consistent with the view that Te help in suppressing Se vacancies and hence reducing the bulk conductivity. However, the increase in carrier concentration in Bi_2Te_3 can be associated with the increase in number of Te_{Bi} anti-site defects that are predominant in Bi_2Te_3.

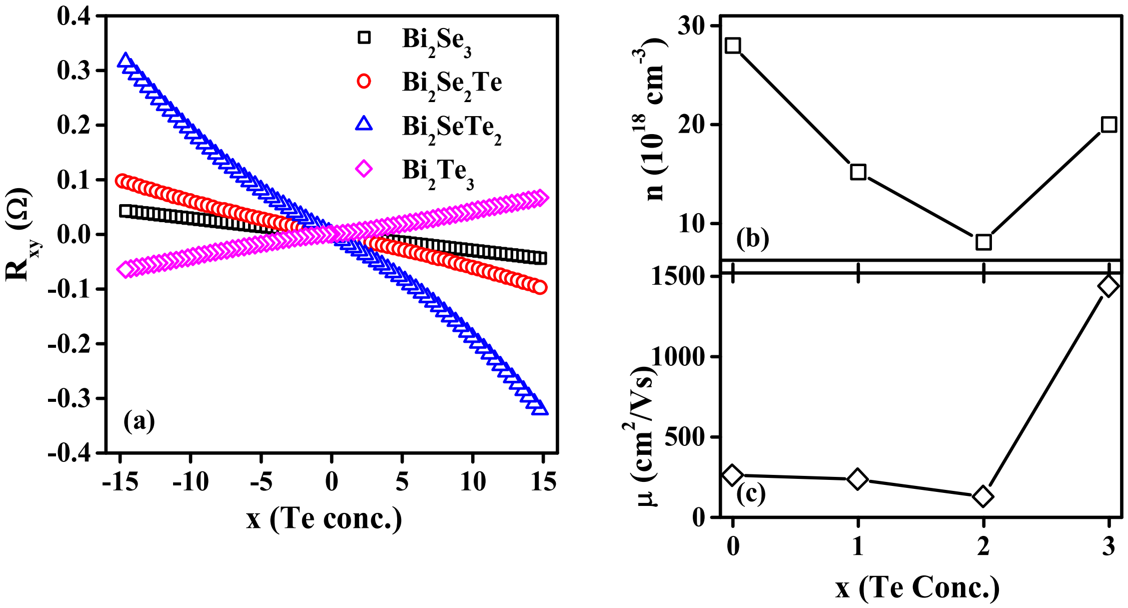

Figure 6.4 - (a) Hall data on synthesized samples as a function of Te concentration; Variation of **(b)** n and **(c)** μ as a function of Te content x in $Bi_2Se_{3-x}Te_x$.

6.4 High Pressure resistivity

The results of the high pressure transport measurements performed on the series of $Bi_2Se_{3-x}Te_x$ single crystals with x =0, 1, 2 and 3 are presented below.

6.4.1 Bi_2Se_3

Figure 6.5(a)-(h) shows the temperature dependent resistivity normalized with respect to room temperature resistivity (ρ(T)/ρ(300K)) at various indicated pressures from 0 to 7.5 GPa in 4 – 300 K temperature range.

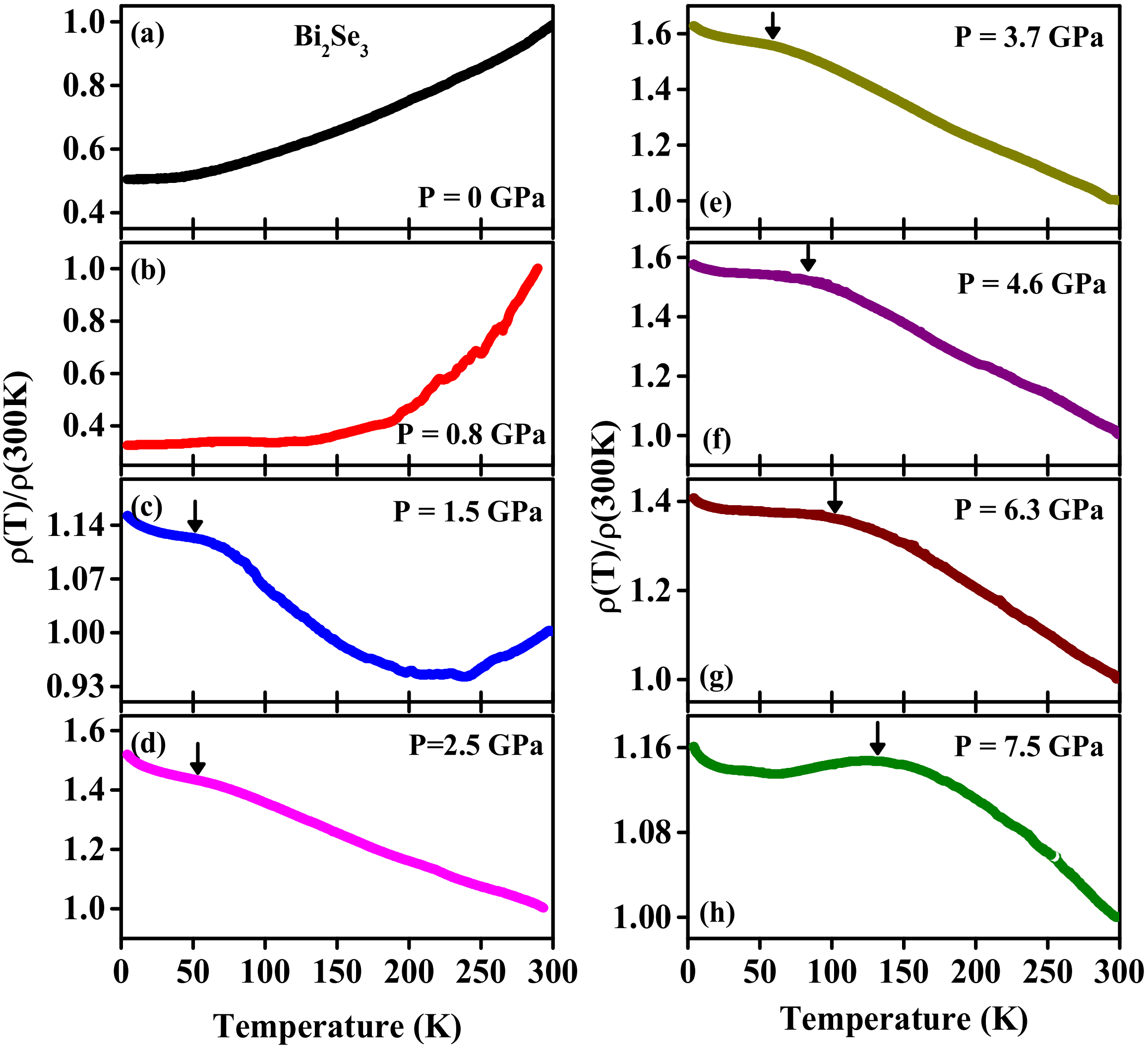

Figure 6.5 – (a)-(h) Normalized Resistivity ρ(T)/ρ(300K) versus T plots at for Bi_2Se_3 at various pressures (from 0 GPa to 7.5 GPa). Arrow marks the position around which $T_{shoulder}$ occurs in the resistance curve

It is seen that Bi_2Se_3 exhibits metallic behaviour at ambient pressure (Figure 6.5(a)), as can be inferred from the positive temperature coefficient of resistivity. The resistivity seems to saturate for temperature below T ~ 30 K. On increasing the pressure to 0.8 GPa

(Figure 6.5(b)), the sample continues to exhibit metallic behaviour but the saturation temperature of resistance raises to ~ 150 K. At a pressure of 1.5 GPa, the slope of resistivity is observed to change from a positive to negative value below T ~ 250 K indicating a metal to insulator transition (MIT). For pressure P ≥ 2.5 GPa, the transport shows a negative slope in the entire temperature range (Figure 6.5(d)) indicating non-metallic behaviour in entire temperature range. In addition to the negative slope, the resistance behaviour shows a shoulder like feature, denoted as $T_{shoulder}$ for P ≥ 1.5 GPa. The value of $T_{shoulder}$ is observed to increase with increasing pressure, from 50 K at 1.5 GPa to 125 K at 7.5 GPa (see Figure 6.5(c)-(h) as marked by arrows). The monotonic increase of $T_{shoulder}$ with pressure (P) is shown in the Figure 6.6.

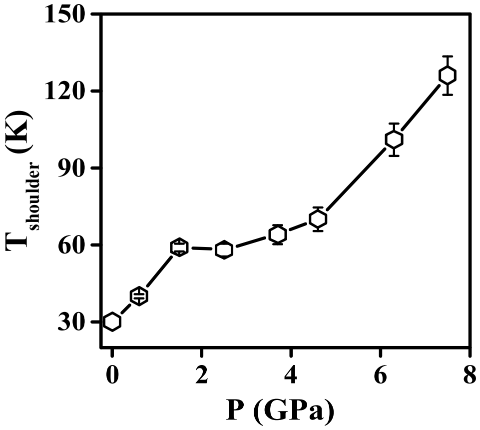

Figure 6.6 – Variation of temperature around which $T_{shoulder}$ appears as a function of pressure (P)

6.4.2 Bi_2Se_2Te

Figure 6.7(a)-(g) exhibits the variation of the normalized resistivity ρ(T)/ρ(300K) at various pressures for Bi_2Se_2Te system. It is observed that at ambient pressure conditions, the ρ(T)/ρ(300K) curve exhibits a positive temperature co-efficient till ~ 125 K, below which an upturn in resistivity is observed. With application of a small pressure of 0.9 GPa, the resistivity upturn shifts to a higher temperature of ~ 250 K, below which the system shows a semiconducting behaviour. At 1.2 GPa, the system completely exhibits semiconducting behaviour from room temperature to 4.2 K. At a pressure of 1.6 GPa, the system sheds its semiconducting behaviour to become completely metallic and the resistivity value saturates below 20 K.

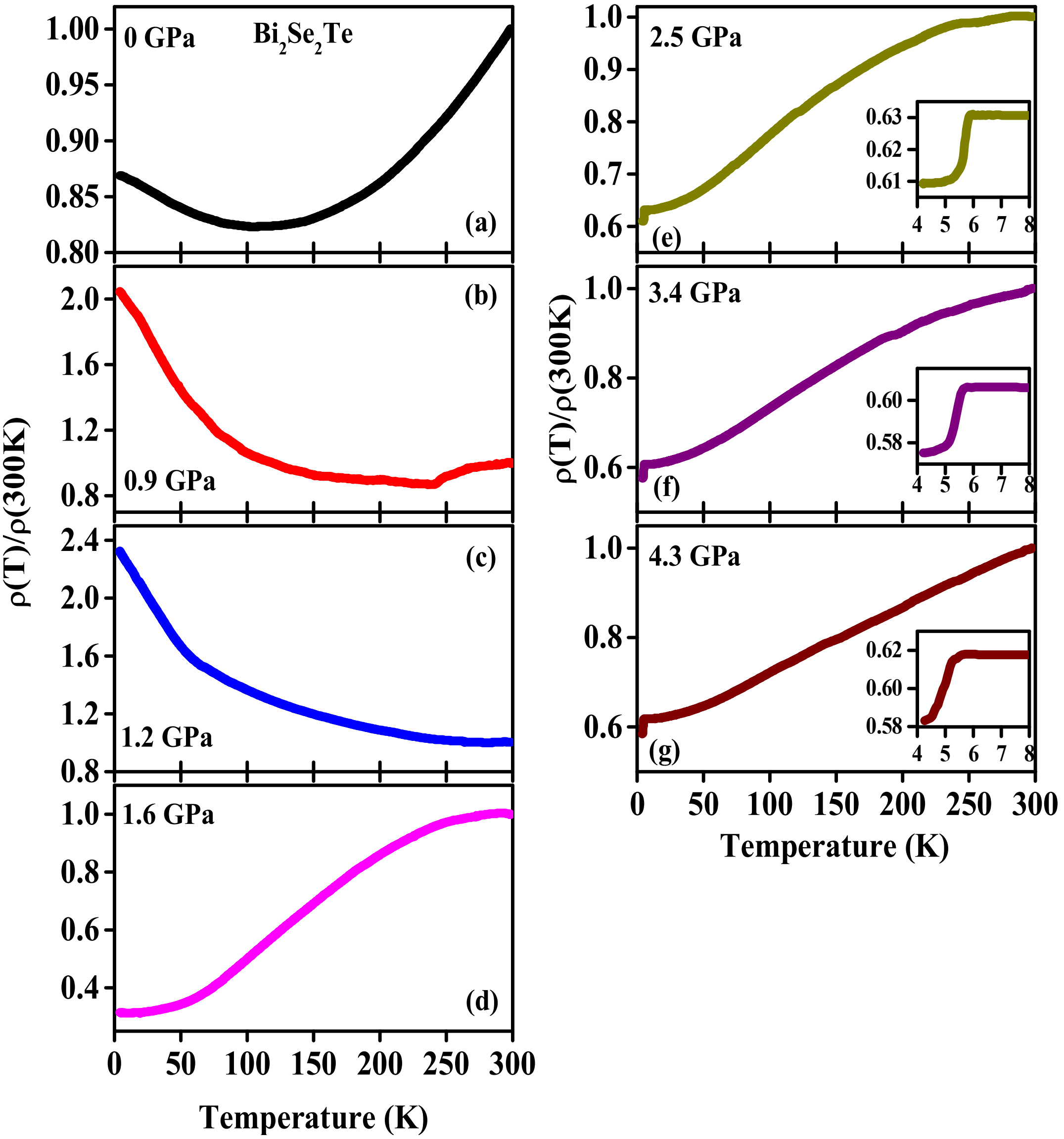

Figure 6.7 – (a)-(g) Variation of normalized resistivity ρ(T)/ρ(300K) as a function of temperature at various specified pressures from 0 to 4.5 GPa of Bi_2Se_2Te sample. Insets in (e)-(g) exhibit closer view of superconducting transition.

Interestingly, a pressure induced superconducting transition is observed at P ~ 2.5 GPa with a transition temperature (T_c) onset of 5.9 K. The transition temperatures of onset, midpoint, or zero resistance are defined based on the differential of resistance over temperature (dR/dT) (as shown in Figure 6.8(a)). Insets in Figure 6.7(e)-(g) show a magnified view of the superconducting transition of Bi_2Se_2Te at various pressures.

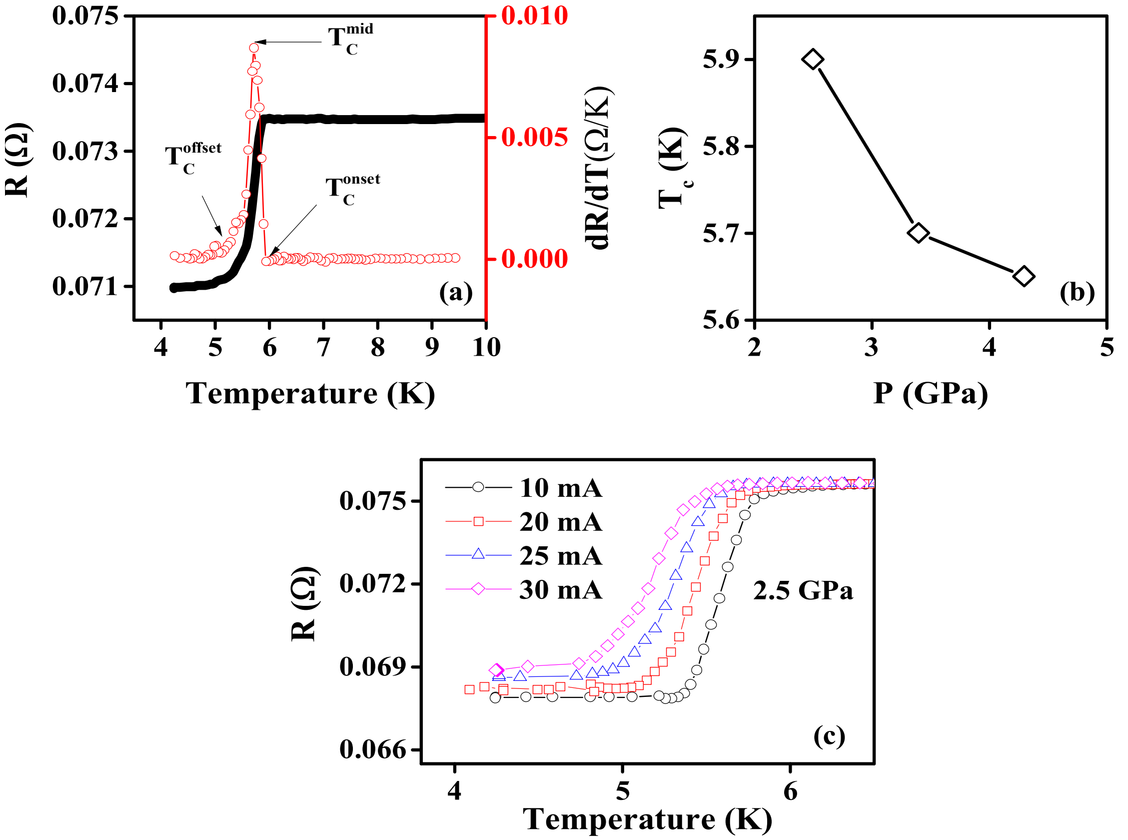

Figure 6.8 – (a) resistance near the critical temperature T_C with the differentiation of dRdT showing the definition of T_C^{onset} , T_C^{mid} and T_C^{offset} respectively; **(b)** variation of T_c onset as a function of pressure in Bi_2Se_2Te; **(c)** current dependence of the superconducting transition at 2.5 GPa

The variation of the T_c onset with pressure is shown in Figure 6.8(b). It is found that T_c decreases with increasing pressure. Figure 6.8(c) shows the current dependence of the transition measured at P = 2.5 GPa. It is found that transition shifts towards lower temperature with increasing the biased DC current as expected from a superconducting transition, a well known Silsbee effect. Thus even though zero resistance is not observed, the current dependence seems to provide evidence that the observed transition is to a superconducting state.

6.4.3 Bi_2SeTe_2

The evolution of temperature dependent normalized resistivity ρ(T)/ρ(300K) behaviour of Bi_2SeTe_2 system at various pressures is shown in Figure 6.9(a)-(e).

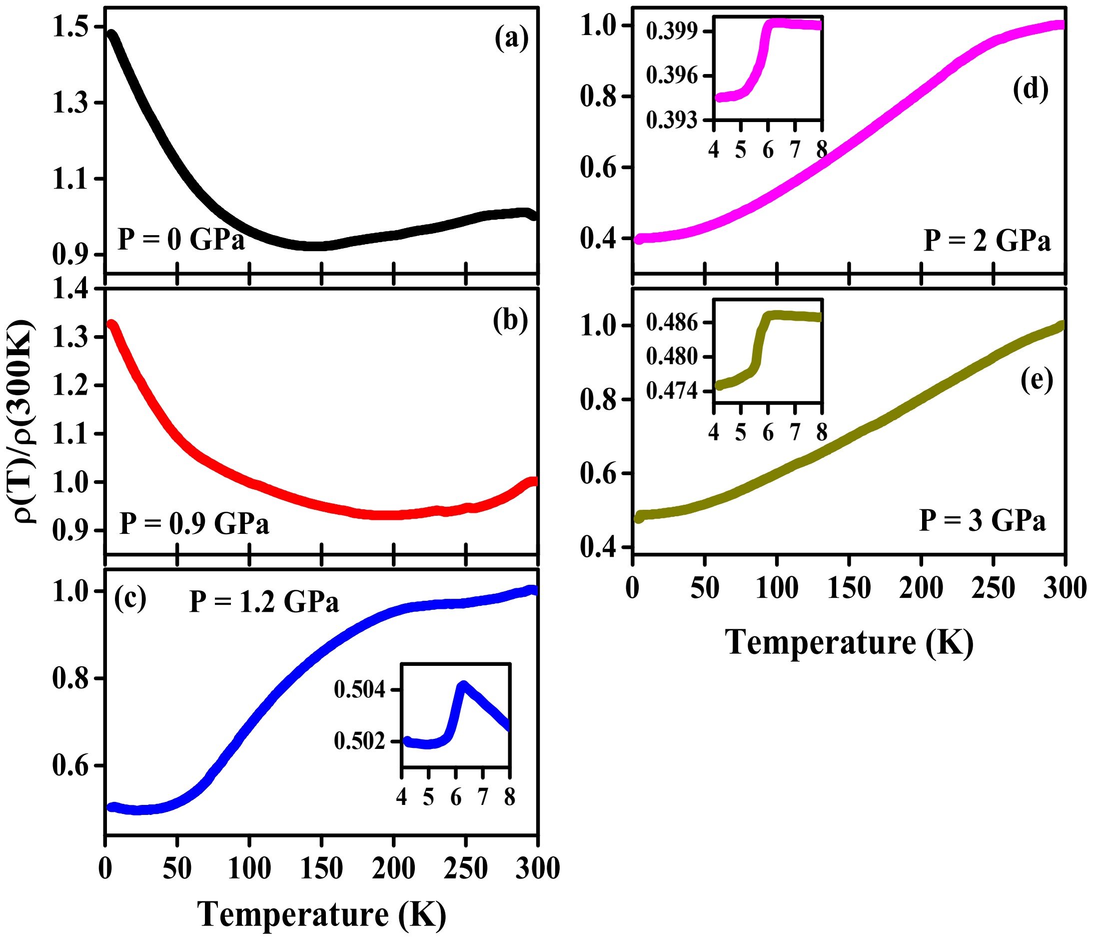

Figure 6.9 – **(a)-(e)** Variation of normalized resistivity for Bi_2SeTe_2 sample as a function of temperature at various specified pressures from 0 to 3 GPa. Insets in (c)-(e) exhibit closer view of superconducting transition.

At ambient pressure, the resistance initially decreases over a small range till 150 K, below which the system shows a negative temperature coefficient akin to a semiconducting behavior. At 0.9 GPa, the system shows a similar characteristics as that of the ambient except that the semiconducting nature begins below T ~ 200 K. With further increase in pressure to 1.2 GPa, the metallic behavior extends down to 20 K and an onset of a pressure induced superconducting transition at 6.20 K is observed. The pressure dependence of T_c is shown in Figure 6.10(a). It is seen that the T_c onset shifts to lower values with increasing the applied pressure. This is similar to the trend observed for Bi_2Se_2Te system (see Figure 6.8(b)). The current dependence of the transition temperature is shown in Figure 6.10(b). Here again T_c shifts to lower temperatures with increasing the current value, though the shift is smaller compared to that in the case of Bi_2Se_2Te.

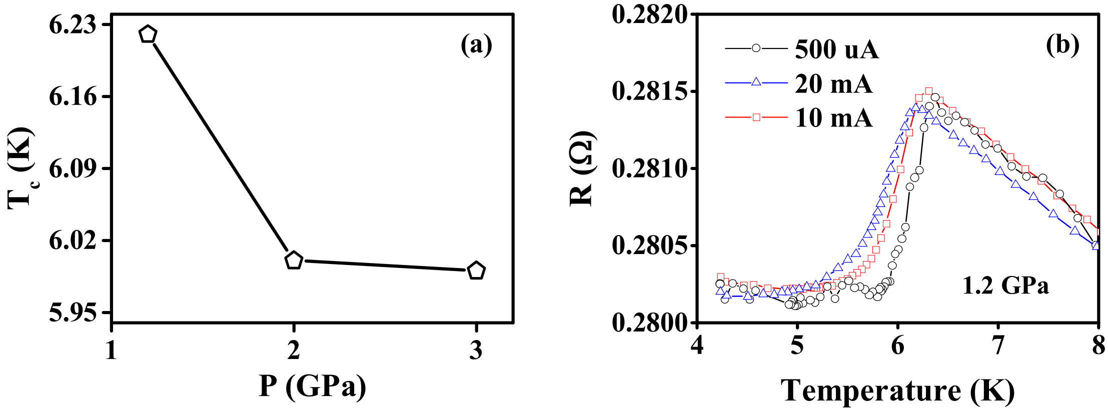

Figure 6.10 – **(a)** Variation of transition temperature onset as a function of pressure in Bi_2SeTe_2; **(b)** current dependence of the transition temperature at 1.2 GPa.

6.4.4 Bi_2Te_3

Figure 6.11(a)-(e) displays the evolution of normalized resistivity as a function of the temperature of the Bi_2Te_3 at various pressures. At ambient pressure Bi_2Te_3 exhibits a metallic behavior like Bi_2Se_3. However, unlike Bi_2Se_3 which shows to non-metallic behavior at higher pressure (P > 1.5 GPa), the conductivity behavior in Bi_2Te_3 remains metallic at all the pressures reported here. We observe a pressure induced superconducting transition in Bi_2Te_3 at a critical pressure of 1.7 GPa. The onset of superconducting transition temperature at this pressure is observed to be at 5.87 K. The closer view of superconducting transition is shown in the insets of Figure 6.11(c)-(e) at various pressures. The variation of T_c with pressure is shown in Figure 6.12(a) and the current dependence of the transition temperature at 1.7 GPa is shown in Figure 6.12(b). It can be seen that the value of T_c changes little with increase in the applied pressure.

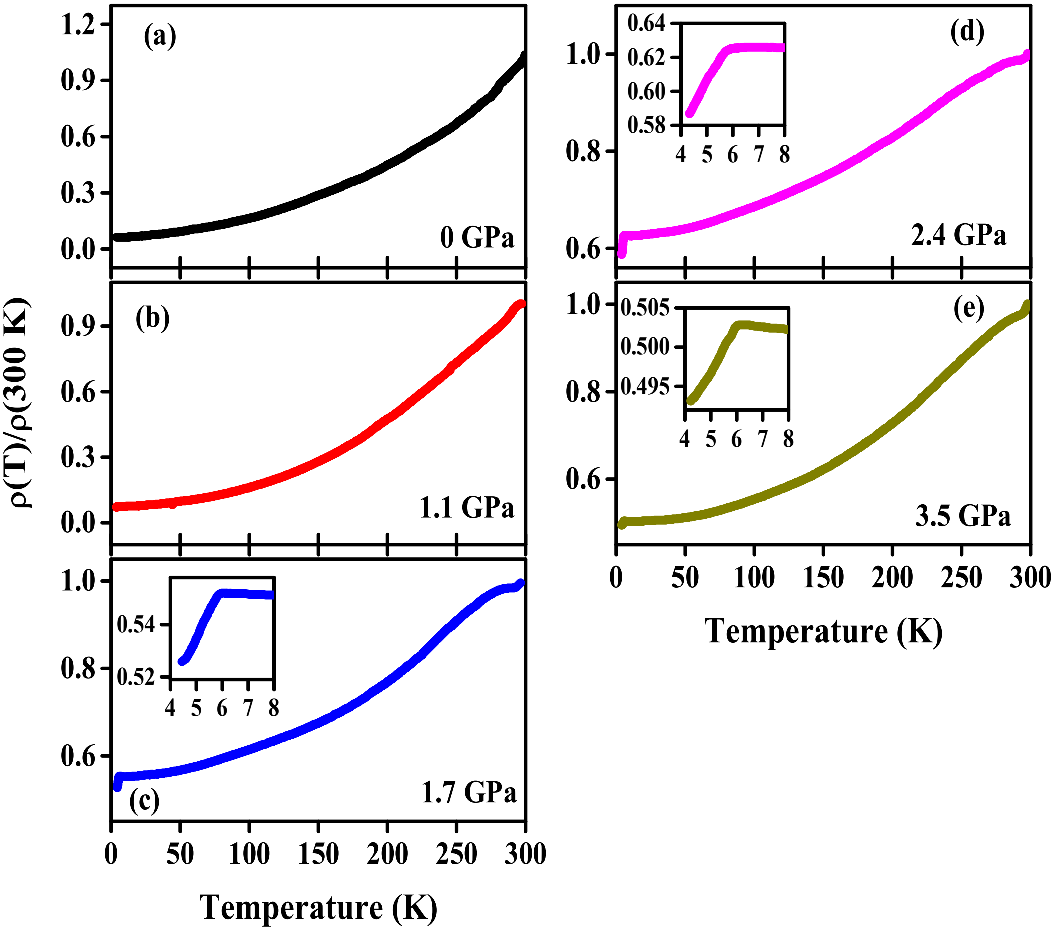

Figure 6.11 – (a)-(e) Variation of normalized resistivity for Bi_2Te_3 sample as a function of temperature at various specified pressures from 0 to 3.4 GPa. Insets in (c)-(e) exhibit closer view of superconducting transition

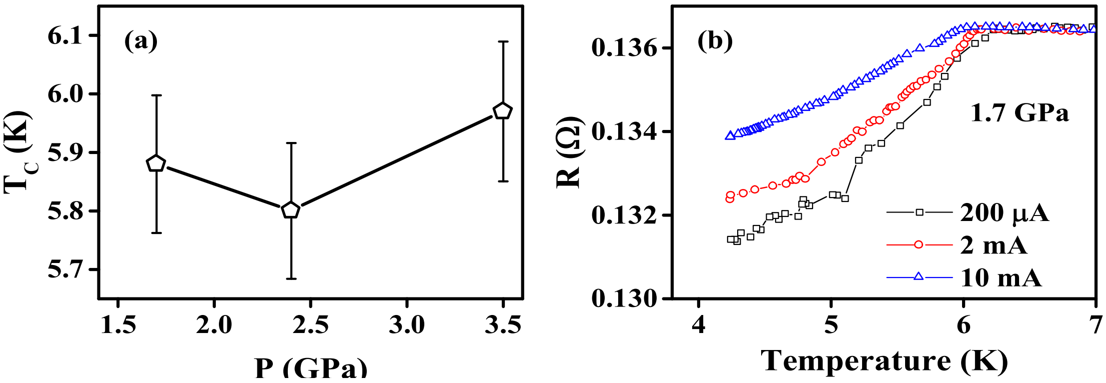

Figure 6.12 – (a) Variation of transition temperature onset as a function of pressure in Bi_2Te_3; **(b)** current dependence of the transition temperature at 1.7 GPa

6.5 Discussion

In present study, no superconducting transition is observed in Bi_2Se_3 upto the measured pressure of 7.5 GPa. From the high pressure resistivity data we observed that the net effect of pressure on Bi_2Se_3 is to drive this system from initial metallic behaviour to an increasingly semiconductor like behavior (Figure 6.5(a)-(h)). Similar results were obtained by Hamlin et al. wherein pressure is initially seen to drive Bi_2Se_3 toward less metallic behaviour until 8 GPa, after which a structural transition is observed [1]. The suppression of metallic behaviour under pressure, leading to a metal – insulator transition, may indicate a pressure induced suppression of bulk conductivity possibly due to squeezing out of Se vacancies. These vacancies in the as prepared sample give rise to defect states that pin Fermi energy to bulk conduction band, and hence result in the metallic resistivity. The resistivity below $T_{shoulder}$ showing weak temperature dependence seems to capture the contribution from the topological surface states. It is seen that ρ(T) below $T_{shoulder}$ gradually flattens as $T_{shoulder}$ progressive shifted to higher temperature with increasing pressure. This can stem from the fact that surface states provide parallel metallic conduction in conjunction to the bulk states. Due to suppression of bulk conductivity under pressure, the relative contribution from surface states would become more prominent and hence dictate ρ(T) behavior at low temperatures.

However in Te substituted samples, no such $T_{shoulder}$ behaviour is observed. An interesting outcome of high pressure studies on $Bi_2Se_{3-x}Te_x$ has been the occurrence of pressure induced superconductivity for x = 1, 2 and 3. The T_c of all the three samples is found to be within 6±0.2 K. In earlier studies on p-type Bi_2Te_3, the pressure induced superconductivity was seen to occur at P = 3.2 GPa with value of T_c of 2.6 K [5][6]. It should be mentioned that ambient parent structure of Bi_2Te_3 persists upto ~ 6 GPa and the observed T_c remained unchanged upto the pressures of 6 GPa. Though the pressure independent behavior of T_c observed in our sample is similar to that seen by Zhang et al [5], the value of T_c (5.9 K) is significantly higher and the onset of superconducting phase too occurs at a comparatively lower critical pressure (1.2 GPa).

It is observed that T_c decreases with increasing pressure for Bi_2Se_2Te and Bi_2SeTe_2, while T_c remains invariant with pressure for Bi_2Te_3. The rate of decrease of T_c per unit pressure $\left({dT_c}/{dP}\right)$ is calculated to be = 0.139 K/GPa for Bi_2Se_2Te and = 0.127 K/GPa for Bi_2SeTe_2. The values of $\frac{d\ln T_c}{dP} = \left[\frac{1}{T_c}\left(\frac{dT_c}{dP}\right)\right]$ are calculated to be = 0.023 and 0.02 GPa^{-1} for Bi_2Se_2Te and Bi_2SeTe_2 respectively. The value of $\frac{d\ln T_c}{dP}$ is reported to be within the range of 0.01 – 0.08 for the conventional superconductors [9]. This suggests that the nature of pressure induced superconductivity seen in $Bi_2Se_{3-x}Te_x$ systems may be of conventional BCS type. In order to gain further insight about the role of electron-phonon interaction in inducing superconductivity in this system, we try to fit the normal state resistivity of $Bi_2Se_{3-x}Te_{x,}$ at critical pressures (P_c) at which superconduтivity is observed, using the Bloch-Gruneisen equation, applicable to a conventional metal to deduce the Debye temperature, which is related to the frequency of the acoustic phonons responsible for electron's scattering [10].

$$\rho(T) = A + BT^2 + C\left(\frac{T}{\Theta}\right)^3 \int_0^{\frac{\Theta}{T}} \left[\frac{x^3 dx}{(e^x - 1)(1 - e^{-x})}\right] \tag{6.1}$$

Here, A is a constant that represents residual resistivity due to electron – impurity scattering, BT^2 accounts for electron – electron interaction and $C\left(\frac{T}{\Theta}\right)^3 \int_0^{\frac{\Theta}{T}} \left[\frac{x^3 dx}{(e^x - 1)(1 - e^{-x})}\right] =$ represents the electron – phonon scattering contribution to resistivity. Figure 6.13 shows the high pressure resistivity data fitted to the above equation.

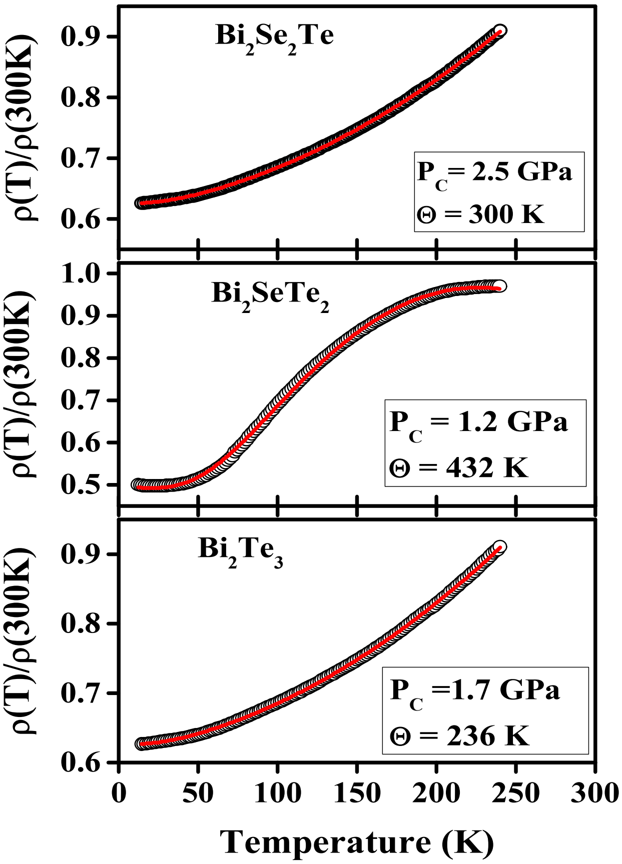

Figure 6.13 – Normal state resistivity data at critical pressure P_c for Bi_2Se_2Te, Bi_2SeTe_2 and Bi_2Te_3 fit to eqn. (6.1)

The value of B found from the fitting is of the order of 10^{-5}, which indicates that electron correlation is not very significant in this system. The value of Debye temperature Θ extracted from the fit is found to be 236 K for Bi_2Te_3 at P_c =1.7 GPa, 300K for Bi_2Se_2Te at P_c = 2.5 GPa and 432K for Bi_2SeTe_2 at P_c =1.2 GPa. The value of electron phonon coupling constants λ is obtained by substituting the values of Θ and T_c in McMillan's formula [11] given below:

$$T_C = \frac{\Theta}{1.45} exp\left[\frac{-1.04(1+\lambda)}{\lambda - \mu^*(1+0.62\lambda)}\right] \tag{6.2}$$

Where, the values of μ^*, which is the Effective Coulomb repulsion term is taken as 0.1.

The value of λ, deduced using Eq. 6.2 at is found to be 0.66 for Bi_2Te_3; 0.61 for Bi_2Se_2Te and 0.55 for Bi_2SeTe_2. These values of $\lambda < 1$ may indicate that observed pressure induced superconductivity in $Bi_2Se_{3-x}Te_x$ may lie in the regime of weakly coupled superconductors.

6.6 Conclusion

The high pressure resistivity of $Bi_2Se_{3-x}Te_x$ (x = 0, 1, 2, 3) single crystals have been studied. Bi_2Se_3 which exhibits metallic behaviour under ambient conditions becomes non-metallic at pressure > 1.5 GPa and the non-metallicity persists till 7.5 GPa. Pressure induced superconductivity has been observed in the Te doped systems Bi_2Se_2Te, Bi_2SeTe_2 and Bi_2Te_3 with transition temperatures of 5.9 K, 6.2 K and 5.87 K respectively. The value of $\frac{d\,ln\,T_C}{dP}$ estimated for the BST and BTS of ~ 0.023 and 0.020 respectively suggests that the nature of superconductivity seen in $Bi_2Se_{3-x}Te_x$ systems may be of conventional BCS type. The Debye temperature is estimated from the Bloch-Gruneisen fit to the normal state resistivity at critical Pressure (P_c). The value of electron-phonon coupling constant determined from the McMillan's formula suggests that the observed pressure induced superconductivity in $Bi_2Se_{3-x}Te_x$ may lie in the regime of weakly coupled superconductors.

References

[1] Awadhesh Mani, Nilotpal Ghosh, S. Paulraj, A. Bharathi and C. S. Sundar, *EPL* **87** (2009) 17004

[2] A. T. Satya, Awadhesh Mani, A. Arulraj, N. V. Chandra Shekar, K. Vinod, C. S. Sundar, and A. Bharathi, *Phys. Rev. B* **84** (2011) 180515(R)

[3] J. J. Hamlin, J. R. Jeffries, N. P. Butch, P. Syers, D. A. Zocco, S. T. Weir, Y. K. Vohra, J. Paglione and M. B. Maple, *J. Phys.: Condens. Matter* **24** (2012) 035602

[4] Kevin Kirshenbaum, P. S. Syers, A. P. Hope, N. P. Butch, J. R. Jeffries, S. T. Weir, J. J. Hamlin, M. B. Maple, Y. K. Vohra, and J. Paglione, *Phys. Rev. Lett.* **111** (2013) 087001

[5] J. L. Zhang, S. J. Zhang, H. M. Weng, W. Zhang, L. X. Yang, Q. Q. Liu, S. M. Feng, X. C. Wang, R. C. Yu, L. Z. Cao, L. Wang, W. G. Yang, H. Z. Liu, W. Y. Zhao, S. C. Zhang, X. Dai, Z. Fang, and C. Q. Jin, *Proc. Natl. Acad. Sci. U.S.A.* **108** (2011) 24

[6] Chao Zhang, Liling Sun, Zhaoyu Chen, Xingjiang Zhou, Qi Wu, Wei Yi, Jing Guo, Xiaoli Dong, and Zhongxian Zhao, *Phys. Rev. B* **83** (2011) 140504(R)

[7] W. Kraus & G. Nolze *J. Appl. Cryst.* **29** (1996) 301

[8] S. Nakajima, *Journal of Physics and Chemistry of Solids* **24** (1963) 479

[9] H. D. Yang, S. Mollah, W. L. Huang, P. L. Ho, H. L. Huang, C.-J. Liu, J.-Y. Lin, Y.-L. Zhang, R.-C. Yu, and C.-Q. Jin, *Phys. Rev. B* **68** (2003) 092507

[10] Awadhesh Mani, N. Gayathri, A. Bharathi, *Solid State Communications* **149** (2009) 899

[11] W. L. McMillan, *Phys. Rev.* **167** (1968) 331

CHAPTER 7

Summary of thesis and Future Work

The work presented in this thesis focussed on the low temperature transport properties of the Topological Insulator system Bi_2Se_3. Single crystals were synthesized using the modified Bridgman method. Magneto-transport measurements were carried out in the temperature range of 4.2 K – 300 K and magnetic field range of 0 – 15 T. High pressure transport measurements were performed in pressure range of 0 – 8 GPa. The summary of various results in this thesis are presented below.

1. In Chapter 3, the role of defects in observing the quantum oscillations in magneto-transport experiments on the topological insulator Bi_2Se_3 has been investigated. Using positron lifetime spectroscopy as a tool for defect characterisation, it has been established that the vacancy defect (V_{Se}) plays the major role in the n-type doping of the bulk in Bi_2Se_3. From Laue experiments it is observed that growing single crystals of Bi_2Se_3 with excess Se in the starting stoichiometry ($Bi_2Se_{3.1}$, $Bi_2Se_{3.2}$) or changing the rate of cooling from the melt during single crystal growth (BS2) is seen to introduce extended defects such as stacking faults and low angle grain boundaries in the lattice. These defects are seen to induce an upward band bending in the system and Shubnikov de Haas (SdH) oscillations with contributions from Topological Surface States (TSS) are observed in magneto-resistance measurements.
2. In Chapter 4, the effect of Sb substitution at Bi site on transport properties of single crystals of Bi_2Se_3 ($Bi_{2-x}Sb_xSe_3$; x = 0, 0.05, 0.1, 0.3, 0.5) has been studied. The resistivity of the samples is seen to increase with increasing Sb substitution with an anomalous reduction in x = 0.5 sample which can be attributed to the presence of multiple phases x = 0.5 sample. The Sb substitution is seen to reduce the concentration of Vacancy defects (V_{Se}) as observed from Hall Effect and positron lifetime measurements. From the magneto-transport studies it

is seen that increasing Sb substitution beyond x = 0.3 leads to SdH oscillations with mixed signatures from both TSS and a conventional 2DEG system.

3. The effect of Te substitution at Se site on transport properties of single crystals of Bi_2Se_3 ($Bi_2Se_{3-x}Te_x$; x = 0, 1, 1.8, 2) has been studied in Chapter 5. With Te substitution metal-insulator transition is seen in resistivity, with the MIT transition temperature increasing with increasing Te content. In Hall Effect measurements, the hall response changes from linear to non-linear with increase in Te concentration, indicating the presence of multiple (two) carriers in the system, which can be identified with carriers from the bulk and carriers from the topological surface states. The mobility of the samples is seen to reduce drastically suggesting increasing electronic disorder with Te substitution. The above statement is vindicated by the values of the Ioffe-Regel parameter ($k_F l$), calculated from resistivity and hall data which lie very close to one for the higher Te concentrations (x = 1.8, 2). Weak-Anti localization behaviour, a signature of time reversal invariant topological surface states are observed in the highly disordered samples, suggesting that the transport from TSS can be realised in transport by introducing strong electronic disorder into the system and achieving the quantum diffusive condition of $l_\varphi > l$.

4. In Chapter 6 the high pressure low temperature resistivity of $Bi_2Se_{3-x}Te_x$ (x = 0, 1, 2, 3) single crystals has been studied. It is observed that while Bi_2Se_3 shows increasingly non-metallic behaviour, the Te substituted samples are driven into a superconducting phase with pressure. The critical pressure P_c at which superconducting transition occurs is 2.5 GPa, 1.2 GPa and 1.7 GPa for x = 1, 2 and 3 respectively. The superconducting transition temperatures (T_c) onset of the three Te substituted systems i.e. x = 1, 2 and 3 are 5.9 K, 6.2 K and 5.87 K respectively. While the T_c of the x = 1, 2 systems decrease monotonically with pressure, it remains the same for x = 3 sample i.e. Bi_2Te_3. The nature of the pressure induced superconducting phase is found to be of conventional BCS type and the analysis of the

normal state resistivity at P_c suggests that the pressure induced superconductivity in $Bi_2Se_{3-x}Te_x$ system may lie in the regime of weakly coupled superconductors.

Future outlook

1. Effect of ion beam irradiation on the Topological surface states:

It is established in the present thesis that defects and disorder play a crucial role in observing the SdH oscillations or WAL from the TSS in magneto-transport measurements in Bi_2Se_3 based systems. With most of the crystals being naturally n-type (~ 10^{19} cm^{-3}), reducing the bulk conductivity is of prime technological importance to access the surface states. As discussed in Section 1.8, various dopings/substitutions have been tried to reduce the n-type doping and achieve a p-type Bi_2Se_3, However with exception to Hor et al. who achieved it in Ca doped system, the minimum value attained has been of the order ~ 10^{-16} cm^{-3}. Ion implantation provides an alternative route as the number and spatial distribution of dopants and thus the charge carrier concentration can be controlled. This can help in reducing the bulk conductivity in transport. Recently Sharma et al. [1] reported the feasibility of ion implantation in Bi_2Se_3. Thus it would be an interesting project to undertake a systematic study of ion irradiation with Bi or Se ions on Bi_2Se_3 and its effect on the magneto-transport properties of TI such as SdH oscillations or WAL.

2. Proximity effect in Topological Insulator/Superconductor (TI/SC) interface:

Achieving an intrinsic superconducting phase in a Topological insulator has been one of the main targets in this area of research. Much of the interest for this has been the interest to observe the elusive Majorana fermions. So far bulk superconductivity has been reported only on very few systems such as Cu intercalated Bi_2Se_3 [2] or under high pressure in Bi_2Te_3 [3], Bi_2Se_2Te, Bi_2SeTe_2 (current study); the reason being the weak electron-phonon coupling present in TIs. In this direction, an alternative approach is to make Topological

Insulator/Superconductor (TI/SC) interfaces and search for whether superconductivity can be induced via proximity effect in them. Such studies have been carried out using Bi_2Se_3/SC heterostructures where tin (Sn) [4] and $Bi_2Sr_2CaCu_2O_{8+\delta}$ (BSSCO) [5][6] have been used as the superconducting material with contrasting results. In this regard the 11 family of Iron arsenide superconductors such as FeSe [7] and $Fe_{1+y}Te_xSe_{1-x}$ [8] are also good candidate materials as superconductivity has been achieved both in their single crystalline [7][8] and thin film [9] form. Thus TI/SC heterostructures of the form $Bi_2Se_{3-x}Te_x$/ $Fe_{1+y}Te_xSe_{1-x}$ are a good system to study the proximity effect.

References

[1] P. A. Sharma, A. L. Lima Sharma, M. Hekmaty, K. Hattar, V. Stavila, R. Goeke, K. Erickson, D. L. Medlin, M.Brahlek, N. Koirala, and S. Oh, *Applied Physics Letters* **105** (2014) 242106

[2] Y. S. Hor, A. J. Williams, J. G. Checkelsky, P. Roushan, J. Seo, Q. Xu, H. W. Zandbergen, A. Yazdani, N. P. Ong and R. J. Cava, *Phys. Rev. Lett.* **104** (2010) 057001

[3] J. L. Zhang, S. J. Zhang, H. M. Weng, W. Zhang, L. X. Yang, Q. Q. Liu, S. M. Feng, X. C. Wang, R. C. Yu, L. Z. Cao, L. Wang, W. G. Yang, H. Z. Liu, W. Y. Zhao, S. C. Zhang, X. Dai, Z. Fang, and C. Q. Jin, *Proc. Natl. Acad. Sci. U.S.A.* **108** (2011) 24

[4] Fan Yang, Yue Ding, Fanming Qu, Jie Shen, Jun Chen, Zhongchao Wei, Zhongqing Ji, Guangtong Liu, Jie Fan, Changli Yang, Tao Xiang, and Li Lu, *Phys. Rev. B* **85** (2012) 104508

[5] T. Yilmaz, I. Pletikosić, A. P. Weber, J. T. Sadowski, G. D. Gu, A. N. Caruso, B. Sinkovic, and T. Valla, *Phys. Rev. Lett.* **113** (2014) 067003

[6] Su-Yang Xu, Chang Liu, Anthony Richardella, I. Belopolski, N. Alidoust, M. Neupane, G. Bian, *Phys. Rev. B* **90** (2014) 085128

[7] S. B. Zhang, Y. P. Sun, X. D. Zhu, X. B. Zhu, B. S. Wang, G. Li, H. C. Lei, X. Luo, Z. R. Yang, W. H. Song and J. M. Dai, *Supercond. Sci. Technol.* **22** (2009) 015020

[8] B. C. Sales, A. S. Sefat, M. A. McGuire, R. Y. Jin, D. Mandrus, and Y. Mozharivskyj, *Phys. Rev. B* **79** (2009) 094521

[9] Ta-Kun Chen, Jiu-Yong Luo, Chung-Ting Ke, Hsian-Hong Chang, Tzu-Wen Huang, Kuo-Wei Yeh, Chung-Chieh Chang, Po-Chun Hsu, Chun-Te Wu, Ming-Jye Wang, Mau-Kuen Wu, *Thin Solid Films* **519** (2010) 1540